

LASER COOLING AND MAGNETO-OPTICAL TRAPPING OF HOLMIUM ATOMS

By

Jinlu Miao

A dissertation submitted in partial fulfillment of
the requirements for the degree of

Ph.D
(Physics)

at the
UNIVERSITY OF WISCONSIN-MADISON
2013

Date of final oral examination: 08/21/2013

The dissertation is approved by the following members of the Final Oral Committee:

Mark Saffman, Professor, Physics

Jim Lawler, Professor, Physics

Deniz Yavuz, Associate Professor, Physics

Michael Winokur, Professor, Physics

John Wright, Professor, Chemistry

© Copyright by Jinlu Miao 2013

All Rights Reserved

To Zhen.

ACKNOWLEDGMENTS

First of all, I would especially like to thank my advisor, Mark, for giving me the opportunity to work on the holmium project and for his enduring patience and inspiring guidance throughout my PhD. Without his helpful discussions with me, I wouldn't have achieved anything. Larry Isenhower has been giving me a lot of guidance and help. Almost my whole lab skill set comes from him.

I would like to thank James Hostetter for pleasant cooperation on the holmium project in my last year and a half. I look forward to seeing new progresses for the rest of his PhD. And I would also like to thank Jake Covey, who helped on setting up our early version of the experiment when I was new to the group, and Georgios Stratis for helping us building blue diode lasers and the Zeeman slower that is going to be installed.

I also thank Marty Lichtman, Kara Maller, Gang Li, Jonathan Pritchard, and all the other group members for helpful discussions and patient cooperation in sharing lab equipments with me. And Siyuan Zhang has been a supportive and quiet lab-mate, roommate and friend. It has been a great pleasure to get to know all current and former group members over the past four years. The group lunches and the Friday beers by the terrace have been very enjoyable and memorable experience.

I have enjoyed all the hours spent in the lab, both the productive ones and the stuck ones. They have made me a better person in many aspects.

My parents and my aunt deserve special thanks for their unconditional love throughout my entire life, and their support and encouragement on my research work. I would especially like to thank Zhen, for coming to see me in Madison almost every month during the past five years. I am very grateful for his love and support. Our happy and stable relationship since college years is one of the best things in my life.

DISCARD THIS PAGE

TABLE OF CONTENTS

	Page
LIST OF TABLES	vi
LIST OF FIGURES	vii
1 Introduction	1
1.1 Quantum computing	1
1.2 Quantum register	1
1.3 Motivation	2
1.3.1 Collective encoding with Rydberg blockade	2
1.3.2 Why holmium	4
1.4 Laser cooling of rare earth atoms	4
1.4.1 Holmium	6
1.5 Summary	10
2 Vacuum System	11
2.1 Overview	11
2.2 Holmium source: initial Attempts	12
2.3 Holmium source: high temperature effusion cell	15
2.4 Atomic beam collimation and slowing	18
2.5 MOT chamber	18
2.6 Magnetic coils	19
2.7 Summary	21
3 Laser system	22
3.1 Overview	22
3.2 Home-made laser system	22
3.3 Periodically poled Potassium Titanyl Phosphate (PPKTP) crystal SHG	24
3.3.1 Single-pass Conversion efficiency	25
3.3.2 Total round trip Conversion Efficiency	26
3.4 Lithium Tri-Borate LiB_3O_5 (LBO) crystal SHG	32

	Page
3.4.1 Cavity setup	34
3.4.2 Mode-matching/impedance-matching measurement	37
3.4.3 Setup with M2 lasers	39
3.5 Summary	41
4 Spectroscopy	42
4.1 Hyperfine structure	42
4.2 Ho 410 nm optical transitions between ground and excited states	43
4.3 Ho 416 nm optical transitions between ground and excited states	51
4.4 Summary	53
5 MOT characteristics	54
5.1 Overview	54
5.1.1 Laser cooling	54
5.1.2 Magneto-optical trapping	55
5.2 Sub-Doppler cooling	59
5.3 MOT Initial Result	63
5.4 First trap operation	64
5.5 Imaging System	64
5.6 MOT characteristics	65
5.7 MOT population and density	66
5.8 Optimising the MOT population	68
5.9 Trap temperature	69
5.9.1 Sub-Doppler Cooling	70
5.10 Characterization of Repumper	72
5.11 Absorption Imaging Analysis	73
5.12 Summary	76
6 Optical Pumping	77
6.1 Theoretical Model	77
6.2 Optical Pumping in Holmium	79
6.2.1 $\sigma+$ polarized laser beam case	79
6.2.2 π -polarized laser beam case	81
6.3 Summary	82

Appendix

	Page
7 Summary and Outlook	84
7.1 Summary	84
7.2 Outlook	85
LIST OF REFERENCES	86
APPENDICES	
Appendix A: Laser Stabilization	92

DISCARD THIS PAGE

LIST OF TABLES

Table	Page
1.1 rare earth elements experiment table	5
1.2 Charateristics of rare earth MOTs	6
1.3 Holmium properties	6
1.4 Ho cooling transitions	8
3.1 PPKTP crystal parameters	25
3.2 Ho laser system table	39
4.1 hyperfine constants in references	44
4.2 transition strengths of 410 nm transitions	45
4.3 hyperfine shifts of ground and excited states of Ho	45
4.4 hyperfine shifts of 22 optical transition lines	48
4.5 Results of excited state hyperfine constants	51
4.6 transition strengths of 416 nm transitions	52
5.1 Initial MOT parameters	63
5.2 MOT Parameter Set	68
5.3 Landé g-factors of the ground and excited hyperfine states of the cooling transition at 410.5 nm	71

DISCARD THIS PAGE

LIST OF FIGURES

Figure	Page
1.1 a) Conventional encoding in K two-level systems. b) Collective encoding in an ensemble of ($K + 1$)-level systems. c) Collective encoding in an ensemble of ($2K + 1$)-level systems.	3
1.2 A toy model for the illustration of the collective encoding scheme with pulses 1), 2) and 3)	4
1.3 Hyperfine structure of the Ho $4f^{11}6s^2$ ground state. Qubit assignments 1–60 are indicated together with hyperfine splittings and g factors.	5
1.4 (a) energy structures and transitions of Er (b) energy structures and transitions of Dy	7
1.5 Ho energy levels	9
1.6 Cooling transition energy levels (not to scale)	9
2.1 System Diagram	11
2.2 The home-made oven	13
2.3 vapor pressure of holmium	14
2.4 home made Ho source (a) holmium hollow tube (b) rectangular holmium plate with slowing beam fluorescence	14
2.5 (a)Schematic of the vacuum system with home-made holmium source (b)Picture of the vacuum system with home-made holmium source	15
2.6 (a)The effusion cell opening and shutter without crucible in (b)the Tantalum crucible and custom-made Tantalum plugs(used and new). Note that some residual Ho is accumulated at the bottom of the used plug due to condensation	16
2.7 Emitted Ho atoms/second, and Ho sample lifetime	17

Figure	Page
2.8 (a) magnetic field profile of MOT coils along axial direction (b) magnetic field profile of shim coils	21
3.1 Previous Laser System	22
3.2 Big PPKTP cavity and small LBO cavity	24
3.3 single-pass efficiency of PPKTP crystal	26
3.4 Estimated blue output power vs. red input power	27
3.5 schematic layout of the ring SHG cavity	28
3.6 (a) waist size between flat mirrors (b) waist size between curved mirrors	29
3.7 (a) cavity arrangement with unit in m (b) PPKTP cavity assembly with blue light output	30
3.8 (a) waist size between flat mirrors (b) waist size between curved mirrors	31
3.9 Estimated blue output power vs. red input power	32
3.10 cavity arrangement with unit in m	33
3.11 phase-matching angle for LBO vs. wavelength at 20°(blue),30°(red), and 40°(yellow).	35
3.12 (a) waist size between flat mirrors (b) waist size between curved mirrors	35
3.13 (a) cavity arrangement with unit in m (b) LBO cavity assembly (top view)	36
3.14 Estimated blue output power vs. red input power	36
3.15 Laser setup with Ti:Sa laser and home-made LBO cavity	37
3.16 410.5 nm laser system layout	40
3.17 Beams layout at the MOT chamber	40
4.1 Ho zero-field hyperfine spectrum for the 410.5 nm transition. (a)experimental spectrum of 5 successive scans (b)fit to experiment curve with excited state A' and B' from Hancox. Note: the other 11 hyperfine peaks extending toward the lower frequency side are cut off in this spectrum.	46

Appendix

Figure

Page

4.2	hyperfine spectroscopy setup	47
4.3	(a) theoretical overall absorption curve (b) experimental overall absorption curve . . .	47
4.4	Modulation transfer spectroscopy setup	49
4.5	Spectroscopy of the frequency scan including 8 strong transitions of $F \rightarrow F + 1$ transitions, namely $F_g = 4 \rightarrow F_e = 5, \dots F_g = 11 \rightarrow F_e = 12$, and 2 weak transitions of $F_g = 5 \rightarrow F_e = 5$ and $F_g = 6 \rightarrow F_e = 6$. Frequency markers are labeling transition frequencies derived with Hancox's hyperfine constants(red), measured experimentally(green), and derived with hyperfine constants fit to measurement(purple).	50
4.6	Spectroscopy of the frequency scan including 5 weak transitions of $F \rightarrow F$ transitions, including $F_g = 5 \rightarrow F_e = 5, \dots F_g = 9 \rightarrow F_e = 9$, and 2 strong transitions of $F_g = 10 \rightarrow F_e = 11$ and $F_g = 11 \rightarrow F_e = 12$. Frequency markers are labeling transition frequencies derived with Hancox's hyperfine constants(red), measured experimentally(green), and derived with hyperfine constants fit to measurement(purple).	51
4.7	Spectroscopy of the frequency scan for the 8 strong transitions, taken on the hollow-cathode Ho lamp.	53
5.1	Scattering force as a function of velocity for two counter propagating laser beams with $I/I_s = 1, \Delta = -\gamma/2$	57
5.2	1D example of the MOT. Laser beams with opposite polarizations onto an atom from opposite directions. The lasers excite the $J=0$ to $J=1$ transition. The laser beam from the right only excites the $m = -1$ excited state, and the laser from the left only excites the $m = +1$ state. As the atom moves, these levels are shifted by the B field therefore affecting the respective photon scattering rates. The result is a position-dependent force that pushes the atoms into the center.	59
5.3	Principal arrangement of the MOT	60
5.4	initial MOT picture	63
5.5	imaging system layout	65
5.6	(a) a picture of the imaging system (b) a USAF test image with this imaging system . .	65

Appendix

Figure

	Page
5.7 (a) A picture of the MOT inside the vacuum chamber (b) Gaussian fit to the MOT fluorescence image	66
5.8 an example result of temperature measurements (a) Gaussian fit to MOT width at different TOF (b) fit width of MOT and temperature curve fit to data	71
5.9 MOT temperature vs cooling light detuning (a) taken at $s = 1.1$ (b) taken at $s = 1.5$. .	72
5.10 level diagram and transitions of the cooling and repumping transitions	73
5.11 MOT population vs. repumper detuning, with slowing beam off, taken at different repumper beam powers from 0 to 15 mW.	74
5.12 level diagram and transitions of the cooling and two probe beam transitions	75
5.13 Absorption imaging pictures (a) background image (I_b) (b) probe beam image (I_P) (c) signal image (I_s)	75
5.14 Gaussian Fits to the absorption images (a) in vertical direction (b) in horizontal direction	76
6.1 $\sigma+$ case Holmium optical pumping. Orange lines represent the π -polarized microwave field, deep blue lines represent the $\sigma+$ repumping field, and light blue lines represent the $\sigma+$ pumping field.	80
6.2 (a) Population of all F states (b) Population of target state.	81
6.3 π case Holmium optical pumping. Orange lines represent the π -polarized microwave field, deep blue lines represent the π repumping field, and light blue lines represent the π pumping field.	82
6.4 (a) Population of all F states (b) Population of target state.	83
A.1 Optics Layout of the PDH lock	93
A.2 error signal and cavity transmission signal before and after the laser is locked	95
A.3 Noise Spectrum at low frequencies when laser is locked	96
A.4 Circuit Layout	97
A.5 Circuit Layout	98

Appendix Figure	Page
A.6 schematic ring-cavity layout of M Squard Ti:Sa laser [1]	99
A.7 Modulation transfer spectroscopy setup	100

LASER COOLING AND MAGNETO-OPTICAL TRAPPING OF HOLMIUM ATOMS

Jinlu Miao

Under the supervision of Professor Mark Saffman

At the University of Wisconsin-Madison

This thesis covers the detailed design and construction of the experimental apparatus and methods developed for laser cooling and magneto-optical trapping Holmium atoms. The trapping apparatus including the laser systems and the UHV vacuum system to produce the Ho MOT are discussed. The Ho MOT at 410.5 nm transition with 32 MHz linewidth was realized without repumping lasers. A MOT with population of $\sim 10^6$ atoms was formed from 1.5 W of 410 nm blue light, with atom density of $\sim 10^{10}/cm^3$. Sub-Doppler temperatures in the MOT were observed. The effect of the redundant repumping beam on the MOT population was also discussed.

Hyperfine spectroscopy of the strong transition at 410.5nm and a comparably strong transition at 416 nm were obtained and discussed.

A theory was developed for analyzing an optical and microwave approach to optical pumping into a single Zeeman sublevel in the 128 hyperfine ground state manifold of Holmium atoms, for state preparation of a collectively encoded quantum register.

Mark Saffman

Chapter 1

Introduction

1.1 Quantum computing

Quantum computation uses the fundamental concepts of quantum mechanics, such as superposition, entanglement, uncertainty principle, etc., to process data. The idea of the possibility of quantum computers was first conceived by Feynman [2]. Then in 1985 David Deutsch introduced the quantum parallelism method[3], by which certain probabilistic tasks can be performed faster by a universal quantum computer than by a classical computer. Then came Deutsch's algorithm in 1992[4], Shor's algorithm for integer factorization in 1994[5], and Grover's search algorithm in 1997[6].

1.2 Quantum register

Let us start with a classical concept. A bit is just a physical object in state 0 or state 1, such as a capacitor with potential difference 0 or 5V. It represents the fundamental unit of classical digital information. A register is the construction of bit rows of zeros and ones. A quantum bit (qubit) is a physical two-level system, which represents the fundamental unit of quantum information. A qubit can be the electron spin, two hyperfine energy levels of an atom, the photon polarization, the presence or absence of a photon in a cavity, etc. A qubit is encoded in the superposition of the two orthogonal quantum states, represented by

$$|\psi\rangle = C_0 |0\rangle + C_1 |1\rangle \quad (1.1)$$

with $|C_0|^2 + |C_1|^2 = 1$, where $|C_0|^2$ and $|C_1|^2$ represent the probabilities of the measured outcome to be in state $|0\rangle$ and $|1\rangle$. And a quantum register is the construction of multiple qubits. If we take N two-level atoms, then clearly we have 2^N quantum states. Thus the N -bit quantum register can be in any superposition of the 2^N states.

$$|\psi\rangle = C_{0...00} |0...00\rangle + C_{0...01} |0...01\rangle + \dots + C_{1...10} |1...10\rangle + C_{1...11} |1...11\rangle \quad (1.2)$$

There are various approaches for realizing a quantum register: ion traps, neutral atoms and cavity QED, superconducting qubits, solid state qubits(quantum dots), NMR in liquids, etc. Our group has been focusing on the neutral atom approach. There are some minimum requirements that a physical system must satisfy in order to support quantum computing[7]: 1. A scalable physical system with well characterized qubits. 2. Ability to initialize the system to a known quantum state. 3. Large decoherence time compared to gate operation times. 4. A universal set of quantum gates. 5. A readout method.

1.3 Motivation

A quantum register built with atoms does not have to be a collection of atoms with the same two levels. Atoms sharing a single large energy manifold can also be used as a collection of qubits. Instead of individually addressing each atom, an ensemble of atoms share the same set of complex set of ground state manifold can be collectively addressed by applying globally applied control pulses. Fig. 1.1 shows three different ways of encoding a K-bit state $|01....001\rangle$ [8]. In c), the states $|0\rangle$ plays the role of an atomic reservoir.

1.3.1 Collective encoding with Rydberg blockade

The idea of using dipolar Rydberg interactions for neutral atom quantum gates was introduced in 2000 [9], and it was shown that this can be directly extended to ensemble qubits, each consisting of N atoms by Lukin et al. [10]. The idea relies on the concept of collective Rydberg blockade whereby excitation of a single atom to a Rydberg state can block the subsequent excitation of a large number of atoms within the so-called Rydberg sphere. The long range Rydberg interactions

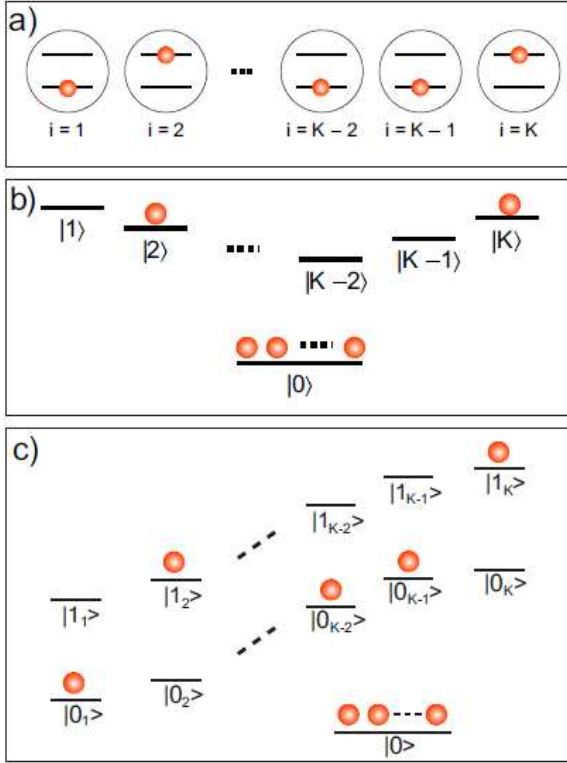


Figure 1.1 a) Conventional encoding in K two-level systems. b) Collective encoding in an ensemble of $(K+1)$ -level systems. c) Collective encoding in an ensemble of $(2K+1)$ -level systems.

together with the availability of a strong and controllable blockade interaction opens up the possibility of collectively encoded multi-qubit register. As suggested in [10, 11], assuming that any of the stable single-atom states can be coupled coherently to the Rydberg state $|r\rangle$, the rotation of the i th qubit in the ensemble representation is accomplished by applying the following pulses (sketched in fig. 1.2: 1) a resonant π pulse transfer of the level population in $|i\rangle$ to $|r\rangle$, 2) a coherent, resonant transition in the closed two-level system with zero and one atom in state $|r\rangle$ (the desired qubit operation), blocking further transfer of atoms to the Rydberg state, and 3) a resonant π pulse transfer of the level population in $|r\rangle$ back to $|i\rangle$. Note that in the above three steps, only 2) is globally applied pulse, 1) and 3) are both applied as if to single atoms. During 2), the Rydberg blockade scheme makes sure that no more than one atom is excited to the Rydberg state.

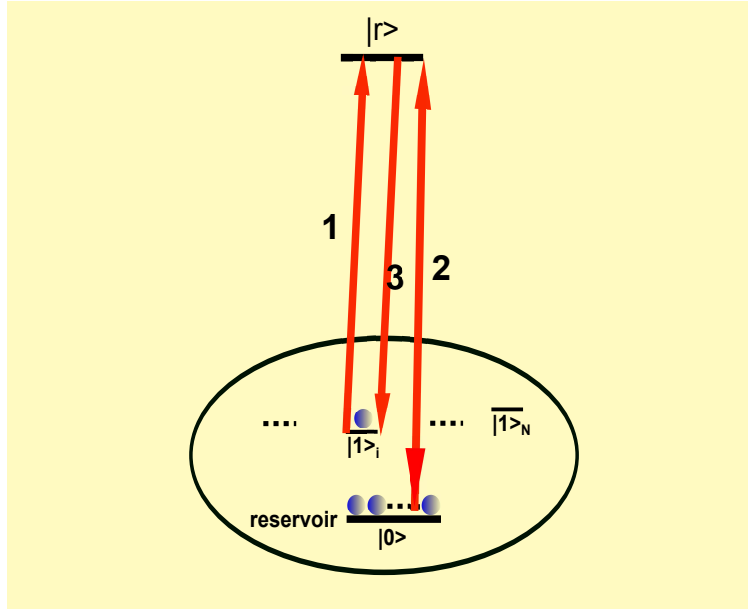


Figure 1.2 A toy model for the illustration of the collective encoding scheme with pulses 1), 2) and 3)

1.3.2 Why holmium

For the collective encoding discussed above, the states $|0\rangle$ and $|1\rangle$ can be chosen as the Zeeman sub-levels of hyperfine ground states of the atoms. Holmium as an element has the largest number of hyperfine ground states, which opens up the possibility to build a large scale 60-bit quantum register by a collective encoding scheme[11, 12], which makes use of the long range Rydberg dipole-dipole interactions. The system can be encoded without individually addressing each qubit. Fig. 1.3 shows a 60-bit encoding with two states per qubit. The implementation of 60 qubits in a small trapped ensemble of holmium may be possible. And cooling and trapping holmium should be possible since several rare earth elements have been successfully laser cooled and trapped in recent years (discussed in the following section).

1.4 Laser cooling of rare earth atoms

Up to date four rare earth elements have been laser cooled and trapped, they are Er[13], Dy[14], Tm[15], and our recently trapped holmium. A variety of experiments have been done on these

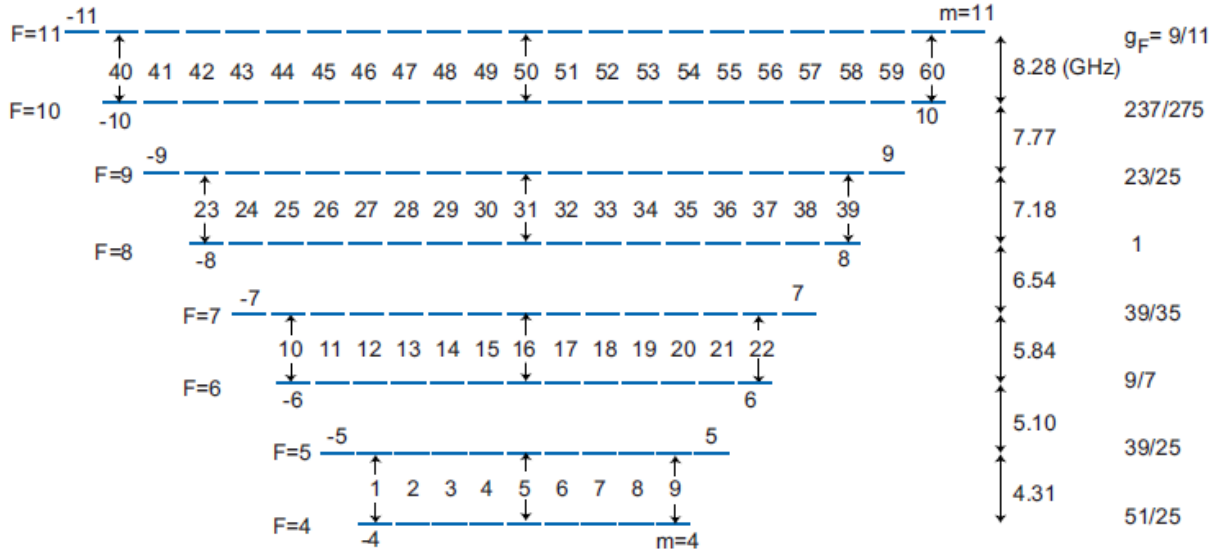


Figure 1.3 Hyperfine structure of the Ho $4f^{11}6s^2$ ground state. Qubit assignments 1–60 are indicated together with hyperfine splittings and g factors.

rare earth MOTs: narrow line cooling with Er[16] and Dy[17], Bose-Einstein Condensation of Erbium[18] and Dy[19], and quantum degenerate dipolar fermi gas with Dy[20]. Table 1.1 shows the recent achievements with rare earth elements. Table 1.2 shows the population, density, temperature achieved in the rare earth MOTs, together with the Doppler temperature and magnetic moments of those elements.

Table 1.1 rare earth elements experiment table

Element	MOT	Narrow line cooling	BEC	DFG
Er	•	•	•	
Dy	•	•	•	•
Tm	•			
Ho	•			

It has been shown that for rare earth atoms, despite of the existence of many metastable levels in between the ground state and the excited state of the cooling transition, no repumper is needed

Table 1.2 Charateristics of rare earth MOTs

Element	Population	Density(cm^{-3})	T(μK)	$T_D(\mu K)$	$\mu(\mu_B)$
Er(NIST)	$\sim 10^6$	$\sim 10^{11}$	~ 100	860	7
Er(Innsbruck)	$\sim 10^8$	$\sim 10^{11}$	10		
Dy	$\sim 10^8$	$\sim 10^{10}$	~ 1000 (majority)	770	10
Tm	$\sim 10^4$	—	~ 100	240	4
Ho	$\sim 10^6$	10^{10}	~ 100	780	9

to for a MOT because of a recycling mechanism [13]. Ho is supposed to have very similar energy structures to its two neighboring elements Er and Dy. Fig. 1.4 shows the energy structures and transitions in Er and Dy.

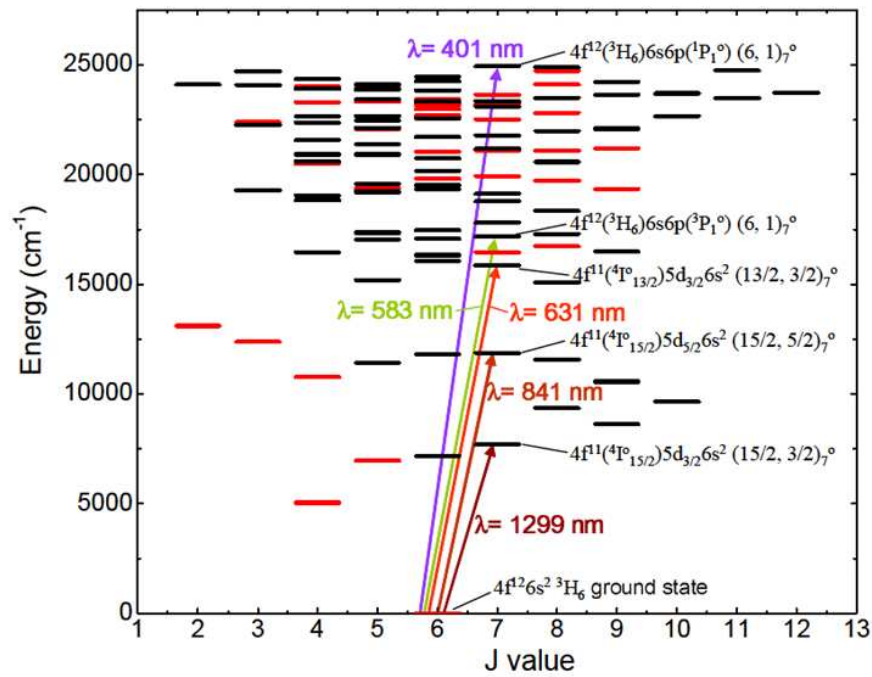
1.4.1 Holmium

Holmium(Ho) is a rare earth element with atomic number 67. It has a melting point of 1461 °C. In order to produce the atom gas with enough number of Ho atoms, we need to heat up the solid Ho source to a high temperature because of its low vapor pressure. Ho is measured to have similar working mechanism with the other magneto-optically trapped rare earth elements. Table 1.3 shows some general and physical properties of holmium [21].

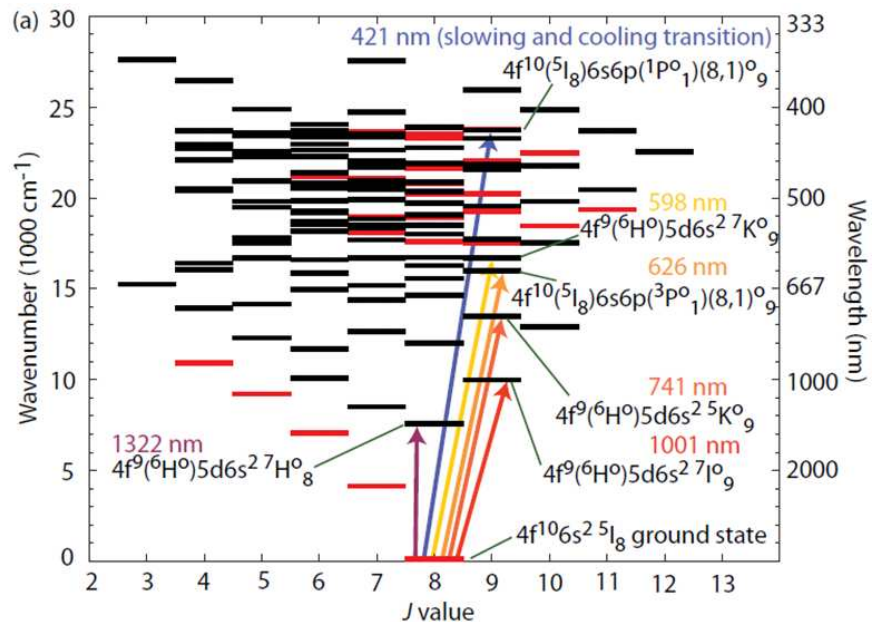
Table 1.3 Holmium properties

standard atomic weight	element category	phase	density (near r.t.)
164.93032	lanthanide	solid	$8.79 g \cdot cm^{-3}$
liquid density (at m.p.)	melting point	boiling point	heat of vaporation
$8.34 g \cdot cm^{-3}$	$1461^\circ C, 1734 K$	$2720^\circ C, 1993 K$	$265 KJ \cdot mol^{-1}$

Ho has one stable isotope ^{165}Ho (boson), with nuclear spin of $I = 7/2$ and a ground electronic configuration $4f^{11}6s^2$. The ground state term is $^4I^0, J = \frac{15}{2}$ with configuration of $4f^{11}(^4I_{15/2}^0)6s^2$. The corresponding energy levels are shown in Fig 1.5. [12]. Transitions suitable for laser cooling and trapping are labeled (a)-(g) between ground state $J = 15/2$ and excited state $J = 17/2$. The



(a)



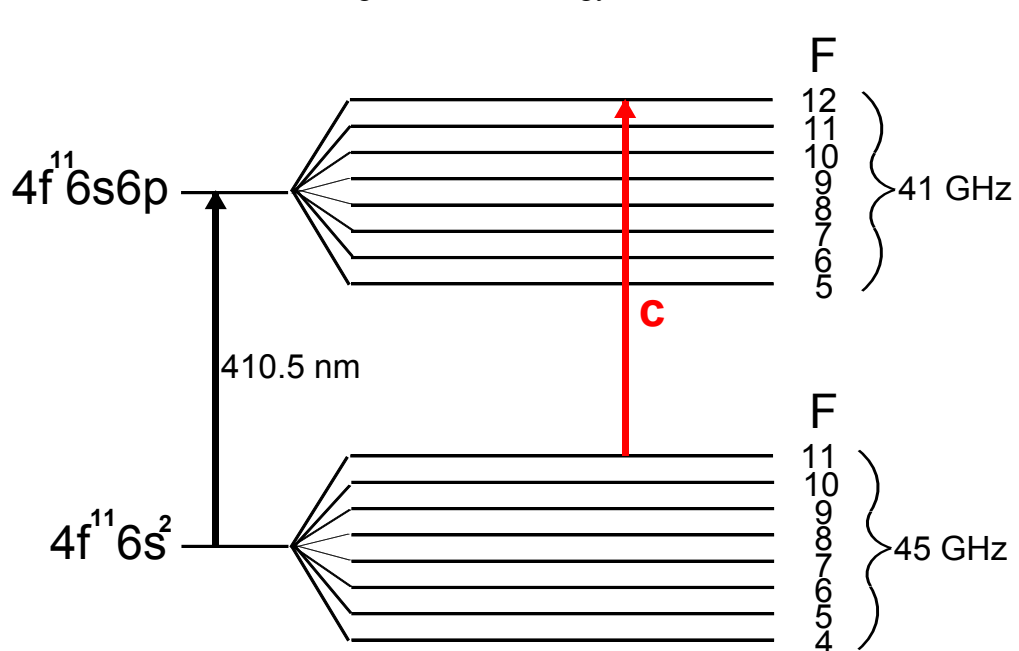
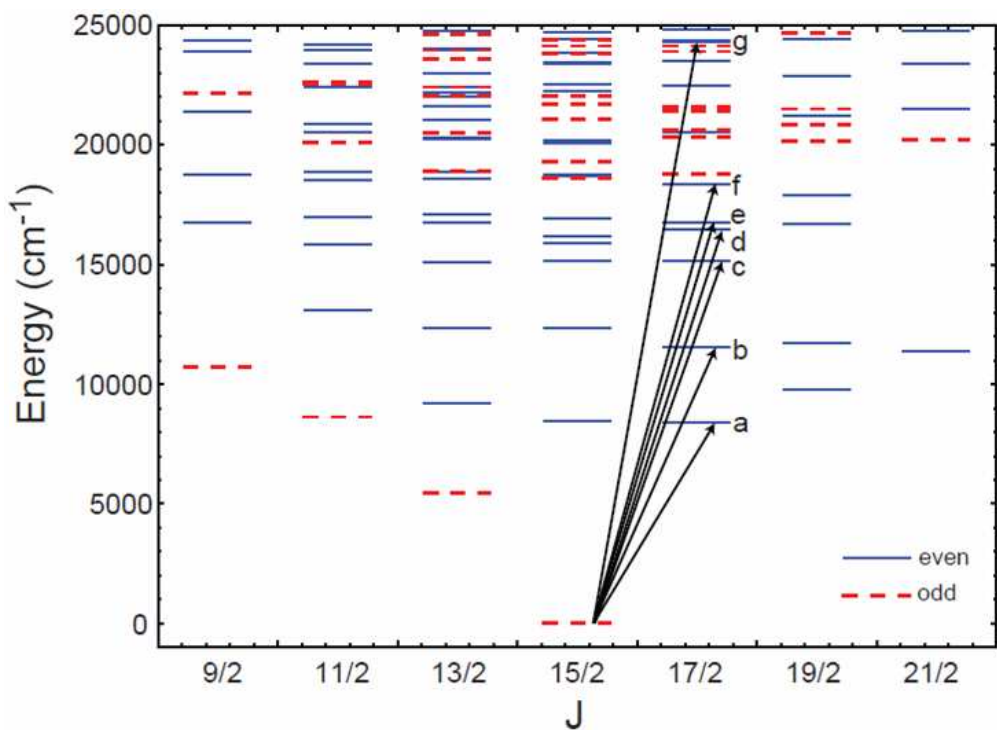
(b)

Figure 1.4 (a) energy structures and transitions of Er (b) energy structures and transitions of Dy

transitions (a)-(f) are closed transitions. According to selection rules, the parity of the ground and excited states must be different, and there are no odd parity excited states for them to decay to. Table 1.4 shows the wavelengths of the suitable cooling transitions. Transitions (a)-(d) have an upper level configuration of $4f^{10}5d6s^2$, which is dipole allowed, but has small oscillator strengths to the ground state. Transitions (e) and (f) have an upper level configuration of $4f^{10}6s6p$ and are coupled more strongly with the ground state. But due to the unknown and very narrow linewidth of the transitions (a)-(f), the strong transition (g) to $4f^{11}6s6p$ at 410.5 nm with a linewidth of 32 MHz is picked for MOT cooling beams, which gives the largest possible number of trapped atoms. Although transition (g) is not a closed transition like (a)-(f), atoms may decay to any of the metastable states between the ground state and the open excited state and lead to atom loss. But we consider the leakage to other metastable states to be very small. In addition the strong magnetic dipole moment($9 \mu_B$) of Ho gives a strong magnetic trapping force, which enables the untrapped atoms in those metastable states to remain confined in the dark states and eventually decay back to ground state and get recycled, thus retrapped by the MOT [13]. Therefore in principle no additional lasers are required. Fig. 1.6 shows the energy levels of the 410.5 nm cooling transition. The cooling laser couples the ground hyperfine state $|F = 11\rangle$ and the excited hyperfine state $|F' = 12\rangle$.

Table 1.4 Ho cooling transitions

Transition	Excited State Configuration	$\lambda(nm)$	$\gamma/2\pi(MHz)$	Doppler limit(μK)
a	$4f^{10}(^5I_8)5d_{\frac{3}{2}}6S^2$	1193	unknown	
b	$4f^{10}(^5I_8)5d_{\frac{5}{2}}6S^2$	867.3	unknown	
c	$4f^{10}(^5I_7)5d_{\frac{3}{2}}6S^2$	660.9	unknown	
d	$4f^{10}(^5I_7)5d_{\frac{5}{2}}6S^2$	608.3	0.04	0.95
e	$4f^{11}(^4I_{15/2}^0)6s6p(^3P_1^0)$	598.5	0.15	3.5
f	$4f^{11}(^4I_{15/2}^0)6s6p(^3P_2^0)$	545.3	unknown	
g	$4f^{11}(^4I_{15/2}^0)6s6p(^1P_1^0)$	410.5	32	780



1.5 Summary

This chapter covers a little bit of introduction about collective encoding in quantum computing and our motivation of choosing holmium, an introduction about holmium. And laser cooling and trapping of other rare earth atoms are compared with holmium. The potentially suitable cooling transitions for holmium are dicussed.

Chapter 2

Vacuum System

2.1 Overview

Fig 2.1 shows the schematic of our vacuum system. The high temperature effusion cell generates a hot beam of Ho atoms. The effusion cell oven is typically running at 1150 °C to 1180 °C. The atoms are slowed and cooled by a red detuned "slowing beam" opposing the atomic beam direction, then pass through a 2.5-mm aperture to enter the MOT chamber and get trapped by a large gradient MOT.

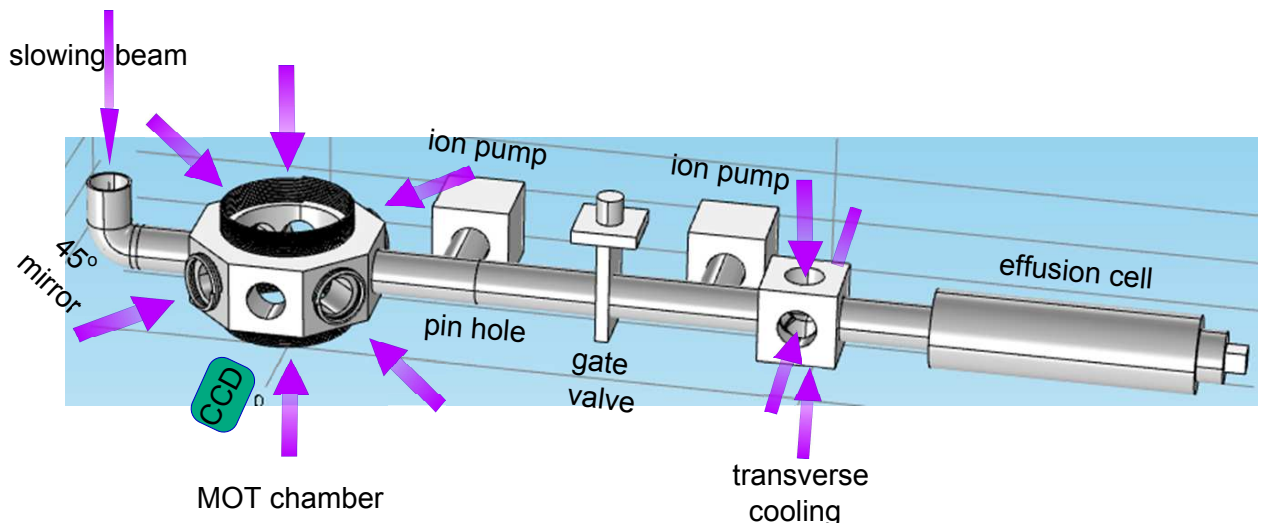


Figure 2.1 System Diagram

The vacuum system contains three main sections: high-temperature effusion cell(with a port aligner and mechanical shutter), transverse cooling section(not in use so far), and MOT trapping

chamber. Two ion pumps, 35 L/s in the MOT region and 20 L/s in the source region are mounted and separated by a gate valve.

This system was baked in a home-made oven made with insulation fiberglass and heating plates for about a week. The various parts of the vacuum system have different temperature ratings. The baking temperature is mainly limited by the view ports and the valves with viton rings. A target temperature of $\sim 200\text{ }^{\circ}\text{C}$ was used in the baking ramp. Due to the offset the actual maximum temperature reached was about $\sim 185\text{ }^{\circ}\text{C}$. Some small parts without windows(crucible, crucible plug, etc.) were pre-baked to a higher actual temperature of $\sim 320\text{ }^{\circ}\text{C}$ with a recipe target temperature of $400\text{ }^{\circ}\text{C}$ before assembling. The gate valve was open while baking. The basic procedure of the baking is to first pump down the vacuum system connected to a turbo pump through the oven wall for about 20 hours. Then do a leak check with acetone in a syringe. Then close up the oven front wall and start the baking recipe with a slow ramp(both up and down) of no more than $15\text{ }^{\circ}\text{C}/\text{hr}$ to avoid window cracks. When the baking is complete, close both of the angle valves to the turbo pump and detach the vacuum system from the oven. Note that several mechanical parts need to be removed before baking, such as the magnets on the ion pumps, plastic turning knobs on the gate/angle valves, and the motor on the effusion cell. The vacuum grease on the turning screws of the valves evaporates during the bake-out. After baking, reapply some if needed before putting the plastic knobs back on. Another thing to keep in mind is that the fiberglass might cause irritation. Therefore it is recommended to wear latex gloves when working with the oven. Fig. 2.2 shows the home-made oven with the vacuum system being pumped inside.

2.2 Holmium source: initial Attempts

Ho has high melting point of $1461\text{ }^{\circ}\text{C}$. fig. 2.3 shows the vapor pressure of Ho vs. temperature [22]. To achieve high enough holmium atom number, we need to heat up solid holmium to above $1100\text{ }^{\circ}\text{C}$. We had tried different versions of setups not only for the laser system but also for the vacuum system before getting the MOT. A summary of what we tried before is as following: we constructed a home-made Holmium source which is a solid Ho piece of either a hollow cylindrical tube or a rectangular plate that connects to a pair of electrical feedthroughs. The tube version of



Figure 2.2 The home-made oven

holmium did not reach a high enough temperature. An estimated temperature of about $800\text{ }^{\circ}\text{C}$ was reached, with DC current close to the upper limit of the power supply (130 A DC). Fig.2.4 and fig. 4.2 shows the previous Ho sources and vacuum system used. The thin plate version of holmium tube has larger resistance due to the small cross section, and reached a higher temperature. We observed fluorescence signals all the way down to the MOT chamber. But the material lifetime was short. After about twenty to thirty hours of operation, the plate got very thin, and reached melting point in the middle and then broke. It was inconvenient for us to constantly break the vacuum and replace the holmium source. In addition, there was no water cooling systems for this high temperature holmium source, so that the connections joining the feedthroughs and the cables got so hot that they melted the cable insulation skin near the feedthroughs which was dangerous. And the laser system back then when we were using this vacuum source setup had low power output (can only provide about 10 to 15 mW in each MOT beam and about 3 mW in the slowing beam), plus the power degraded during the day due to the PPKTP thermal effect (will be discussed later). Only fluorescence signal was seen with this setup. Although the low laser beam power was most likely the main reason that we did not see the MOT, the vacuum system needed modification as well. We need a vacuum system with a good holmium atom source that could provide high

temperature, long material lifetime, and safty water cooling system. Eventually we decided to replace our home-made holmium source setup with a commercial high temperature effusion cell that could satisfy all the requirements we need. And we modified our vacuum chamber system according to the mounting needs of this cell.

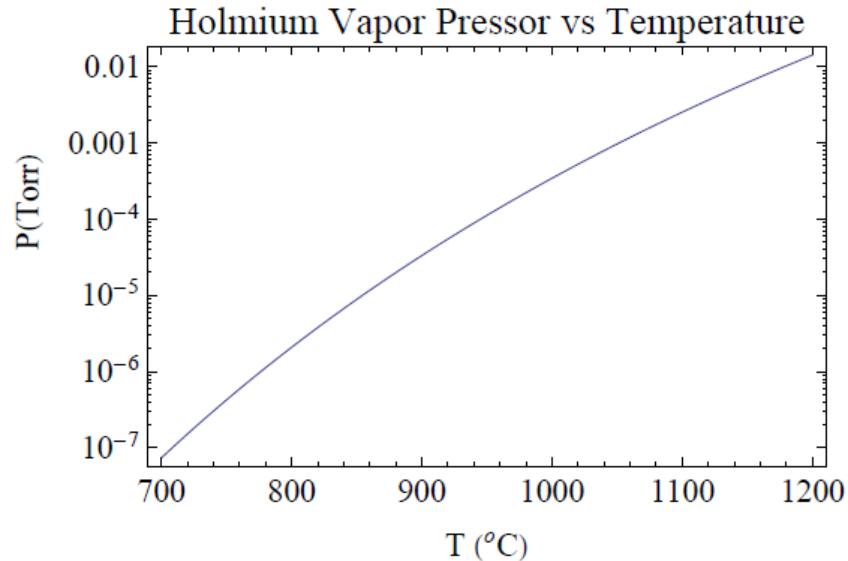


Figure 2.3 vapor pressure of holmium

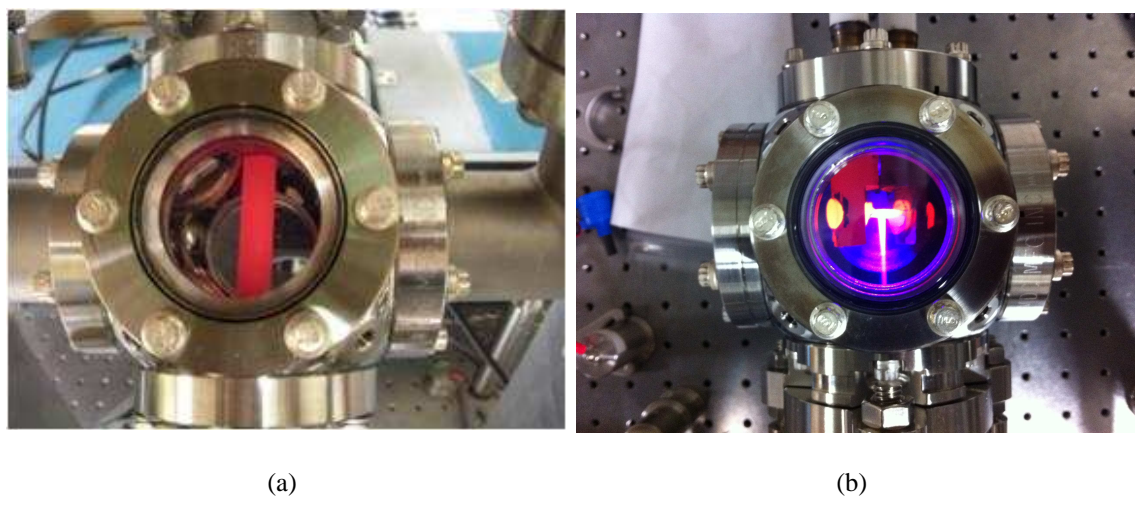


Figure 2.4 home made Ho source (a) holmium hollow tube (b) rectangular holmium plate with slowing beam fluorescence

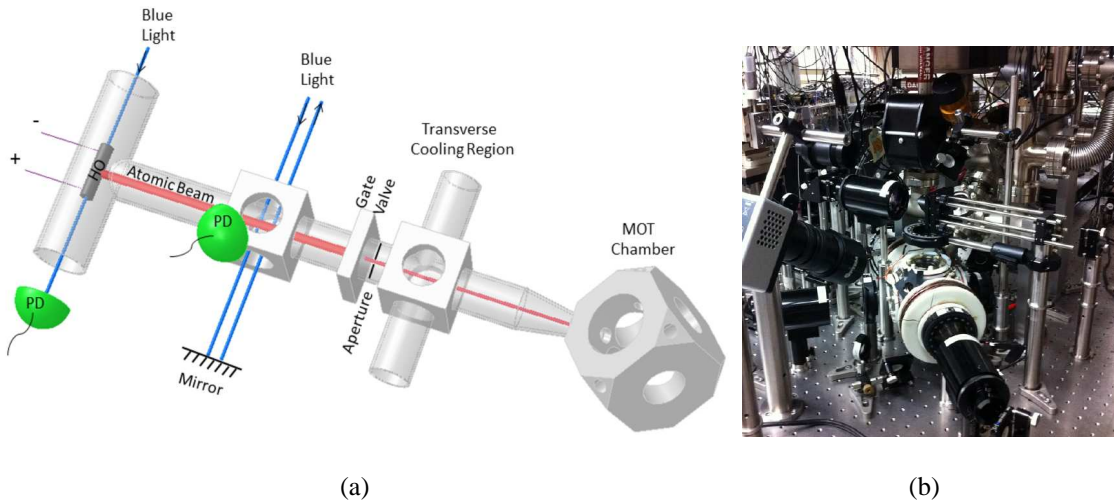


Figure 2.5 (a)Schematic of the vacuum system with home-made holmium source (b)Picture of the vacuum system with home-made holmium source

Handling holmium requires extra care [23]. Holmium can oxidize rapidly, burn under fire conditions. May react with water liberating flammable, explosive hydrogen gas. For ultrasonic cleaning, pure Acetone and Isopropanol can be used, without turning on the heat of the ultrasonic cleaner. And one should wait for the solvent in the cleaner to cool down before taking holmium out, to avoid interaction with water vapor in the air which might cause fire. Do not use water. Conditions to avoid: Dusting conditions, electric arcs, open flame, spark and moisture. Materials to avoid: Air, strong acids, strong oxidizing agents, acid chlorides, halogens, chloates, bromates, iodates.

2.3 Holmium source: high temperature effusion cell

The effusion cell(CREATEC, SFC-40-10-284-HL-WK-SHE-SC) is designed for evaporation of various materials in the temperature between 200 °C and 1400 °C with temperature stability of < ± 0.1°C depending on the PID controller. The heating system consists of a Tantalum wire heater with PBN insulator rings for electrical isolation. To decrease the material condensation at the orifice, the heating system has a higher power density in the area of the crucible orifice. This

cell is used with a Tantalum crucible inside (Max. temperature of 2000 °C), and is water cooled surrounding the entire cell. The whole system has a bakeout temperature of 200 °C [24].

Since the effusion cell with the crucible inside is mounted horizontally. A tantalum plug with a 2.5-mm hole is custom made to go inside the crucible to prevent liquid Ho from leaking out to the vacuum due to potential local heating higher than the melting point. Fig. 2.6 shows pictures of the effusion cell opening and shutter flag, and the home-made Tantalum plugs. The plug with a small opening extends the life time of loaded holmium pieces, because the majority of hot holmium gas get blocked by the plug, and accumulate at the end of it and eventually get recycled.



Figure 2.6 (a)The effusion cell opening and shutter without crucible in (b)the Tantalum crucible and custom-made Tantalum plugs(used and new). Note that some residual Ho is accumulated at the bottom of the used plug due to condensation

At the output of the crucible, a shutter is integrated into the cell flange. A rotary UHV feedthrough connects to the shutter rod. One can open and close the shutter manually by rotating the knob outside the vacuum or electronically controlling it with the electric motor retrofitted with the shutter feedthrough.

A Ho atomic beam is generated through the orifice of the effusion cell and propagates through another pin-hole of 2.5-mm close to the gate valve and finally reach the MOT trapping chamber. A port aligner(Kurt. J. Lesker, PA35-H) is mounted behind the effusion cell to maximize the number of atoms that reach the MOT trapping chamber.

When the effusion cell is running at $1150\text{ }^{\circ}\text{C}$, we achieve a vacuum of $\sim 10^{-9}$ Torr at the ion gauge in the MOT chamber, with the use of a 35 L/s ion pump. A gate valve mounted between the MOT trapping region and the effusion oven region is for maintaining the low pressure in the MOT vacuum chamber while the source region is heated and is high in pressure. A second ion pump of 20 L/s is mounted before the gate valve and the ion gauge of it reads $\sim 10^{-8}$ Torr. The figure below shows the vapor pressure of solid holmium vs temperature.

The orifice is about 2.5 mm. When the solid pieces of holmium (company: ESPI, Electronic Space Products International) were heated in the crucible, the number of atoms that escape in time t , through this orifice, assuming ideal gas condition, is given by [25]

$$N_{escape} = At \frac{1}{4} \frac{P}{KT} \bar{v} \quad (2.1)$$

where $\bar{v} = \sqrt{\frac{8KT}{\pi m}}$ is the average velocity, A is the area of the orifice, and K is the Boltzmann constant. The crucible is filled with ~ 20 g of holmium pieces. Assume we run the effusion oven at $1150\text{ }^{\circ}\text{C}$, for 8 hours a day, then the sample would last 116 days. Fig. 2.7 shows the emitted Ho atoms/second through the orifice and the total sample lifetime vs running temperature(assuming 8 running hours/day).

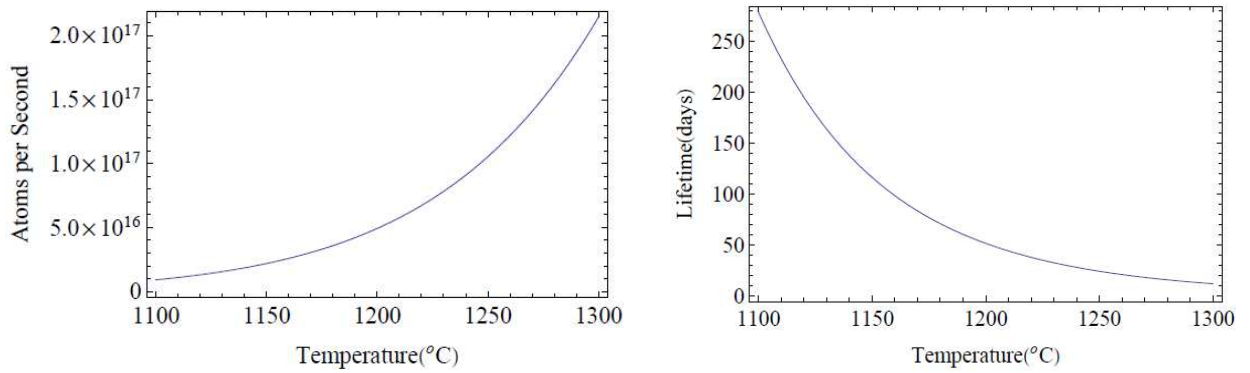


Figure 2.7 Emitted Ho atoms/second, and Ho sample lifetime

2.4 Atomic beam collimation and slowing

To efficiently couple an atomic beam source to a MOT, we must efficiently couple the broad velocity distribution of a beam to match to the narrow one of the trap. Small changes in the atomic velocity profile can produce large changes in the loading rate. Furthermore, the angular distribution of a typical atomic beam, is rather broad, collimation of the beam can improve the MOT population in the trapping chamber. So we will add transverse cooling beams later when we have more blue power to spare. In addition, some mechanical ways of collimation can also reduce the angular distribution, such as using a long and narrow channel. In our case we custom-made a 7-inch long collimating tube with a inner diameter of 0.2-inch. Note that the drawback of it is that it suffers from a severe reduction in the flux as the channel length grows. A 7-inch length is supposed to be enough to provide significant collimation and we will want to put it as close to the source as possible (This collimating tube is not mounted on the vacuum system so far).

Atoms coming out from a thermal oven running at above 1100 °C typically have velocities in the range of 400-500 m/s and are too hot to be loaded into a MOT. In order to bring them within the capture velocity range of the MOT (which is about 40 m/s for our case), it is necessary to slow them down before they reach the trapping chamber. This can be done using scattering force from a single counter-propagating laser beam. We achieved efficient pre-cooling with a single slowing beam tuned 320 MHz to the red without using a Zeeman slower. The 32MHz broad linewidth of the 410.5 nm cooling transition helped the efficiency of this pre-cooling with the single-frequency slowing beam. The detuning of the slowing beam is chosen by tuning the frequency of the slowing beam to maximize the MOT population. The power used in this slowing beam is typically about 70 mW. It is chosen by changing the power distribution between the slowing beam and the MOT cooling beams to maximize the MOT population.

2.5 MOT chamber

The MOT chamber is the basic element for preparing a cold atomic gas. A stainless steel octagon chamber(Kimball Physics, MCF600-SphOct-F2C8) with two 6"-diameter CF view ports

on the top and the bottom, and six 2.75" view ports on the sides. Six view ports are for the six orthogonal MOT cooling beams, the other two are for imaging and the slowing beam. Note that to prevent accumulation of Ho on the view port of the slowing beam that leads to reduction of slowing beam transmission through that port, a 45 $^{\circ}$ -mirror is mounted inside the vacuum chamber in a cage system at that port. So the Ho atoms would only coat that tilted mirror without affecting the slowing beam transmission through the viewport window.

For power concern we did not use fiber but directly send the beam off to the MOT area. The beam is first split off a PBS, and then the cooling light is split into two other beams by another PBS. forming a total of three beams with equal intensity. The beam size was expanded to $w = \sim 6\text{mm}$ before splitting. In the MOT chamber fluorescence detection is made by an EMCCD camera. A spare port is saved for shining through the absorption imaging probe beam, on the opposite port from the CCD camera.

A pair of magnetic coils for generating the quadrupole field of the MOT is mounted on the pair of 6" windows. The coils generate a field of about 20G/cm along z-axis, which aligns with the quadrupole axis of symmetry. Each coil has 10 rows(z) and 10 columns(r). 20 A of current runs through this pair of coils and makes the temperature as high as 100 $^{\circ}\text{C}$ during operation. So a new pair of hollow copper coils is made to provide water cooling. Shim coils are mounted onto four side-windows through which the other 4 MOT beams go through, to compensate the residual field at the MOT center.

2.6 Magnetic coils

The MOT coil is a pair of anti-Helmholtz coils through which a current is sent into opposite directions. With the z-axis as the symmetry axis, a weak quadrupole magnetic field is zero at the center $z = 0$ and increases linearly with increasing distance from the center. In the magnetic field the atomic energy levels experience a splitting into Zeeman components with the energies

$$E_i = -\mathbf{p}_m \cdot \mathbf{B} = g_F \mu_B m_F |\mathbf{B}|. \quad (2.2)$$

where μ_B is the Bohr-magneton, F is the quantum number of the total angular momentum including nuclear spin, and m_F is the magnetic quantum number.

For coils that are large compared to the trap size, the field has the form $\mathbf{B} = \frac{b}{2}(-x\mathbf{i} - y\mathbf{j} + 2z\mathbf{k})$ near the center, where b is the field gradient along \mathbf{z} . For the x and y directions, the magnetic field of the anti-Helmholtz coils is a quadrupole field. From Maxwell's equation $\nabla B = 0$,

$$\frac{\partial B_x}{\partial x} = \frac{\partial B_y}{\partial y} = -\frac{1}{2} \frac{\partial B_z}{\partial z}. \quad (2.3)$$

The restoring forces in the x and y directions are therefore half of that in the z direction.

The anti-Helmholtz configuration is advantageous for tight confinement and deep trap depths. A well chosen ratio between axial and radial windings of the coils helps to minimize the power consumption for a given field gradient. When designing the magnetic coils we also need to consider about the limits of size of the coils and the distance between them, which is limited by the chamber size and the power supplies' current ratings, and the need of water cooling.

The MOT coils with holders are directly mounted to the top and bottom windows of the MOT chamber. Additionally three pairs of shim coils are mounted onto the MOT chamber to cancel stray magnetic fields. Along the axial direction, the shim coils are in the additional slots of the MOT coil holders. And the other two pairs of shim coils, we have them wound directly on the windows of the MOT chamber.

For the MOT coils, the design parameters are: inner coil pair separation of 11 cm, coils inner radius of 9 cm, wire width of 0.10 inch, number of turns in both radial direction and axial direction equals 10, current through the coils of 20 A. With the parameters above, the simulated B field profile along the axial direction is shown in fig. 2.8(a). And around the MOT central region, it gives a field gradient of 19.4 G/cm.

A more general approximation using $B = \mu In \times 3 \frac{\frac{1}{2}dR^2}{((0.5d)^2 + R^2)^{5/2}}$ gives a similar result of 19.9 G/cm [26]. A similar simulation can be carried out for the shim coils. The difference is that the shim coils have Helmholtz configuration instead of anti-Helmholtz configuration.

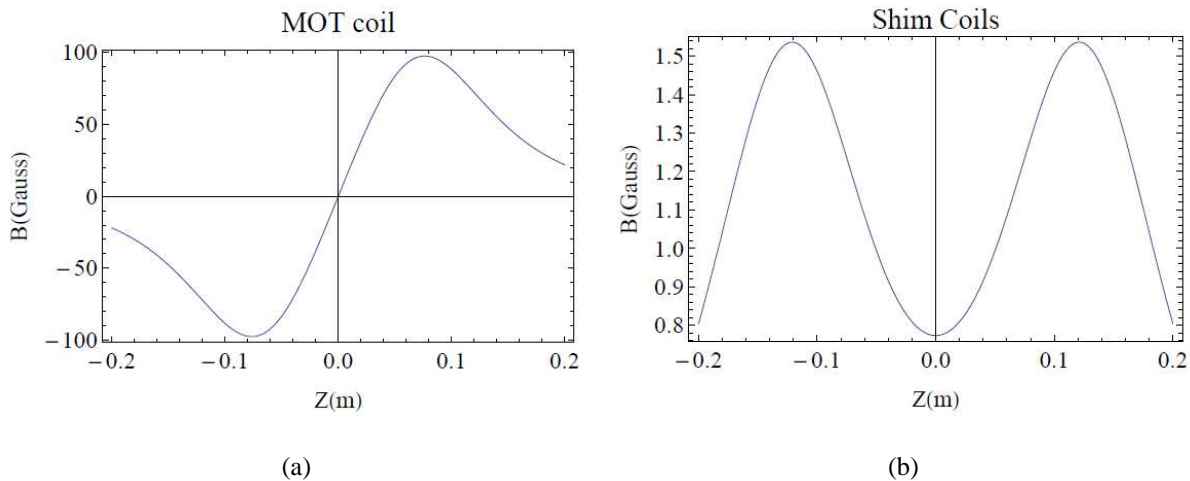


Figure 2.8 (a) magnetic field profile of MOT coils along axial direction (b) magnetic field profile of shim coils

2.7 Summary

This chapter covers our previous vacuum system with home-made holmium sources for some of our hyperfine spectroscopy experiments, and our current vacuum system with commercial effusion cell holmium source and magnetic coils settings for the MOT experiments.

Chapter 3

Laser system

3.1 Overview

3.2 Home-made laser system

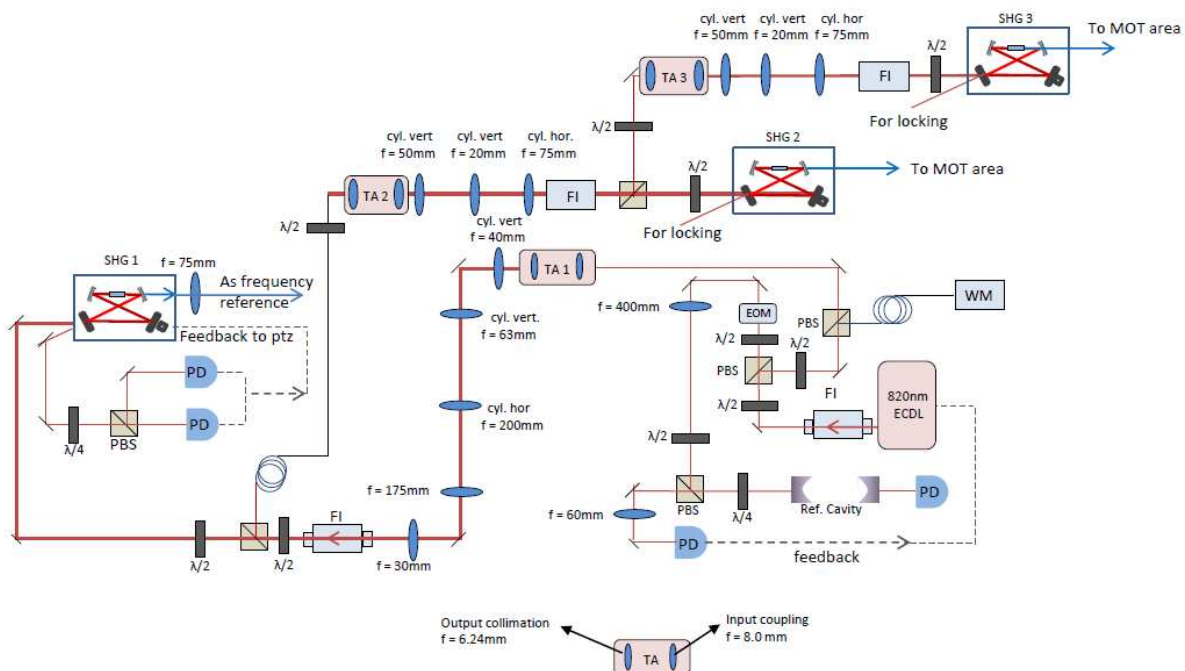


Figure 3.1 Previous Laser System

Using diode lasers with Holmium is difficult by the lack of commercially available high power diodes at 410.5 nm. As commercial diodes nowadays are typically only available with up to 150 mW output power (raw output without external cavity and feedback). We tried a couple of versions

of external cavity diode lasers (ECDL) with blue diode centered at 405 nm, both home-made and commercial. The performance of these blue ECDLs were not satisfying. The power was weak and the frequency stability was bad. It is a good practice to use a tapered amplifier (TA) to increase the amount of light. Since TA in blue light regime is not commercially available so far, we choose to use frequency doubling technique. Fig. 3.1 shows our home-made laser system. A home-made external cavity diode laser (ECDL) at 821 nm is split into three paths through tapered amplifiers (one Toptica TA-0830-0500-4, and two Sacher TPA-0830-1000) to get power enhancement. Three frequency doubling cavities with nonlinear crystals (PPKTP and LBO) are used to produce the 410.5 nm light from the fundamental light at 821 nm. The frequency doubling cavities are locked to the IR laser using Hansch-Couillaud technique. This laser system was close to success of the MOT with a power output of about 150 mW total, but still not strong enough. Then came a brief period of time when we had a combination of commercial Ti:Sa laser (M2 SolsTis) with a Verdi pump laser at 532 nm, and our home-made LBO frequency doubling cavity, that gives us a total of more than 300 mW of blue light. This laser system setup eventually helped us achieved the MOT for the first time. In the end we installed a whole commercial laser system with the home-made LBO cavity also replaced.

The diode laser we use is an external cavity diode laser (ECDL). The light from a commercial laser diode (SANYO DL8142-201) is collimated through a lens (C110-TME-B) and adjustable feedback is provided by a Littman-Metcalf configuration cavity formed by a diffraction grating Edmund NT43-849, gold, 830/mm) and a retro-reflecting mirror. The laser has thermo-electric cooling (TEC) that cools the diode down to temperature around 18 °C for our operation. The central wavelength of the diode was pulled from 830 nm down to 821 nm with the feedback. Typically this diode laser (at 821 nm) has an output power about 64 mW (with raw diode rated for 120 mW). The power output of this diode laser is amplified with three tapered amplifiers to get enhanced output power of about 250 mW in the Toptica TA branch and from 800mW up to 1 W depending on the operation parameters (TA current, seed power, etc.) in the Sacher TA branches. Typically we use about 36 mW seed power for all three TAs.

The tapered amplifier contains a chip with a tapered gain region where the light from the laser which is to be amplified is focused. Two mirrors are used to couple the beam into the TA. After the TA a set of beam correcting cylindrical lenses are used to reduce the ellipticity of the beam profile. And for our case this output out of the tapered amplifier has a 4:1 ellipticity to be corrected. After the beam correction of the output from the first TA, the beam is sent through a fiber onto a bread board, on which two other additional TAs and two home-made SHG cavities are aligned. Depending on different nonlinear crystal (PPKTP or LBO) and the cavity design of different sizes, the output blue power is different. This is to be discussed in the following sections. Fig. ?? shows part of our laser setup with one of the big PPKTP cavities and an LBO cavity.

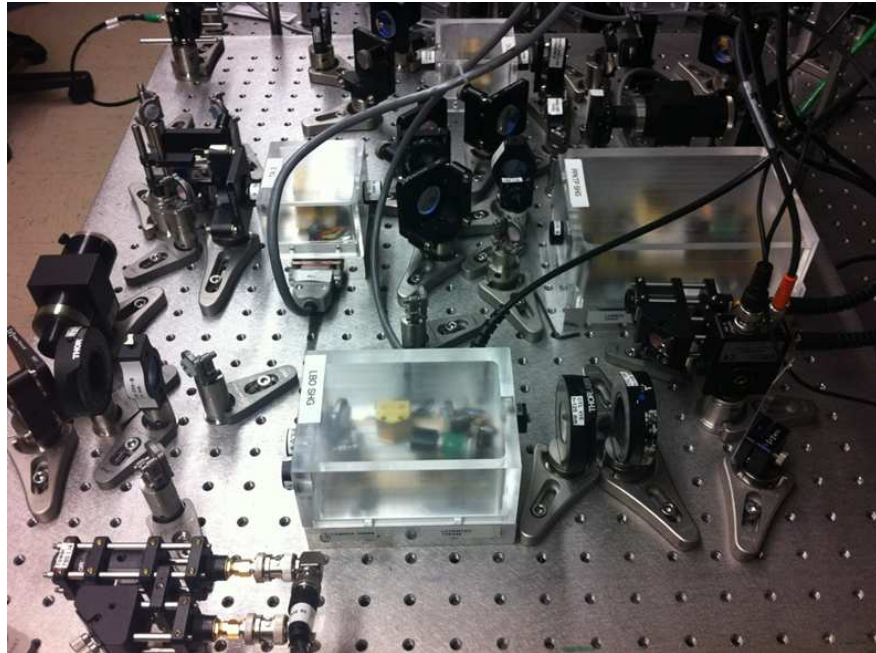


Figure 3.2 Big PPKTP cavity and small LBO cavity

3.3 Periodically poled Potassium Titanyl Phosphate (PPKTP) crystal SHG

The PPKTP crystal has an index of refraction of 1.84 and the crystal length is chosen to be 20 mm. Some relevant susceptibility and mode-matching angle parameters of PPKTP ($d_{33} = 15pm/V$) crystal are shown in table 3.1 [27]. The advantages of using PPKTP crystals are larger

nonlinear susceptibility, non-critical phase-matching which makes getting a reasonable amount of SHG power much easier, no walk-off angle (The birefringence of the crystal causes the energy flow (Poynting vector) of the ordinary and the extraordinary beams to propagate along different directions, and this is called wall-off, which reduces the conversion efficiency because the nonlinear interaction requires overlapping of the o and e beams.), and high conversion efficiency.

Table 3.1 PPKTP crystal parameters

$\vartheta(^{\circ})$	90
$\varphi(^{\circ})$	30
d_{eff}	$\frac{2}{\pi}d_{33}$

3.3.1 Single-pass Conversion efficiency

The single-pass power conversion efficiency is given by

$$E_{NL} \equiv \frac{P_2(L_c/2)}{P_1^2} = \frac{2\omega_1^2 d^2}{\epsilon_0 c^3 n_1^2 n_2} \frac{L_c^2}{\pi w_{01}^2} h \quad (3.1)$$

Where P_1 is the input power of 821 nm light, P_2 is the out put power of 410.5 nm light, L_c is the total cavity length, w_{01} is waist size of fundamental beam in the center of the crystal, ω_1 is the angular frequency of the fundamental beam, n_1 and n_2 are index of refraction of fundamental and harmonic light respectively, d is the effective susceptibility listed in table 3.1 and h is the weak focusing limit.

To get the weak focusing limit h , we need to first determine the Boyd-Kleinman coefficient B [28], which is given by

$$B = \frac{\sqrt{k_1 L_c}}{2} \delta \quad (3.2)$$

Where k_1 is the wave number of the fundamental light in the crystal, and δ is the double refraction angle(walk-off angle). The Boyd-Kleinman $h(B)$, which represents the contributions to the harmonic beam power at different longitudinal positions inside the crystal is given by

$$h = \int_{\xi=-0.5}^{\xi=0.5} \int_{\xi'=-0.5}^{\xi'=0.5} \frac{e^{i\Delta k L_c(\xi-\xi')} e^{-2\frac{L_c}{S_{Rl}} B^2 (\xi-\xi')^2}}{(1 + i\frac{L_c}{Z_{Rl}}\xi)(1 - i\frac{L_c}{Z_{Rl}}\xi')} d\xi d\xi' \quad (3.3)$$

Since PPKTP has no walk-off angle, h is then simplified to

$$h = \int_{\xi=-0.5}^{\xi=0.5} \frac{e^{i\Delta k L_c(\xi)}}{(1 + i \frac{L_c}{Z_{RL}} \xi)} d\xi \quad (3.4)$$

Where Z_{RL} is the Rayleigh length of the fundamental beam, Δ is $\frac{\pi}{L_c}$ for best match. For the PPKTP crystal, considering no walk-off angle, the single-pass efficiency E_{NL} is shown in fig. 3.3. For the first step of the SHG cavity design, an optimal fundamental waist size $w_{01} = 23\mu m$ is chosen to maximize the single-pass efficiency.

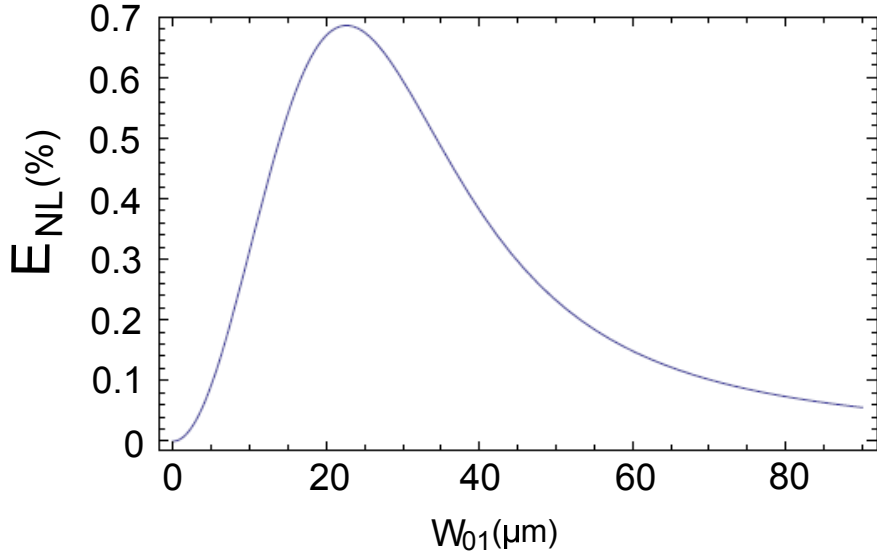


Figure 3.3 single-pass efficiency of PPKTP crystal

3.3.2 Total round trip Conversion Efficiency

The total conversion efficiency is defined as the second-harmonic power output from the cavity divided by the incident fundamental power. By using the ring SHG enhancement cavity, much higher than the single-pass efficiency can be obtained. An advantage of the ring cavity is that the beam travels in only one direction around the ring and no reflection directly goes back into the pump beam source. Assume that the input coupler has a transmission rate T and the ring cavity has internal linear loss L_0 . Then the total conversion efficiency ϵ , which is defined as $\frac{P_{out}}{P_{in}}$, is given by

$$\sqrt{\epsilon} = \frac{4T\sqrt{E_{NL}P_{in}}}{[2 - \sqrt{1 - T}(2 - L_0 - \sqrt{\epsilon E_{NL}P_{in}})]^2} \quad (3.5)$$

where P_{in} is the fundamental beam power. Fig. 3.4 shows an estimation of the output power vs. input power at different input coupler transmission T, assuming a cavity loss of 3.5 %.

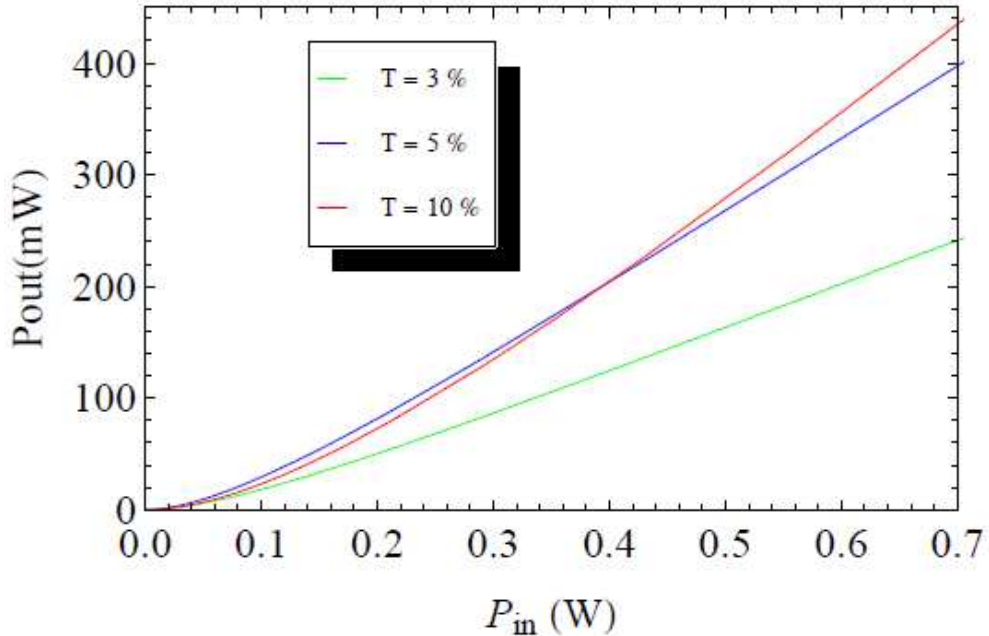


Figure 3.4 Estimated blue output power vs. red input power

3.3.2.1 Cavity set-up

The PPKTP ring cavity is made of two planar mirrors(M1 and M2) and two curved mirrors(M3 and M4) with 25mm radius of curvature. M1 is the input coupler with a measured reflectivity of 94 % at 820 nm. M4 is the output coupler dichromatically coated with high reflectivity for the fundamental beam and high transmission for the second harmonic beam. The round-trip optical length of the cavity is 13.5 cm. The whole cavity is placed on a brass plate which is temperature controlled underneath. The crystal is held in a pentagonal brass housing and put between M3 and M4. The incident angle is 12° . Small incident angle is chosen to reduce astigmatism. The LBO crystal used in this ring cavity has a dimension of 1mm by 2mm by 20mm. A simplified schematic layout of the cavity is shown in fig 3.5

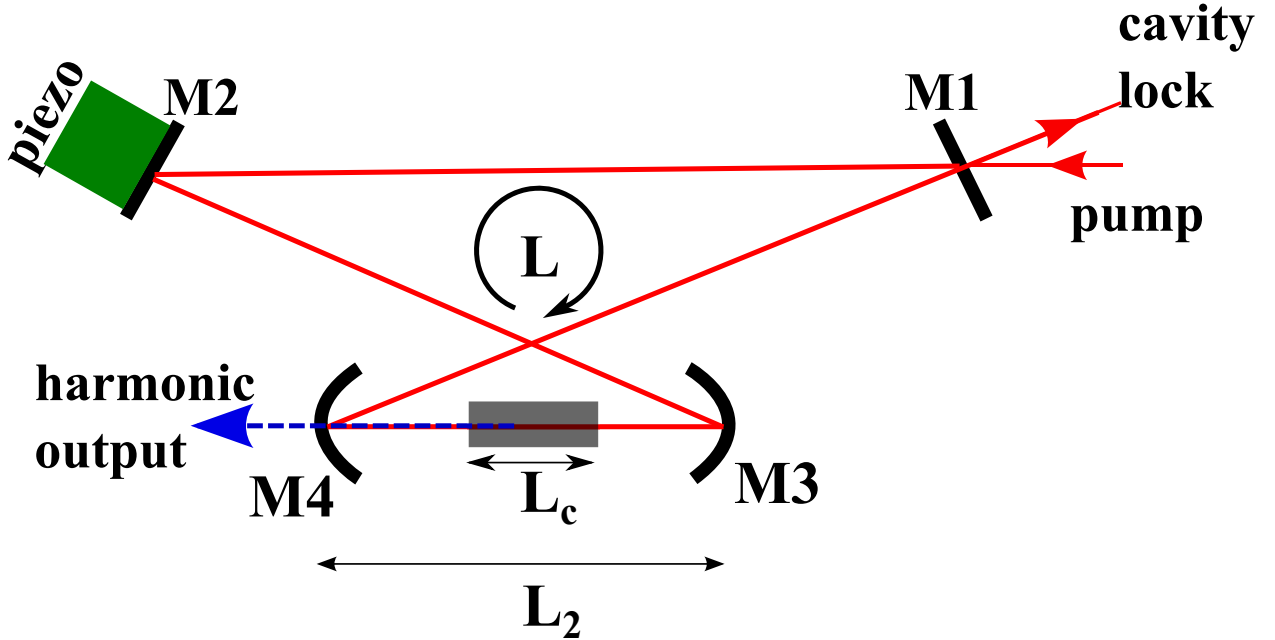


Figure 3.5 schematic layout of the ring SHG cavity

The position arrangement of the cavity mirrors and the crystal is calculated with the ABCD matrix to meet three requirements: the incident beam mode has to match the cavity mode, the fundamental beam waist size in the center of the crystal has the optimized value ($\sim 23 \mu\text{m}$) so that the single-pass conversion efficiency of the second harmonic is maximized, and that the stable cavity condition has to be satisfied. A brief discussion about the ABCD matrix used for this cavity design is as following: assume that the beam starts from the center of the crystal, after a round trip propagation in the cavity, it comes back to the center of the crystal, then the ABCD matrices for the tangential and sagittal propagation is given by

$$M_t = M_L\left(\frac{L_c}{2}\right) M_n(1, n) M_L\left(\frac{L2 - Lc}{2}\right) M_{Rt}(R, \theta) M_L(L - L2) M_{Rt}(R, \theta) M_L\left(\frac{L2 - Lc}{2}\right) M_n(n, 1) M_L\left(\frac{L_c}{2}\right) \quad (3.6)$$

$$M_s = M_L\left(\frac{L_c}{2}\right) M_n(1, n) M_L\left(\frac{L2 - Lc}{2}\right) M_{Rs}(R, \theta) M_L(L - L2) M_{Rs}(R, \theta) M_L\left(\frac{L2 - Lc}{2}\right) M_n(n, 1) M_L\left(\frac{L_c}{2}\right) \quad (3.7)$$

where

$$M_L = \begin{bmatrix} 1 & L \\ 0 & 1 \end{bmatrix}, M_{Rt}(R, \theta) = \begin{bmatrix} 1 & 0 \\ \frac{-2}{R\cos(\theta)} & 1 \end{bmatrix}, M_{Rs}(R, \theta) = \begin{bmatrix} 1 & 0 \\ \frac{-2\cos(\theta)}{R} & 1 \end{bmatrix}, \text{ and } M_n(n1, n2) = \begin{bmatrix} 1 & 0 \\ 0 & \frac{n1}{n2} \end{bmatrix}$$

Figure 3.6 shows the beam waists between curved and flat mirrors vs the distance between the curved mirrors vs. the distance between the curved mirrors, assuming that the total cavity length is fixed at 13.5 cm. The distance between curved mirrors is 3.7 cm, where the tangential and sagittal waists are focused at the same position in the crystal. A coupling lens is put before the cavity for focusing the laser beam down to the required waist size ($\sim 150 \mu\text{m}$) between M1 and M2, so that the wanted waist w_0 in the center of the crystal would be achieved. And A $\lambda/2$ plate right in front of the cavity adjusts the laser polarization to almost parallel to the cavity optical plane to get maximized second harmonic conversion.

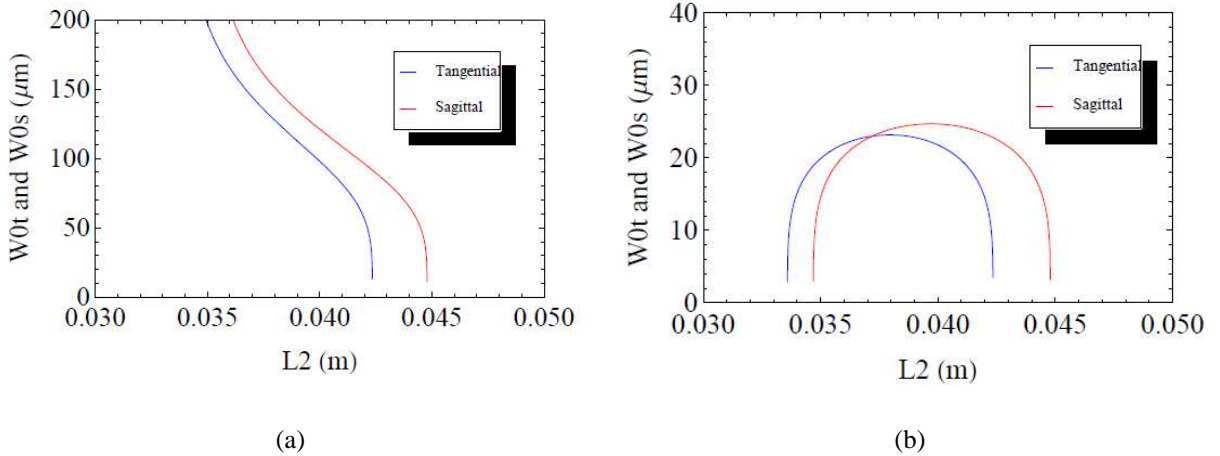


Figure 3.6 (a) waist size between flat mirrors (b) waist size between curved mirrors

The planar mirror M2 has a PTZ allowing to scan the cavity length for locking the SHG to the laser frequency (or atomic error signal). For locking the SHG to the laser, Hansch-Couillaud locking scheme [29] is used. The reflected light from the cavity has a frequency dependent elliptical polarization. A $\lambda/4$ plate followed by a PBS and two photo detectors are placed in the beam path of this reflected beam to get the error signal for electronic frequency stabilization. The biggest

advantage of this locking method is that it is modulation-free. Fig. 3.7 shows a to-scale layout of this PPKTP cavity and a picture of the cavity assembly with blue light generated. Note that in our previous to-scale layout design (not shown), we did not take into account the size of the mirror mounts, so that we had to shift the positions of the mirrors a bit to avoid them from knocking into each other.

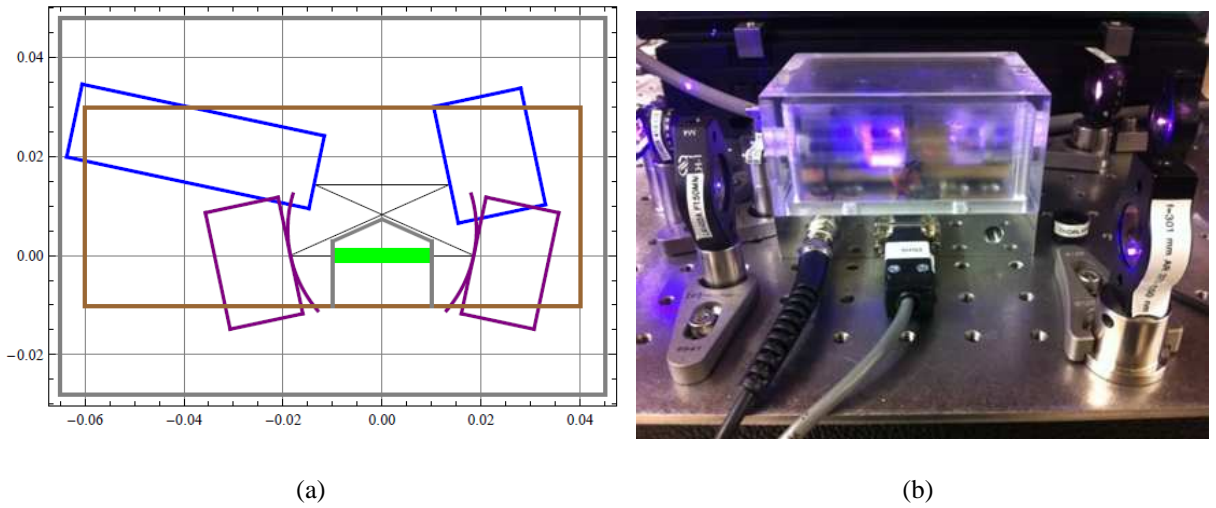


Figure 3.7 (a) cavity arrangement with unit in m (b) PPKTP cavity assembly with blue light output

The main issue of this PPKTP SHG cavity is that the output blue power degrades over time. The typical performance of it is with about 600 mW of input fundamental light, the output blue light starts at about 45 mW. And the power degrades down to about 20 mW in \sim two hours and then stays there. This is due to the thermal effect caused by the tight focusing used ($w_0 = 23\mu\text{m}$), corresponding to the theoretical optimum of the single-pass efficiency for the PPKTP crystal length of 20 mm. [28, 30]. PPKTP crystal absorbs short wavelength light around 400 nm, and turns it into heat, leading to the change of the index of refraction of the crystal. Therefore the effective cavity length is changed over time. The corresponding thermal lensing power is proportional to w_o^2 . [31]. Because of this the mode-matching becomes worse and the conversion efficiency got reduced. Furthermore, the two polarization modes inside the cavity move relatively when the temperature is changed, and leads to a phase change of the error signal. This makes locking the cavity difficult.

To circumvent this thermal effect, we have chosen to use a weaker focus (smaller spot size of the IR beam) in the crystal with a bigger cavity design. The new design loosens up the crystal focus waist by about a factor of two, so the the thermal lens power is 4 times less than at the optimal focusing [32].

The total round trip length of this cavity is 22 cm, with the incident angle of 10° . The curved mirrors have radius of curvature of 50 mm instead of 25 mm. The curved mirror distance is chosen to be 6.7 cm from fig. 3.8, where the tangential and sagittal waists are overlapped. And this design corresponds to about $39 \mu\text{m}$ in both tangential and sagittal planes in the crystal, giving a single-pass efficiency of 0.4 %.

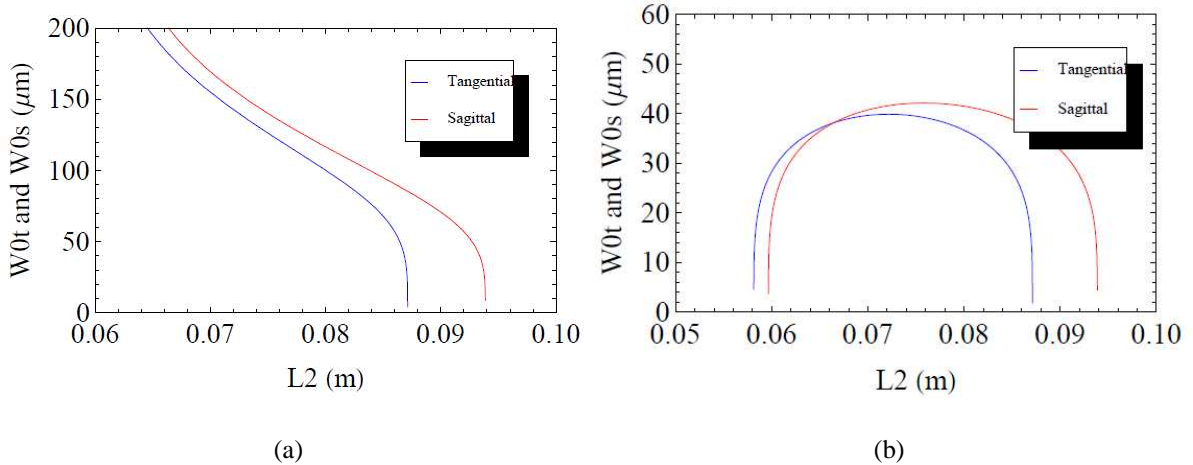


Figure 3.8 (a) waist size between flat mirrors (b) waist size between curved mirrors

Fig. 3.9 shows an estimation of the output power vs. input power at different input coupler transmission T , assuming a cavity loss of 3.5 %. And fig. 3.10 shows a to-scale layout of this big PPKTP cavity.

This bigger cavity design improved our PPKTP frequency doubling performance. The output power is typically ~ 70 to 80 mW at 410.5 nm out of ~ 700 mW pump beam at 821 nm. The power still degrades over time but with a slower rate. Normally it would drop to about 45 mW throughout the day and stabilize there.

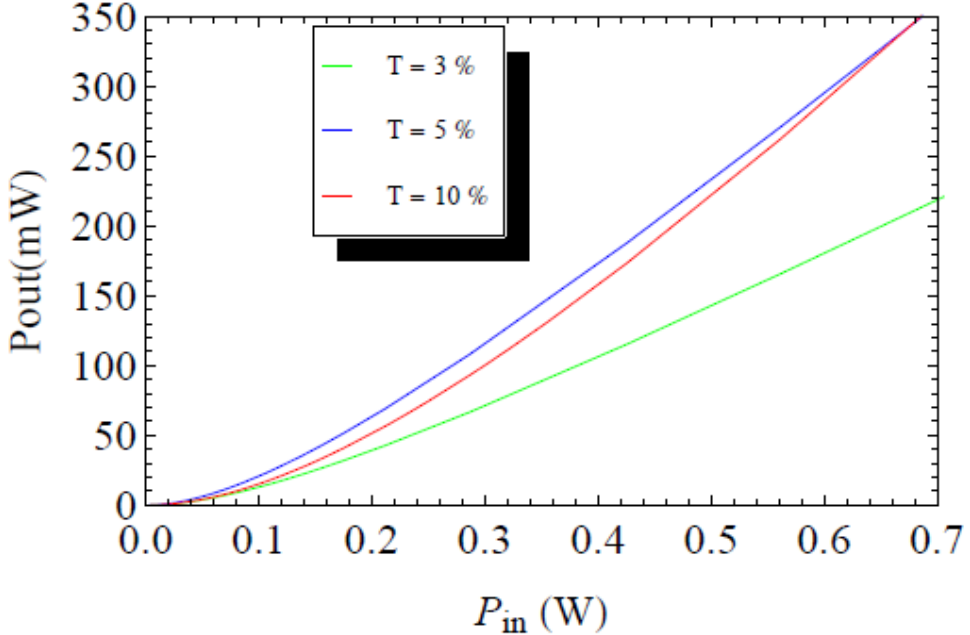


Figure 3.9 Estimated blue output power vs. red input power

3.4 Lithium Tri-Borate LiB_3O_5 (LBO) crystal SHG

LBO crystal is insensitive to blue light absorption. Therefore we do not need to worry about the thermal effect for LBO SHG cavities. Small cavity design with tight focusing inside the crystal is feasible. The index of refraction of LBO crystal at 821 nm is 1.61 [33]. The crystal front and back surfaces are antireflection-coated for 821 nm light at normal incidence. The advantages of using LBO crystal are large phase-matching angle, small walk-off angle, high damage threshold and little thermal effect. The disadvantage is that it has a relatively small nonlinear susceptibility and requires precise angle-matching.

3.4.0.2 Phase-matching angle

Unlike the periodically-poled KTP crystal, the LBO crystal requires critical phase-matching. The cutting angle of the crystal is $\theta = 90^\circ$, with φ_m to be determined for type I(ooe) phase-matching at 821 nm. The internal phase-matching angle φ_m is determined by using Sellmeier's

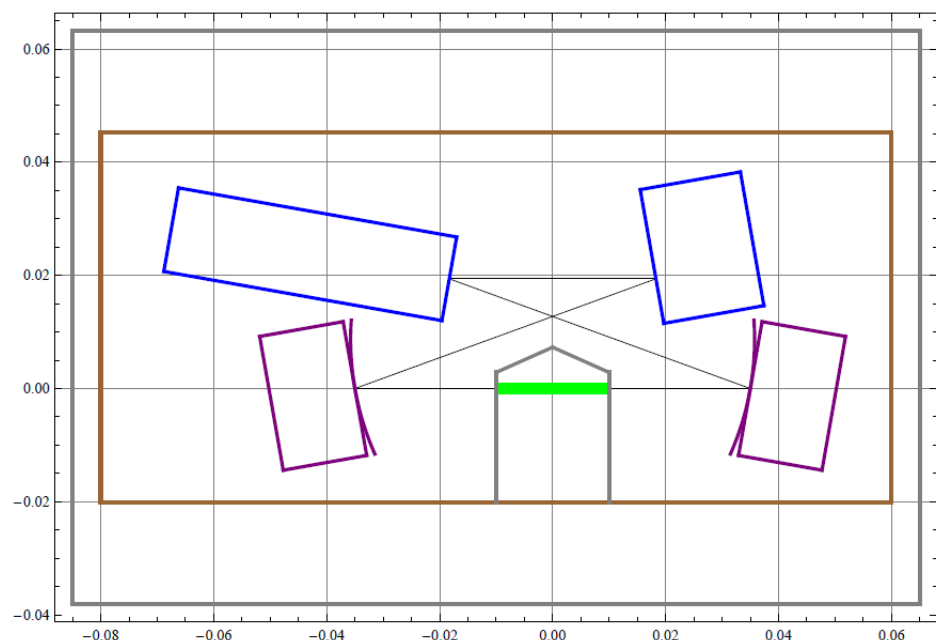


Figure 3.10 cavity arrangement with unit in m

equations(at 20 degree C) [27, 34, 35],

$$n_x^2 = 2.4542 + \frac{0.01125}{\lambda^2 - 0.01135} - 0.01388\lambda^2 \quad (3.8)$$

$$n_y^2 = 2.5390 + \frac{0.01277}{\lambda^2 - 0.01189} - 0.01848\lambda^2 \quad (3.9)$$

$$n_z^2 = 2.5865 + \frac{0.01310}{\lambda^2 - 0.01223} - 0.01861\lambda^2 \quad (3.10)$$

we can get the index of refraction along each axis for 821 nm and 410.5 nm light. Then using

$$\varphi_m = \arcsin\left(\sqrt{\frac{n_{z1}^{-2} - n_{y2}^{-2}}{n_{x2}^{-2} - n_{y2}^{-2}}}\right) \quad (3.11)$$

we can get the optimum phase-matching angle φ_m , which for our case is around 30° . To get an idea of how sensitive this angle is to temperature and wavelength, we can add the temperature dependence to the index of refraction n_{z1} in Sellmeier's equations:

$$n_z^2 = (2.5865 + \frac{0.01310}{\lambda^2 - 0.01223} - 0.01861\lambda^2)\sqrt{1 + (-6.3 + 2.1\lambda \times 10^{-6})(T - 20)} \quad (3.12)$$

Figure 3.11 below shows the phase-matching angle for LBO vs. wavelength at several temperatures.

3.4.1 Cavity setup

The single-pass and round trip conversion efficiency calculation method of LBO is very similar to PPKTP, with only a few difference in parameters: $d_{eff} = d_{32}Cos\varphi$, with $d_{32} = -0.98 \times 10^{-12}$, non-zero walk-off angle $\delta = 0.01$ rad, $B = 2.77$. The curved mirror have radius of curvature of 38 mm. The total round trip length is 18 mm. And the incident angle is 9° . Fig. 3.12 shows the waist sizes of the tangential plane and sagittal plane between the flat and curved mirrors. The curved mirror spacing of the cavity design is chosen to be 5.1 cm where the tangential and sagittal waists (both about $31 \mu m$) overlap.

Fig. 3.13 shows a to-scale layout of this LBO cavity and a top view picture of the cavity assembly.

Fig. 3.14 shows an estimation of the output power vs. input power at different input coupler transmission T, assuming a cavity loss of 3.5 %.

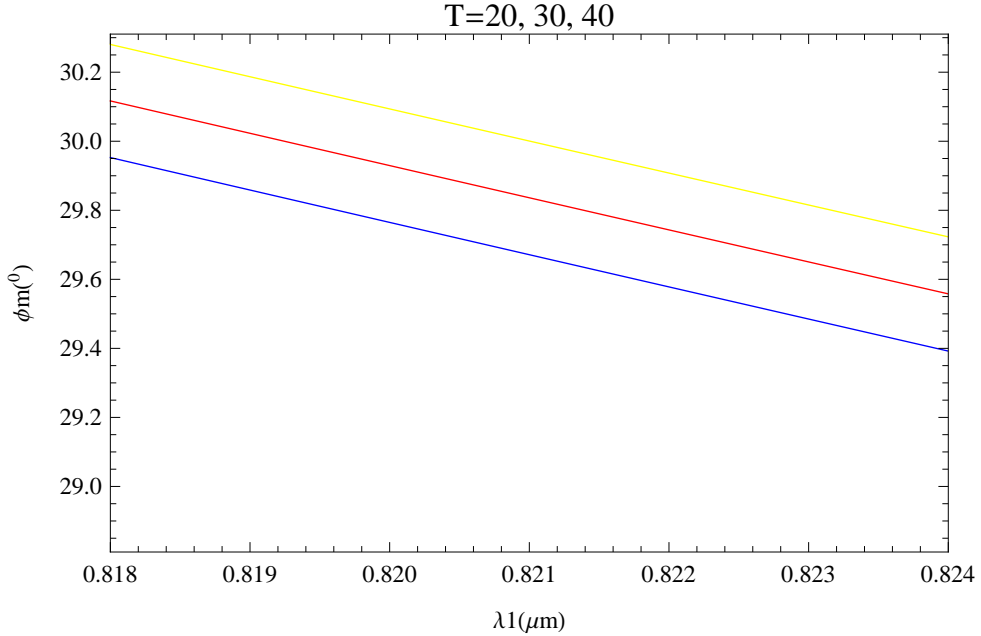


Figure 3.11 phase-matching angle for LBO vs. wavelength at 20° (blue), 30° (red), and 40° (yellow).

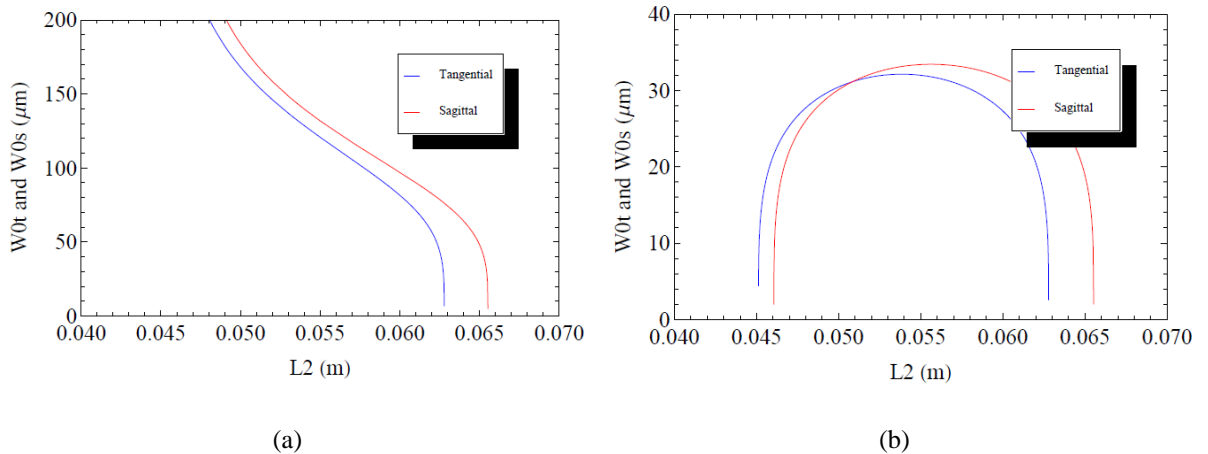


Figure 3.12 (a) waist size between flat mirrors (b) waist size between curved mirrors

The conversion efficiency result of the LBO cavity is as following: with input red light of about 500 mW, the maximum blue output power was about 9 mW. This red light was provided by the diode laser and the tapered amplifiers. For the Ti:Sa and LBO cavity setup, we achieved a better

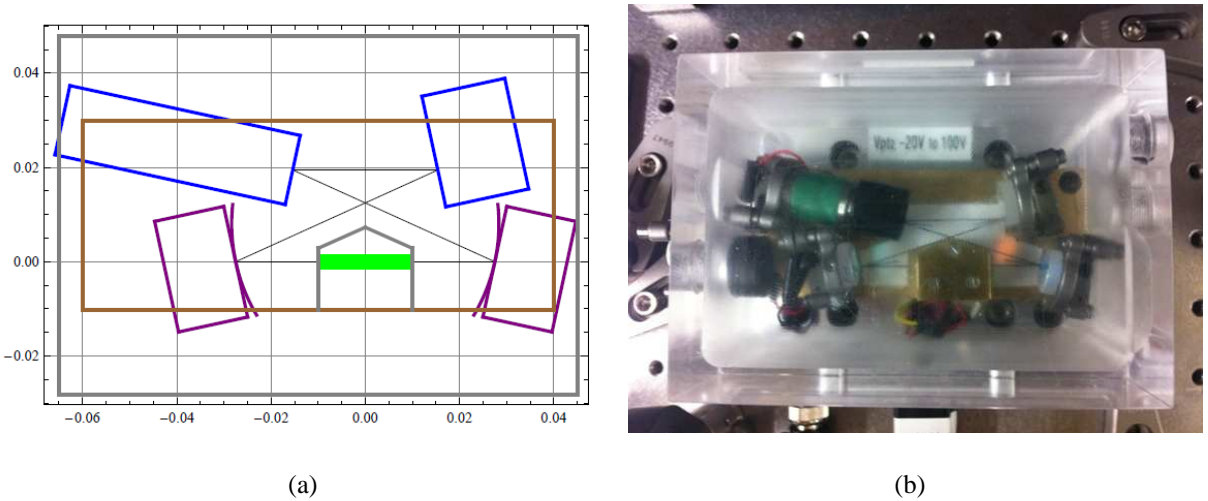


Figure 3.13 (a) cavity arrangement with unit in m (b) LBO cavity assembly (top view)

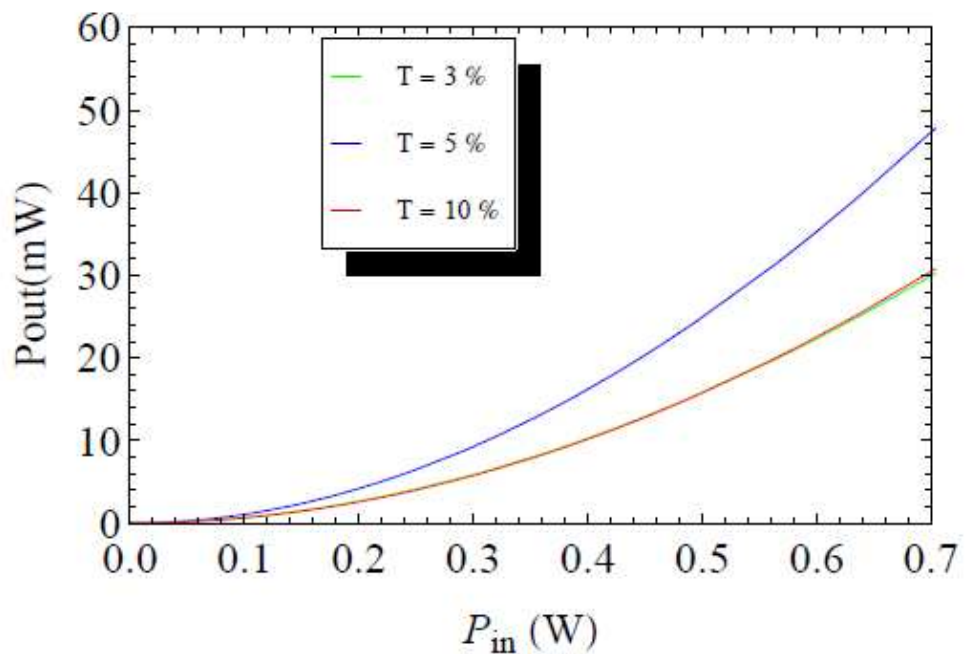


Figure 3.14 Estimated blue output power vs. red input power

result of 340 mW blue light out of 4.6 mW red light. Fig. 3.15 shows a picture of this setup. And more details would be discussed in next section.

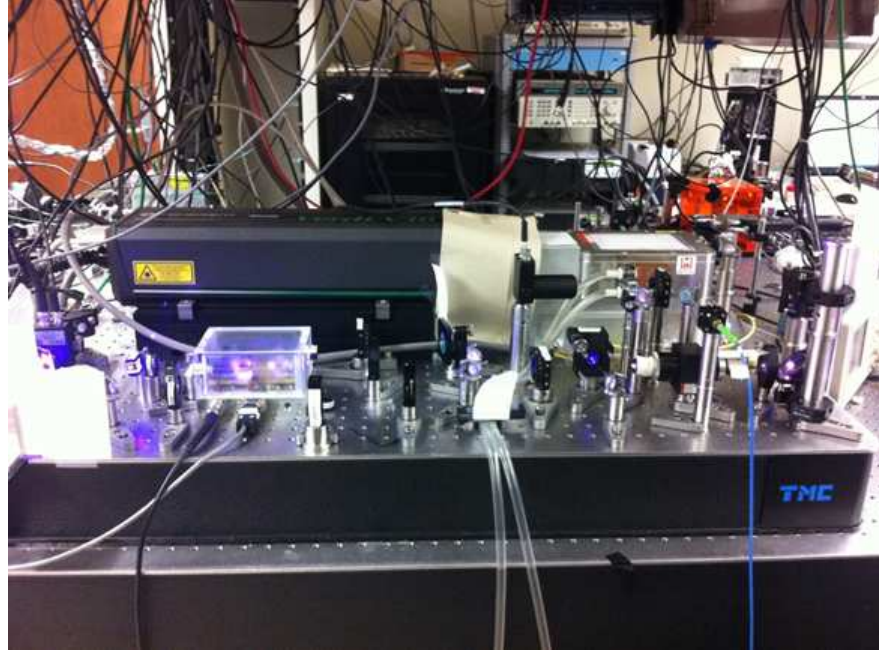


Figure 3.15 Laser setup with Ti:Sa laser and home-made LBO cavity

3.4.2 Mode-matching/impedance-matching measurement

In order to get high power output of frequency doubled light, it is critical to have good overlap between the fundamental beam and the cavity mode. The enhancement of power in a ring SHG cavity depends on the transmission of the input coupling mirror and the total losses inside the cavity. These losses are mainly caused by transmissions through three highly reflected mirrors, the crystal absorption, and the conversion into the second harmonic power. The cavity is said to be mode-matched when the transmission through the input coupling mirror equals to the total loss. We estimated that the total intra-cavity loss is about 1~2%, so M1 is custom made with the coating of $\geq 99\%$ at 821 nm.

The observed reflected intensity I_r at resonance is given by

$$\frac{I_r}{I_{in}} = m \frac{1}{R_{in}} \times \frac{(R_{in} - |g|)^2}{(1 - |g|)^2} + (1 - m)R_{in} \quad (3.13)$$

Where the coefficient $m = I_0/I_{in}$ is the fraction of the intensity that is mode matched to the cavity. Introduce a cavity loss coefficient g , which accounts for the coupling and internal losses, is written as $|g| = \sqrt{R_{in}R_{out}R_{cav}} = \sqrt{R_{in}(1 - L)}$.

To measure m, we need to do three measurements: First determine R_{in} by measuring the input coupler reflectivity with the intra-cavity field blocked(note that we need to measure the transmission T instead of R for HR mirrors and also take into account the reflection of the uncoated side of the mirror r and get $R_{in} = 1 - T + r$). Then measure the cavity finesse \mathcal{F} which determines g by $\mathcal{F} = \frac{\pi\sqrt{|g|}}{1-|g|}$. Then measure the reflection dip percentage η , which gives $(1 - \frac{I_r}{I_{in}})$, when the laser frequency is at cavity resonance frequency. For measuring cavity finesse, it should be measured when the least amount of blue is generated because in the term g, the conversion into blue power is not included. We can either tune the IR laser out of resonance frequency or change the cavity temperature at resonance frequency to minimize the loss by generating blue power. Once the three measurements are taken, the m can be calculated.

The calculated single-pass efficiency E_{NL} for LBO is 1.4×10^{-4} , i.e. with $P_{in}=600$ mW, $\epsilon=25\%$, and $P_{out}=150$ mW. The measured single-pass efficiency E_{NL} is 7.8×10^{-6} , i.e. with $P_{in}=600$ mW, $\epsilon=2.7\%$, and $P_{out}=16$ mW.

The previous attempts to get frequency doubled blue light using LBO crystals from a shape-corrected tapered amplifier output ended up disappointing. An example of what we got is as following: With Input 821nm power $P_{in} = 508mW$, measured reflected $P_{out} = 420mW$. Cavity finesse is measured to be 210, and reflection dip percentage 33%. With the numbers above, together with measured R_{in} , using equations (3.12), the calculated mode-matching coefficient m is about 50%. And under this condition, the actual 410nm power out of the cavity is about 9 mW. This is comparable our theoretical prediction.

Then we used the same SHG ring cavity with a Ti:Sapphire laser output and got a much better result. The main advantages of using a Ti:Sapph laser is its high power output and good beam mode. We used a Ti:Sapphire laser(Model: SolsTis) from M Squared which is capable of providing up to 5.4 W of single mode output at 821 nm with 18 W of Verdi laser pump power at 532 nm. The Ti:Sapphire laser has a line of $\sim 1\text{MHz}$ measured with Toptica FPI100 cavity. Our LBO ring cavity has a line width of 5.4 MHz. We installed a Faraday isolator between the Ti:Sapph laser and the SHG cavity to minimize the backward scattered light from the SHG cavity that perturbs the laser in spite of the unidirectional configuration of the SHG cavity [36]. Our Faraday isolator(at

850 nm) induces $\sim 25\%$ transmission loss. The cavity finesse is 310 and the intra-cavity loss is about 1.4%. The mode-matching coefficient is 77.4%. For an Incident fundamental power at 821 nm of 4.6 W, we obtained 340 mW of 410.5 nm light.

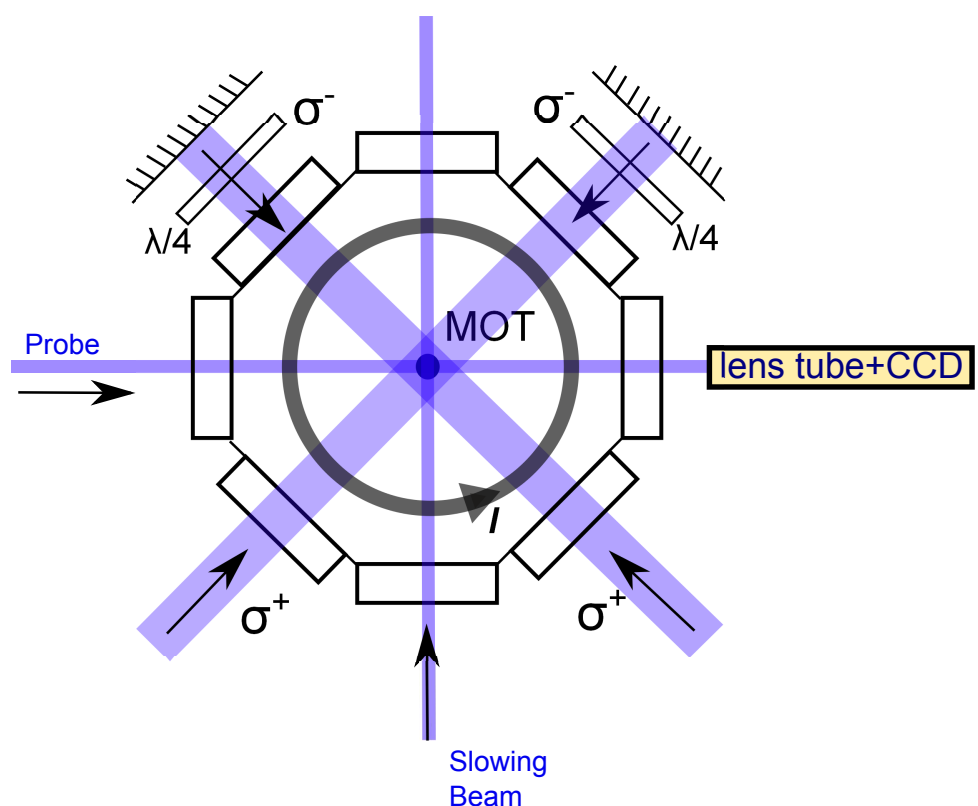
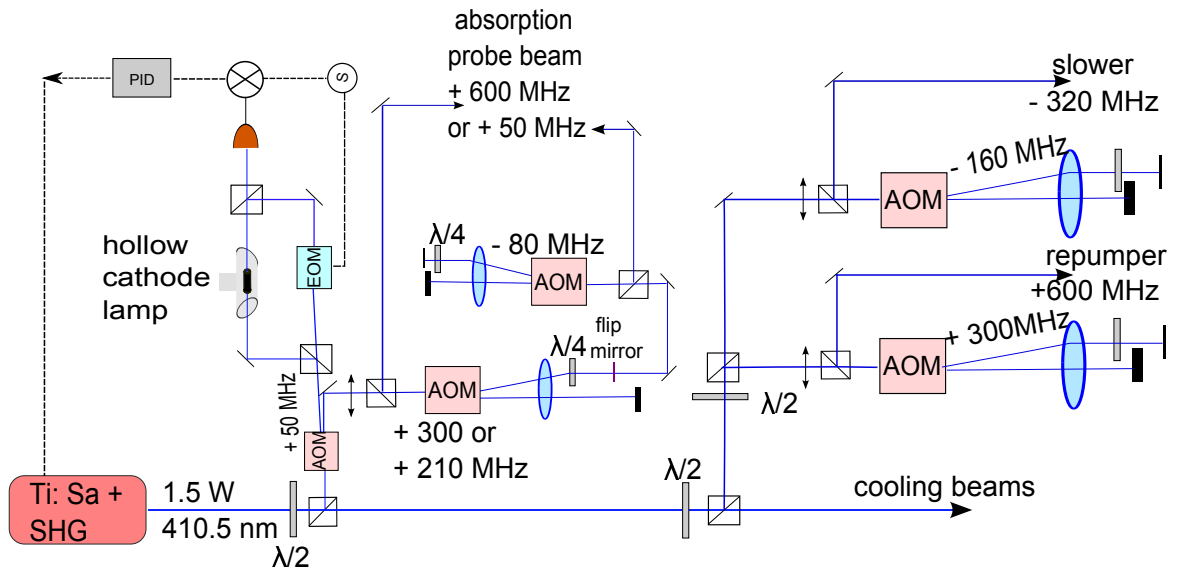
3.4.3 Setup with M2 lasers

In the experiment now we use a commercial M Squared Ti:Sapphire laser system with a Sprout pump laser of 16 W at 532 nm, a SolsTis Ti:Sapph laser outputting $\sim 4.8W$ of IR light at 821 nm, a high finesse reference cavity for frequency stabilization, and a SHG doubling cavity outputting $\sim 1.5W$ of blue light at 410.5 nm. The scan range of this laser is ~ 25 GHz, which is sufficient to cover all Ho transitions. The frequency of the laser is locked to a hollow cathode holmium lamp using modulation transfer technique. In fig. 3.16 a complete schematic of the optical setup is shown. And fig. 3.17 shows the beams layout at the MOT chamber.

In table 3.2, a summery of the light frequencies and the lasers providing them is shown. Various detunings for different purposes were achieved with AOMs, either single-pass or double-pass configuration. The use of double pass configuration compensates the beam shift of the first-order diffracted beam which is dependent on the modulation frequency of the AOM. A telescope pair around the AOM focuses the beam into the AOM. After the AOM, the higher order diffraction beams are blocked. The quarter wave plate causes the second pass of the AOM to be orthogonally-linearly polarized with respect to the first pass. So it goes out without overlapping with the incident beam.

Table 3.2 Ho laser system table

Purpose	Provided by	detuning(MHz)	power(mW)
MOT cooling	M2 system	$\sim - 50$	$200 \sim 300$
MOT repumping	M2 system	$\sim + 600$	~ 10
Atom slowing	M2 system	- 320	~ 70
Absorption imaging probe	M2 system	$\sim + 50$ and $\sim + 600$	$\sim 10^{-3}$



3.5 Summary

In summary, this chapter covers a brief history of the laser systems built. Details about designing and constructing frequency doubling cavities with PPKTP and LBO crystals are discussed. And our most recent laser system with M2 lasers and optical setup for the MOT operation is shown.

Chapter 4

Spectroscopy

4.1 Hyperfine structure

We follow the treatment in [37], the relativistic hyperfine Hamiltonian of an atom is given by

$$H_{hypf} = \sum_k \mathbf{M}^{\{k\}} \cdot \mathbf{T}^{\{k\}} \quad (4.1)$$

where $\mathbf{M}^{\{k\}}$ and $\mathbf{T}^{\{k\}}$ are spherical tensors of rank k , representing the nuclear and electronic parts of the interaction, respectively. In first-order perturbation theory, the eigen-states of the Hamiltonian are $|J, I, F, m_F\rangle$ states. Where F is the quantum number of the total angular momentum $\mathbf{F} = \mathbf{I} + \mathbf{J}$, with \mathbf{I} and \mathbf{J} being the total angular momentum of the nucleus and the electron state, respectively. The I is always a good quantum number of H , as very large energies are involved in the transitions between nuclear states. J is also a good quantum number in the first-order approximation.

The eigenenergies, i.e. the hyperfine energies $E(J)$ of the $|J, M_J\rangle$ states are

$$\begin{aligned} E(J) &= \left\langle I, J, F, M_F \left| \sum_k \mathbf{M}^{\{k\}} \cdot \mathbf{T}^{\{k\}} \right| I, J, F, M_F \right\rangle \\ &= \sum_k (-1)^{I+J+F} \left\{ \begin{array}{ccc} I & J & F \\ J & I & k \end{array} \right\} \times \langle I \left| \mathbf{M}^{\{k\}} \right| I \rangle \times \langle J \left| \mathbf{T}^{\{k\}} \right| J \rangle \end{aligned} \quad (4.2)$$

In the magnetic dipole case, $k=1$. The magnetic dipole hyperfine constant A is defined by

$$A = \mu_N \frac{\mu_I}{I} \frac{\langle J \left| \mathbf{T}^{\{1\}} \right| J \rangle}{\sqrt{J(J+1)(2J+1)}} \quad (4.3)$$

where the nuclear dipole moment μ_I , in units of the nuclear magneton $\mu_N = e\hbar/2m_p c$, is defined as

$$\mu_N \mu_I = \left\langle I, I \left| \mathbf{M}_0^{\{1\}} \right| I, I \right\rangle = \begin{pmatrix} I & 1 & I \\ -I & 0 & I \end{pmatrix} \left\langle I \left\| \mathbf{M}^{\{1\}} \right\| I \right\rangle, \quad (4.4)$$

the magnetic dipole hyperfine energy E_{M1} is then given by

$$E_{M1} = A \mathbf{I} \cdot \mathbf{J} \quad (4.5)$$

In the electric quadrupole case, $k=2$. The electric quadrupole hyperfine constant is defined by

$$B = 2eQ \left(\frac{2J(J-1)}{(2J+1)(2J+2)(2J+3)} \right)^{\frac{1}{2}} \left\langle J \left\| \mathbf{T}^{\{2\}} \right\| J \right\rangle \quad (4.6)$$

where the nuclear quadrupole moment Q is defined as

$$\frac{eQ}{2} = \left\langle I, I \left| \mathbf{M}_0^{\{2\}} \right| I, I \right\rangle = \begin{Bmatrix} I & 2 & I \\ -I & 0 & I \end{Bmatrix} \left\langle I \left\| \mathbf{M}_0^{\{2\}} \right\| I \right\rangle, \quad (4.7)$$

the electric quadrupole hyperfine energy E_{d2} is then given by

$$E_{E2} = B \frac{\frac{3}{2}\mathbf{I} \cdot \mathbf{J}(2\mathbf{I} \cdot \mathbf{J} + 1) - \mathbf{I}^2 \mathbf{J}^2}{2I(2I-1)J(2J-1)} \quad (4.8)$$

Then the zero-field (at zero magnetic field) Hamiltonian, after first-order approximation, can be written as

$$H = E_{M1} + E_{E2} = \mathbf{I} \cdot \mathbf{J} + B \frac{\frac{3}{2}\mathbf{I} \cdot \mathbf{J}(2\mathbf{I} \cdot \mathbf{J} + 1) - \mathbf{I}^2 \mathbf{J}^2}{2I(2I-1)J(2J-1)} \quad (4.9)$$

Using the identity of $\mathbf{I} \cdot \mathbf{J} = \frac{1}{2}(\mathbf{F}^2 - \mathbf{I}^2 - \mathbf{J}^2)$, the eigen-energies can be found to be

$$E = \frac{1}{2}AK + B \frac{3K(K+1) - 4I(I+1)J(J+1)}{8I(2I-1)J(2J-1)} \quad (4.10)$$

where $K = F(F+1) - J(J+1) - I(I+1)$.

4.2 Ho 410 nm optical transitions between ground and excited states

Ho has one stable isotope ^{165}Ho , which has nuclear spin $I = \frac{7}{2}$. For the 410.5 nm transition, the ground state, which has $J_g = \frac{15}{2}$, is shifted into 8 levels, with $F = 4 \sim 11$. The excited state, which has $J_e = \frac{17}{2}$, is shifted into 8 levels, with $F = 5 \sim 12$.

Table 4.2 calculated from electric dipole matrix elements shows the relative transition strengths of the 21 transitions. The transition strength is defined as electric dipole matrix element representing the coherence coupling between the hyperfine states. For example in holmium, the transition strength between ground state $|F_1, m_{f1}\rangle$ and excited state $|F_2, m_{f2}\rangle$ is given by

$$\begin{aligned}
 d_{21} &= \langle F_2, m_{f2} | d | F_1, m_{f1} \rangle \\
 &= (-1)^{F_2 - m_{f2}} \begin{pmatrix} F_2 & 1 & F_1 \\ -m_{f2} & q & m_{f1} \end{pmatrix} (-1)^{1+I+J_2+F_1} \sqrt{(2F_1+1)(2F_2+1)} \cdot \begin{Bmatrix} J_2 & F_2 & I \\ F_1 & J_1 & 1 \end{Bmatrix} \\
 &\quad \cdot (-1)^{\frac{5}{2}+L_2+J_1} \sqrt{(2J_1+1)(2J_2+1)} \begin{Bmatrix} L_2 & J_2 & \frac{3}{2} \\ J_1 & L_1 & 1 \end{Bmatrix} \cdot (-1)^{L_2+\frac{1}{2}(1+L_1+L_2)} \sqrt{\text{Max}(L_1, L_2)}
 \end{aligned} \tag{4.10}$$

And Table 4.3 shows the hyperfine shifts for ground and excited states, calculated with hyperfine constants for ground and excited states as following: $A = 800.583645$ MHz, $B = -1668.00527$ MHz, $A' = 653 \pm 2$ MHz, $B' = -500 \pm 200$ MHz [38]. Table 4.1 shows a collection of reference with the ground and excited state hyperfine constants of holmium 410.5 nm transition.

Table 4.1 hyperfine constants in references

Ground State				Excited State		Reference
$A(\text{Exp.})$	$B(\text{Exp.})$	$A(\text{Theo.})$	$B(\text{Theo.})$	$A'(\text{Exp.})$	$B'(\text{Exp.})$	
800.583645(6)*	-1668.00527(33)*					W. Dankwort, et al [39]
800.583645	-1668.00527			653±2	-500±200	C. I. Hancox, Ph.D Thesis [38]
800.58309(6)	-1668.089(8)	800.581	-1668.987			B. Burghardt, et al [40]
800.5836434(4)	-1668.005336(32)					B. Burghardt, et al [40], Nachtsheim, G Thesis [41]
800.583 (+ 4.5%)	-1668.089 (- 2.8%)	836.77	-1621.87			K. T. Cheng and W. J. Childs [42]
800.583 ± 0.003	-1668.950 ± 0.050					Kurze Originalmitteilungen [43]

Note, *have been corrected for second order hyperfine interaction within the 4I ground multiplet.

The corrected constants are 800.583173(36) and -1668.07870(330).

Table 4.2 transition strengths of 410 nm transitions

$F \rightarrow F - 1$		$F \rightarrow F$		$F \rightarrow F + 1$	
				$4 \rightarrow 5'$	1.58
		$5 \rightarrow 5'$	0.13	$5 \rightarrow 6'$	1.79
$6 \rightarrow 5'$	0.004	$6 \rightarrow 6'$	0.22	$6 \rightarrow 7'$	2.05
$7 \rightarrow 6'$	0.007	$7 \rightarrow 7'$	0.28	$7 \rightarrow 8'$	2.34
$8 \rightarrow 7'$	0.009	$8 \rightarrow 8'$	0.29	$8 \rightarrow 9'$	2.67
$9 \rightarrow 8'$	0.008	$9 \rightarrow 9'$	0.28	$9 \rightarrow 10'$	3.04
$10 \rightarrow 9'$	0.005	$10 \rightarrow 10$	0.23	$10 \rightarrow 11'$	3.44
$11 \rightarrow 10'$	0.002	$11 \rightarrow 11'$	0.13	$11 \rightarrow 12'$	3.89

Table 4.3 hyperfine shifts of ground and excited states of Ho

F	Ground states	HPF shift (GHz)		
		Excited states		
4	-24.425	$A' = 653, B' = -500$	$A' = 655, B' = -700$	$A' = 651, B' = -300$
5	-20.1157	-21.8869	-22.0232	-21.7505
6	-15.0195	-17.8743	-17.9609	-17.7878
7	-9.17708	-13.2169	-13.2549	-13.179
8	-2.63625	-7.92572	-7.92081	-7.93063
9	4.54858	-2.01327	-1.97618	-2.05036
10	12.3161	4.50623	4.55912	4.45334
11	20.5983	11.617	11.663	11.571
12		19.3018	19.3113	19.2923

Since the electric dipole transitions follow the the selection rules: $\Delta F = 0, \pm 1, F + F' \geq 1$, there are a total of 21 transitions lines, of $F = 4$ to $F' = 5$; $F = 5$ to $F' = 4, 5, 6; \dots$; $F = 11$ to $F' = 11, 12$. Table 4.4 shows the overall transition line shifts using the same sets of hyperfine constants as above.

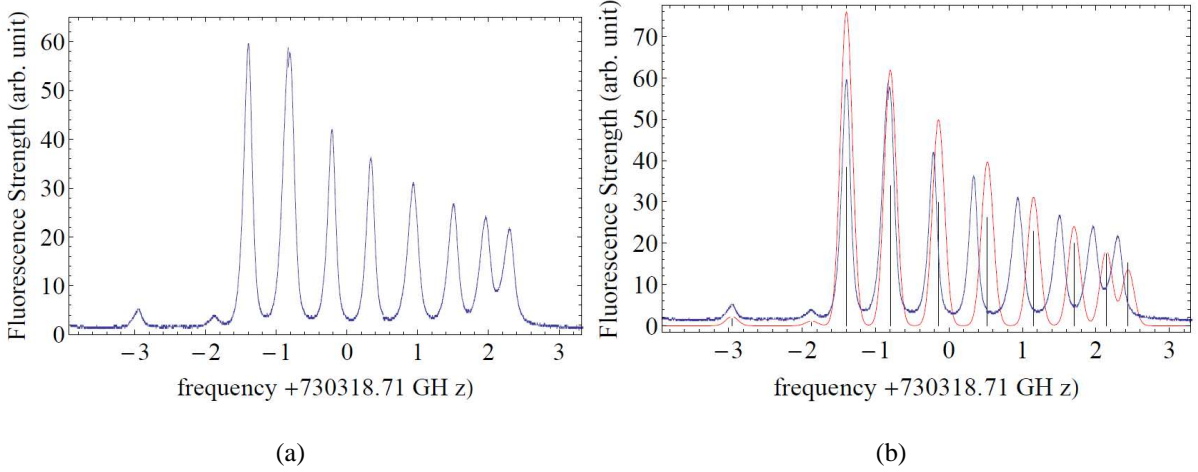


Figure 4.1 Ho zero-field hyperfine spectrum for the 410.5 nm transition. (a)experimental spectrum of 5 successive scans (b)fit to experiment curve with excited state A' and B' from Hancox. Note: the other 11 hyperfine peaks extending toward the lower frequency side are cut off in this spectrum.

Among the 21 transitions, there are 8 strongest ones, which are $F = 4$ to $F' = 5$, $F = 5$ to $F' = 6$ $F = 11$ to $F' = 12$ (shown in the third column of table 4.2).

The spectroscopy was first taken with our early version of vacuum system with a home-made holmium source, and the early version laser system including the 821 nm ECDL, tapered amplifiers and home-made SHG cavities. The schematic layout of the vacuum system with optical paths is shown in fig. 4.2. Fluorescence spectroscopy was done in the second level chamber from the holmium source with double-passed beam configuration. And absorption spectroscopy was done in the first level chamber with a single-passed beam going right through the holmium source. Figure 4.1 shows the zero-field experimetal spectrum of the 8 strongest transitions, together with two weak ones extended to the red, for the $0 \text{ cm}^{-1} \rightarrow 24360.81 \text{ cm}^{-1}$ transition at 410.5 nm [44]. And a theoretical curve fit is also shown, which is generated with the same set of ground state hyperfine constants and excited state hyperfine constants of $A' = 653$ and $B' = -500$. Note that the fit curve is not very well matched with the experimental data mainly due to the multiple scanning of the experimental data which does not match quite well at each point of the adjacent scans. Our laser system back then could not stay locked with a frequency scan more than about

1GHz. And an overall absorption theoretical curve and experimental data (also taken with multiple frequency scans) are shown in fig. 4.3.

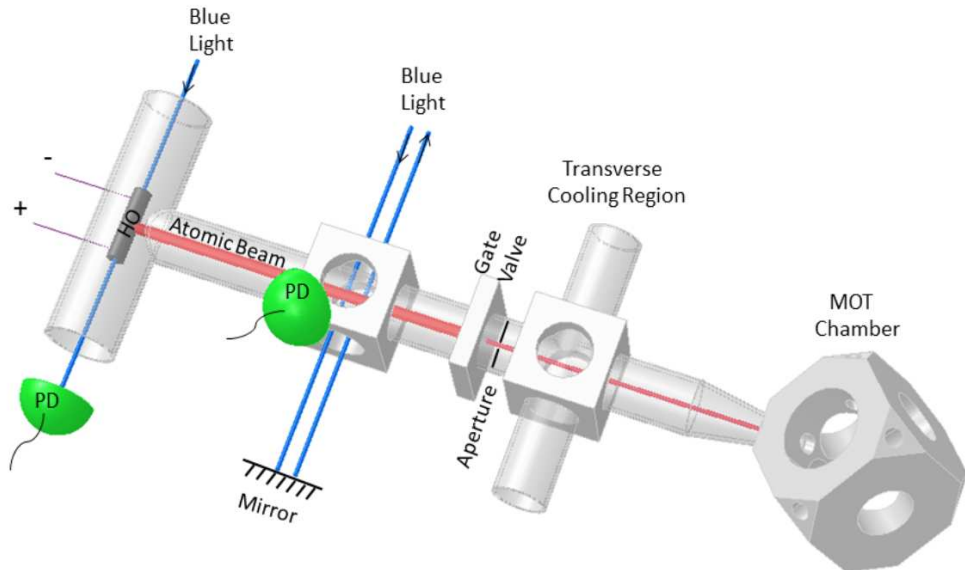


Figure 4.2 hyperfine spectroscopy setup

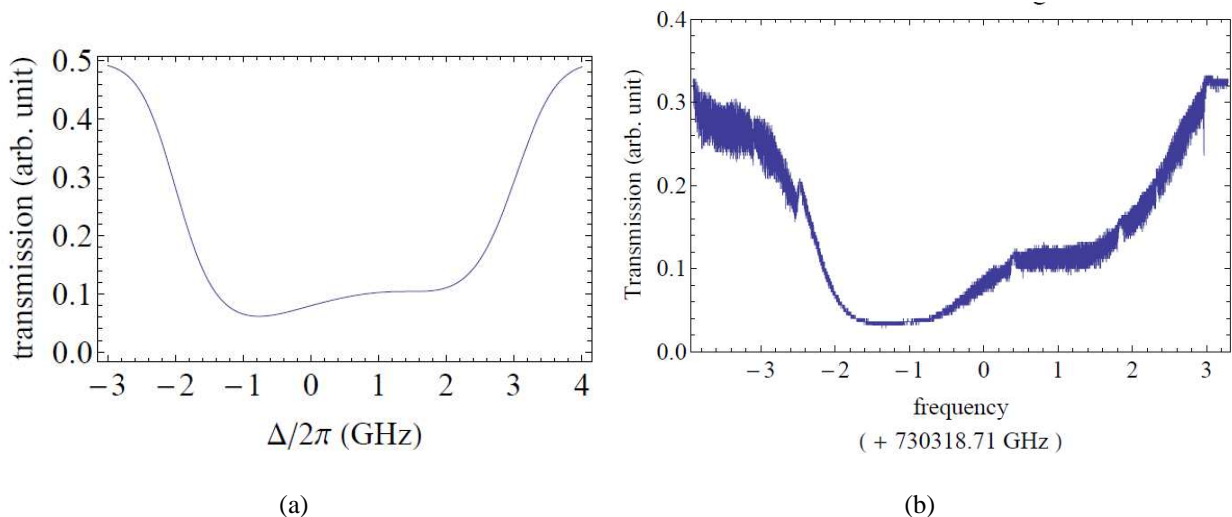


Figure 4.3 (a) theoretical overall absorption curve (b) experimental overall absorption curve

After installing the commercial M2 laser system, we were able to do a frequency scan wide enough to cover all 8 strong transitions at once. The spectroscopy data shown in fig. 4.5 was

Table 4.4 hyperfine shifts of 22 optical transition lines

		transition line shift (GHz)		
F	F'	$A' = 653, B' = -500$	$A' = 655, B' = -700$	$A' = 651, B' = -300$
4	5	2.53811	2.40176	2.67446
5	5	-1.77117	-1.90753	-1.63482
5	6	2.24136	2.15483	2.32790
6	5	-6.86743	-7.00378	6.73108
6	6	-2.85489	-2.94143	-2.76835
6	7	1.80251	1.76453	1.84049
7	6	-8.69726	-8.7838	-8.61073
7	7	-4.03987	-4.07784	-4.00189
7	8	1.25136	1.25627	1.24645
8	7	-10.5807	-10.6187	-10.5427
8	8	-5.28947	-5.28456	-5.29438
8	9	0.62298	0.660072	0.585887
9	8	-12.4743	-12.4694	-12.4792
9	9	-6.56185	-6.52476	-6.59894
9	10	-0.0423526	-0.0105381	-0.0952434
10	9	-14.3294	-14.2923	-14.3665
10	10	-7.8099	-7.75701	-7.86279
10	11	-0.699119	-0.653115	-0.745123
11	10	-16.0921	-16.0392	-16.1450
11	11	-8.98131	-8.9353	-9.02731
11	12	-1.29657	-1.28707	-1.30607

taken in the hollow-cathode Ho lamp. The modulation transfer technique was used to obtain the spectroscopy data [45, 46]. Fig. A.7 shows the schematic layout of the setup. The laser beam (a total power of about 15 mW) is split into two paths, a pump beam and a probe beam. The pump

beam is phase modulated with an EOM that is driven by a local oscillator. The probe beam that counter-propagates and overlaps with the pump beam is detected by a photodetector. The detected signal is demodulated by an rf mixer, giving an IF output of a background-free error signal. More details about this technique is discussed in Appendix A.

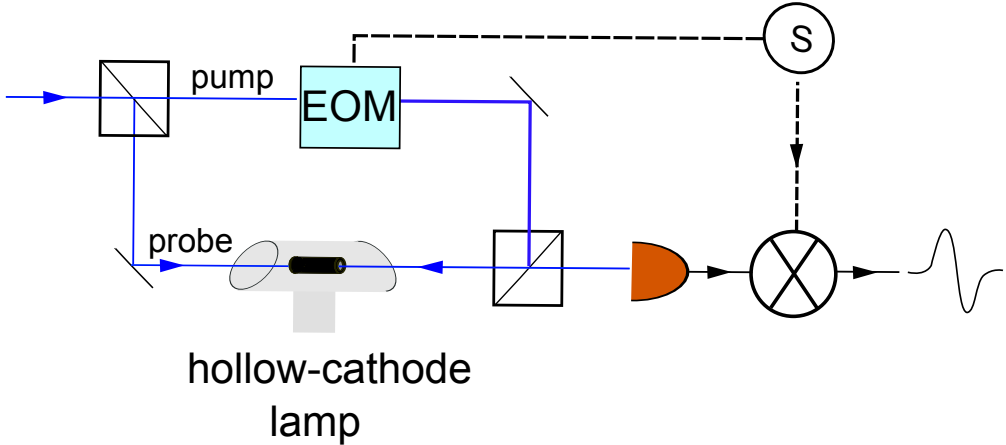


Figure 4.4 Modulation transfer spectroscopy setup

The spectroscopy data shows the error signals of each transition peak. The zero-crossing frequencies were picked out. Since the absolute frequency reading taken from the wavemeter has offset, only the frequency differences Δfs between transitions were taken for curve fitting with theory.

From the two measurements shown in fig. 4.5 and fig. 4.6, two sets of fit results for the excited state hyperfine constants A' and B' were obtained. The results and the Hancox's results [38] are shown in table. 4.5. The measurement including the eight strongest transitions of $F \rightarrow F + 1$, along with two weaker transitions of $F = 5 \rightarrow F' = 5$ and $F = 6 \rightarrow F' = 6$ gives $A' = 654$ and $B' = -538$. Another measurement including five of the $F \rightarrow F$ transitions from $F = 5 \rightarrow F' = 5$ to $F = 9 \rightarrow F' = 9$ along with two of the strong transitions of $F = 10 \rightarrow F' = 11$ and $F = 11 \rightarrow F' = 12$ gives $A' = 653$ and $B' = -575$. Both results verify the Hancox's result of $A' = 653 \pm 2$ and $B' = -500 \pm 200$. The A' and B' extracted from the curve fit to the spectroscopy data were used to calculate the transition frequency differences and marked back onto the spectroscopy data. The three kinds of frequency markers(Green: zero-crossing frequencies marked directly from

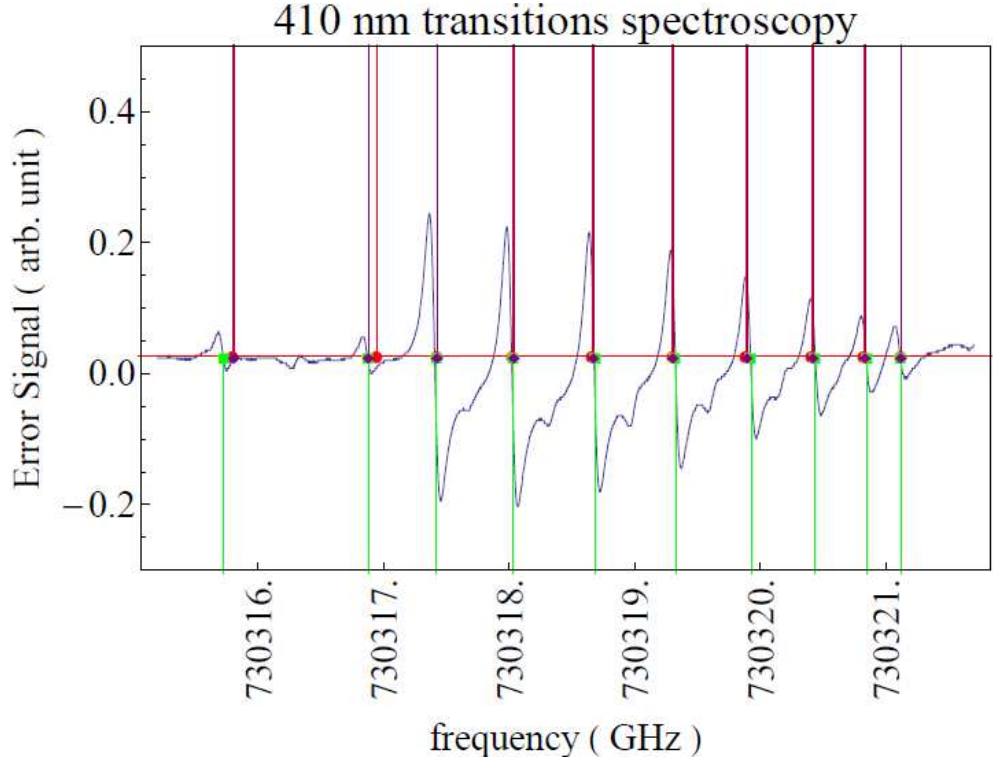


Figure 4.5 Spectroscopy of the frequency scan including 8 strong transitions of $F \rightarrow F + 1$ transitions, namely $F_g = 4 \rightarrow F_e = 5, \dots, F_g = 11 \rightarrow F_e = 12$, and 2 weak transitions of $F_g = 5 \rightarrow F_e = 5$ and $F_g = 6 \rightarrow F_e = 6$. Frequency markers are labeling transition frequencies derived with Hancox's hyperfine constants(red), measured experimentally(green), and derived with hyperfine constants fit to measurement(purple).

data; Red: marked with calculation from Hancox's A' and B' ; Purple: marked with calculation from fit A' and B' of this measurement) show reasonable consistency. The way that the tolerances were set in the Hancox's A' and B' is unknown. And for our measurements, the main sources of systematic errors are: the offsets of the zero-crossing frequencies of the error signals picked out from the experimental spectroscopy curve, and the offset of the total ramp frequency range($\sim \pm 20$ MHz). It is difficult to set a boundary of the influences from these error sources on the A' and B' results, so the tolerances are so far left open (no uncertainty boundary is added). But one thing to keep in mind is that the tolerance of the B' is supposed to be much bigger than A' , because the B' influences the energy shifts much less than A' does.

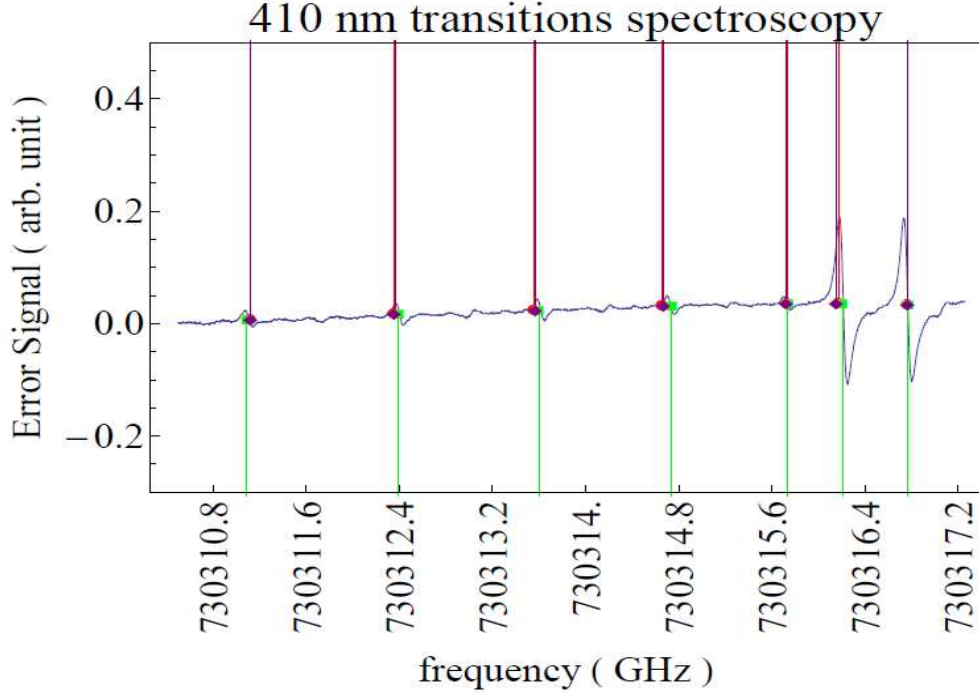


Figure 4.6 Spectroscopy of the frequency scan including 5 weak transitions of $F \rightarrow F$ transitions, including $F_g = 5 \rightarrow F_e = 5, \dots F_g = 9 \rightarrow F_e = 9$, and 2 strong transitions of $F_g = 10 \rightarrow F_e = 11$ and $F_g = 11 \rightarrow F_e = 12$. Frequency markers are labeling transition frequencies derived with Hancox's hyperfine constants(red), measured experimentally(green), and derived with hyperfine constants fit to measurement(purple).

Table 4.5 Results of excited state hyperfine constants

measurement	A'	B'
1 (mainly strong peaks)	654	-538
2 (mainly weak peaks)	653	-500
Hancox	653 ± 2	-500 ± 200

4.3 Ho 416 nm optical transitions between ground and excited states

Besides the cooling transition at 410.5 nm, another transition at 416 nm was also investigated. It has ground state $J = 15/2$ and excited state $J = 13/2$, with comparable linewidth of $106 \pm 5 MHz$. The wave number of this transition is $24014.22 cm^{-1}$ [47]. For this 416 nm transition, the ground state, which has $J_g = \frac{15}{2}$, is shifted into 8 levels, with $F = 4 \sim 11$. The excited state, which has

$J_e = \frac{13}{2}$, is also shifted into 8 levels, with $F = 3 \sim 10$. So there are in principle 21 hyperfine transitions.

Table 4.6 calculated from the electric dipole matrix elements shows the relative transition strengths of the 21 transitions.

Table 4.6 transition strengths of 416 nm transitions

$F \rightarrow F - 1$		$F \rightarrow F$		$F \rightarrow F + 1$	
$4 \rightarrow 3'$	1.23	$4 \rightarrow 4'$	0.15	$4 \rightarrow 5'$	0.006
$5 \rightarrow 4'$	1.43	$5 \rightarrow 5'$	0.25	$5 \rightarrow 6'$	0.011
$6 \rightarrow 5'$	1.68	$6 \rightarrow 6'$	0.31	$6 \rightarrow 7'$	0.013
$7 \rightarrow 6'$	1.97	$7 \rightarrow 7'$	0.33	$7 \rightarrow 8'$	0.011
$8 \rightarrow 7'$	2.30	$8 \rightarrow 8'$	0.31	$8 \rightarrow 9'$	0.007
$9 \rightarrow 8'$	2.67	$9 \rightarrow 9'$	0.25	$9 \rightarrow 10'$	0.003
$10 \rightarrow 9'$	3.08	$10 \rightarrow 10$	0.15		
$11 \rightarrow 10'$	3.54				

For the hyperfine shifts for ground and excited states, this case is different from the 410.5 nm one. Although it shares the same ground state as the 410 nm transition, with $A = 800.583645$ MHz, and $B = -1668.00527$ MHz, the excited state hyperfine constants A' and B' are not mentioned in any references. So we do not have a theoretical estimation of the energy shifts of the excited hyperfine states, thus the transition line frequency shifts.

From the transition strength listed in table 4.6, among the 21 transitions, there are 8 strongest ones, which are $F = 4$ to $F' = 3$, $F = 5$ to $F' = 4$ $F = 11$ to $F' = 10$. Figure 4.7 shows the zero-field experimental spectrum of the scan for these 8 strongest transitions. Note that only 7 transitions were observed, instead of 8, either from the error signals or from the saturated absorption curve. Since this 416 nm transition shares the same ground state with the 410 nm transition, in principle we can extract the excited state hyperfine constants A' and B' from the spectroscopy curve. But for this case it is unclear that the seven peaks that were resolved were which seven of the 8 strongest transitions, or if there were two transitions too close to each other

to be resolved as two. Fitting them to random 7 peaks of the 8 and solve for the excited state A' and B' gives a result of $A' \cong 860 \sim 900$, and $B \cong -1300 \sim -2400$.

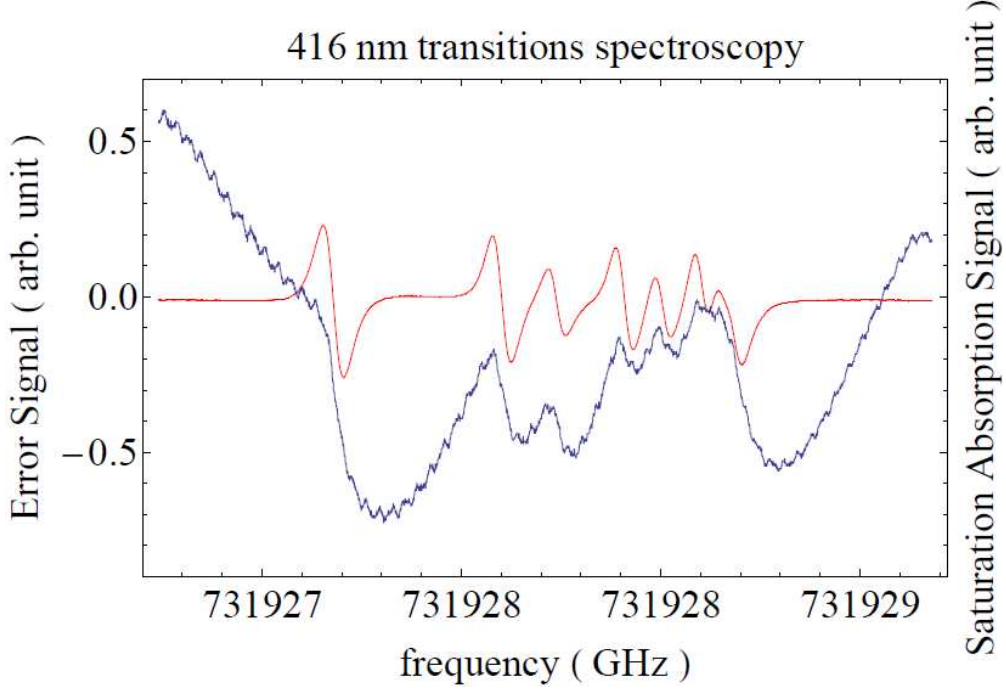


Figure 4.7 Spectroscopy of the frequency scan for the 8 strong transitions, taken on the hollow-cathode Ho lamp.

4.4 Summary

In summary, this chapter covers some background of hyperfine structure, hyperfine spectroscopy on the 410.5 nm transition of holmium, with two sets of experimental setups is discussed. The extracted hyperfine constants of the excited states are compared and discussed. Another set of hyperfine transitions at 416 nm with comparable linewidth is also investigated, and there is a missing transition left to be resolved.

Chapter 5

MOT characteristics

5.1 Overview

5.1.1 Laser cooling

The physics of laser cooling have been reviewed extensively in lots of literature [48, 49, 50, 51]. A famous analogy is: Suppose a bowling ball is flying in the air. A gun which is loaded with infinite number of ping-pong balls begins to fire at the bowling ball. Although the momentum of each ping-pong ball is very small compared with that of the bowling ball, the total momentum of all the ping-pong balls is enough to slow down and even stop the bowling ball. Then the bowling ball is replaced with an atom and the ping-pong ball gun with a laser loaded with photons. That is the basic idea behind laser cooling. Atoms in a laser beam experience a momentum kick of $\hbar k$, with the wave-vector k along the axis of beam propagation, every time they absorb a laser photon. When the photon is spontaneously emitted, the direction of the emission is random. The net change of momentum due to spontaneous emission is therefore zero, but the large number of photons in the laser beam reduces the atoms velocity in the k direction by $\sim \hbar k/m$ for every photon that is absorbed. After several thousands of absorption-emission cycles, the atom which typically has a velocity of several hundreds of meters per second, will be slowed down to just a few meters per second. Note that, for laser cooling to work the frequency of the light must be lower than ω_a , which is the resonance frequency of the atomic transition. This is due to the Doppler effect, the atom is not in resonance if the frequency ω is tuned to the resonance frequency ω_0 . In the atoms reference frame, an atom moving towards the laser beam will see a photon which appears to have a higher frequency (blue detuned) than it would if the relative atom-photon velocity were zero,

$\omega' = \omega + kv$. However, photons will be resonantly absorbed if the Doppler shift compensates the detuning, namely $\omega = \omega_0 - kv$. For red-detuned light, photons with wavevectors opposing the atoms direction of motion will be Doppler shifted onto resonance. These photons would therefore be absorbed. For each absorbed photon, the atom then acquires linear momentum by $\hbar k$, opposite to its initial momentum, leading to the atom being slowed down along the direction of the laser beam. Energy and momentum decreases simultaneously and the atom cools.

5.1.2 Magneto-optical trapping

The magneto-optical trap (MOT) is the most employed hybrid trap, combining optical fields and magnetic fields. It was first demonstrated by Chu et al. [52] in 1986 using Sodium atoms, and has become a standard research tool since then to capture atoms from a supplied background pressure. Up to date a large number of atoms have been laser cooled and trapped using magneto-optical traps(MOT). Since the first demonstration using sodium, various MOTs have been constructed with alkali atoms [53, 54, 55], and the alkaline earth atoms [56, 57], and the metastable states of the rare gases [58, 59, 60, 61]. These atoms have relatively simple energy level structures, so that cooling and trapping can be achieved with only a small number of lasers. And the wavelengths for the trapping transitions are all in the regime where tunable cw lasers with power of at least a few miliwatts are at hand. Rare earth atoms, on the other hand, have more complicated level structures, therefore were thought to be more difficult to be maneto-optically trapped. Until 1999, Yb was trapped by Honda et al. [62]. Followed with Er [13], Tm [15] and Dy [14].

The MOT combines three pairs of counter propagating laser beams and a magnetic field gradient. It is best understood by creating a one-dimensional model and then expanding to three dimensions. To understand how it works let's start with a simple model by considering a neutral atom as a two-level system and take the case of a plane wave incident on this atom. The process of resonant absorption by the atom is followed by an averaged symmetric spontaneous emission, after natural lifetime τ . That is to say for every absorbed photon the atom receives a momentum kick in the direction of the photon's motion. And momentum kicks from spontaneously emitted photons will be in random directions, so will cancel out. This results in the scattering of the incident light

momentum, and gives rise to an average scattering force in the direction of the incident light. This force acting on an atom is basically the product of the photon momentum and the rate at which the photons are absorbed. The scattering rate of photons from a two-level atom is given by [48]

$$\Gamma_s = \frac{\Gamma}{2} \frac{\Omega^2/2}{\Delta^2 + \Omega^2/2 + \Gamma^2/4} \quad (5.1)$$

where Γ is the natural decay rate, Ω is the Rabi frequency and Δ is the detuning from the resonance. The Rabi frequency can be related to the saturation intensity by $I/I_s = 2\Omega^2/\Gamma^2$, I is the intensity of the laser for one beam.

We could use the strong velocity dependence of the scattering force due to Doppler shift to damp or cool the atomic motion. In each dimension, with a pair of identical opposing beams tuned below resonance, any atomic motion along the axis meets a net opposing force due to the strong Doppler shifts of the absorption. Consider an atom placed between a pair of counter-propagating laser beams. If we assume that the laser intensity I is small compared to the saturation intensity I_s , the total force on the atom is given by the sum due to each laser beam

$$F_{net} = F_+ + F_- \quad (5.2)$$

where the force can be given by

$$F_{\pm} = \hbar k \frac{\Gamma}{2} \frac{I/I_s}{1 + 2I/I_s + 4(\Delta \mp kv)^2/\Gamma^2} \quad (5.3)$$

where Δ is the detuning from the transition. A detailed description of the derivation of this expression can be found in [48]. The contribution of these forces is shown in figure 5.1.

In order to capture the atoms in the MOT, the atoms have to be initially slow enough to interact and thermalize within a reasonable cooling volume. For atoms of a given injection velocity there is a "stopping distance z_s " of \sim twice the waist of the cooling beams.

We can now use the force in equation 5.3 and the stopping distance z_s to find particular velocity v_c an atom can be stopped from, which we call the capture velocity.

Begin with Newton's second law,

$$F = m \frac{dv}{dt} = mv \frac{dv}{dz} \quad (5.4)$$

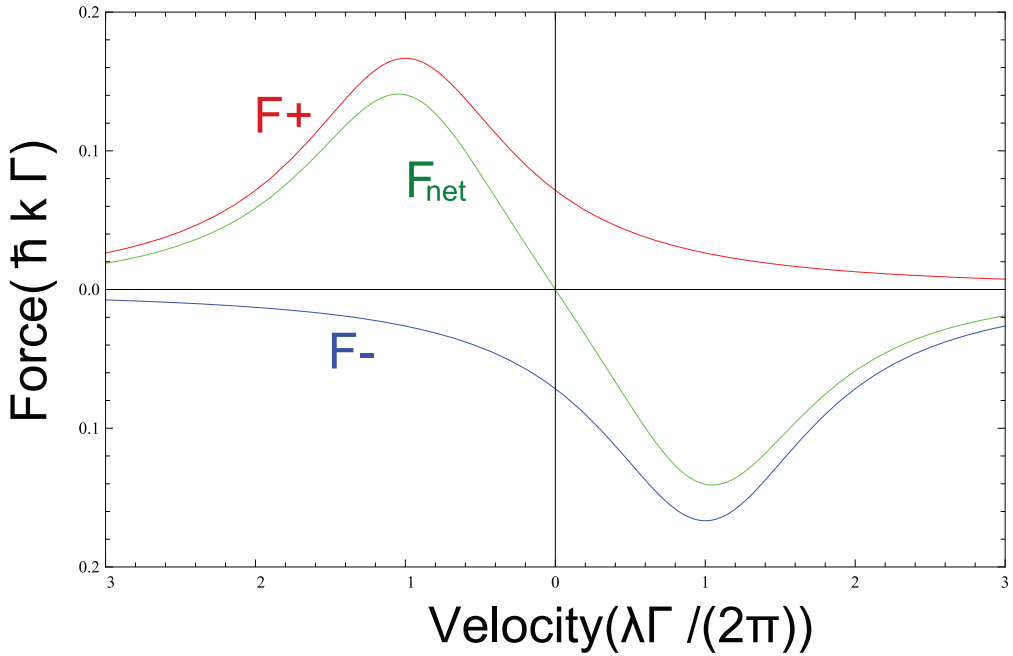


Figure 5.1 Scattering force as a function of velocity for two counter propagating laser beams with $I/I_s = 1, \Delta = -\gamma/2$.

and the scattering force $F(v)$ is a function of velocity.

$$mv \frac{dv}{dz} = F(v) \quad (5.5)$$

So we can integrate to find the stopping distance $z_s = 2w$

$$z_s = \int_0^{v_c} \frac{vdv}{F(v)} \quad (5.6)$$

Solving equation 5.6, we can find the capture velocity v_c for any set of trap parameters(Ho source temperature, detuning Δ , beam intensity I , etc.).

To cool atoms effectively using the Doppler effect, net cooling must be achieved for atoms in all directions. For this purpose, beams along all three Cartesian axes are needed. If the atom is exposed to three pairs of counter propagating laser beams it will slow down towards $v = 0$. This process is often called optical molasses. Although optical cooling decreases the volume of the atomic cloud in the velocity space, it does not confine them in position space. In addition, a central region must be provided where the cold atoms can accumulate. Atoms away from the trap center

should experience a net force driving them back to the origin. This is achieved by using circularly polarized light for the optical molasses and adding a spherical quadrupole magnetic field, such that as an atom moves away from the origin, the transition is Zeeman shifted into resonance with the beam which pushes it back. A pair of coils carrying opposing currents (near Anti-Helmholtz configuration) is normally used. This configuration gives rise to a magnetic field that increases linearly from the origin in each dimension.

Let us consider a simple model with ground state $J = 0$ and excited state $J = 1$. From the principle of conservation of angular momentum, the $\sigma+$ beam can only increase the internal quantum number m_F by one, i.e., it causes the transition between the Zeeman levels $m_F = 0$ and $m_F = +1$, and similarly, the $\sigma-$ beam causes the transition between the levels $m_F = 0$ and $m_F = -1$. This leads to a differential absorption that provides a restoring force on the atom. Thus the atoms will be trapped in a potential well, the barrier height of which depends on the magnetic field gradient.

The six circularly polarized beams passing through the MOT induce transitions with $\Delta m_F = \pm 1$. If the laser frequency ω_L is below the resonance frequency ω_0 , atoms in the region $z > 0$ absorb preferentially σ^- -light, which induces $\Delta m_F = -1$ transitions, while for $z < 0$ mainly σ^+ -light is absorbed. For $z = 0$ the absorption rates for σ^+ and σ^- light are equal. Since for $\omega < \omega_0$ atoms moving towards the laser beam propagation experience a larger average recoil than those moving into the direction of the beam propagation, this pushes all atoms moving outwards back towards the center. The gas of cold atoms is therefore compressed into a dense cloud around the center of the MOT.

Fig. 5.2 shows an example of a MOT in 1D. Extending this example to Holmium is straightforward. The ground ($J = 15/2$) and excited ($J = 17/2$) states of Ho are both split by the hyperfine interaction with the nucleus ($I=7/2$). The details of the energy structures of the Ho cooling transition will be discussed in Chapter 1.

One might assume that the atom gets cooled further and further till it reaches a velocity of zero and therefore zero temperature Kelvin. But the atom experiences heating from the spontaneously emitted photons in all directions. In fact the cooling achieves a minimum temperature at $I \ll I_s$

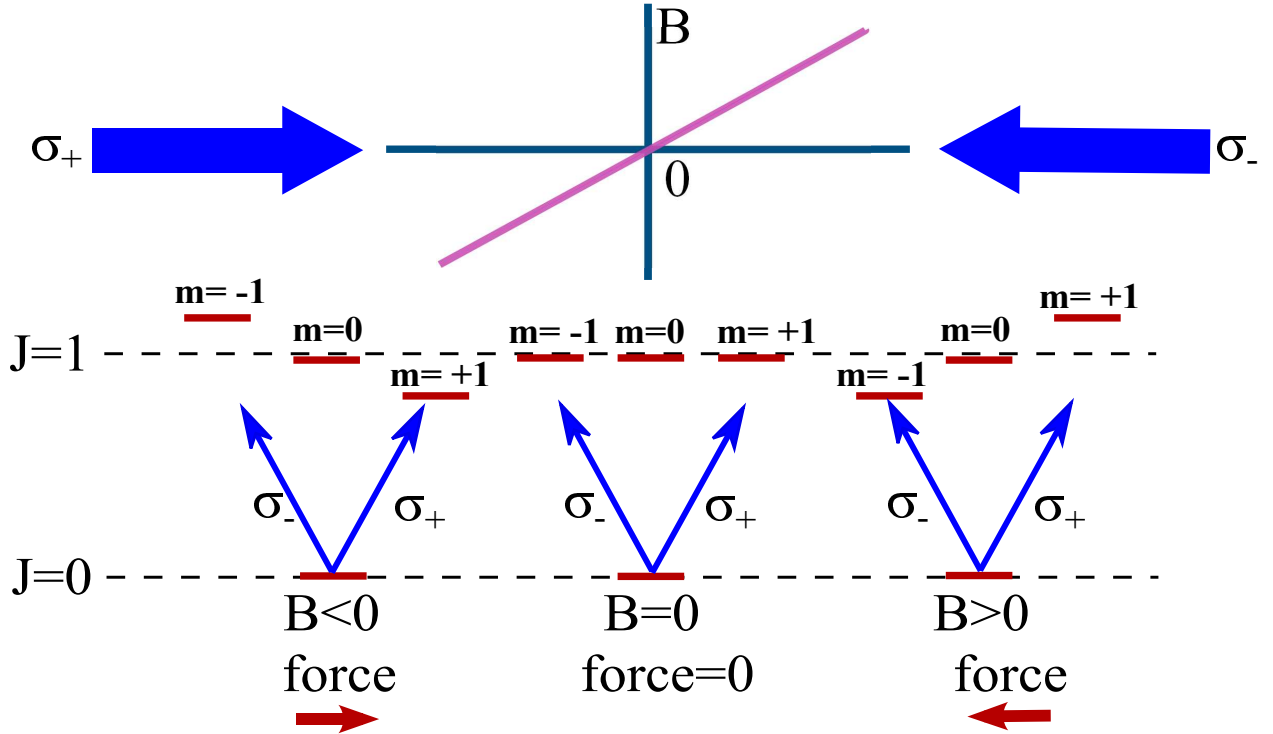


Figure 5.2 1D example of the MOT. Laser beams with opposite polarizations onto an atom from opposite directions. The lasers excite the $J=0$ to $J=1$ transition. The laser beam from the right only excites the $m = -1$ excited state, and the laser from the left only excites the $m = +1$ state. As the atom moves, these levels are shifted by the B field therefore affecting the respective photon scattering rates. The result is a position-dependent force that pushes the atoms into the center.

and $\Delta = -\gamma/2$ which can be expressed by

$$k_B T_D = \frac{\hbar \gamma}{2} \quad (5.7)$$

This is the Doppler cooling limit. For Ho at the $4f^{11}6S^2 \rightarrow 4f^{11}6S6P$, 410.5 nm transition this corresponds to a temperature of $T_D \approx 780 \mu K$.

5.2 Sub-Doppler cooling

It was soon discovered that temperatures way below this Doppler limit could be produced. Temperatures below the Doppler-cooling limit were observed; which is referred to as sub-Doppler cooling.

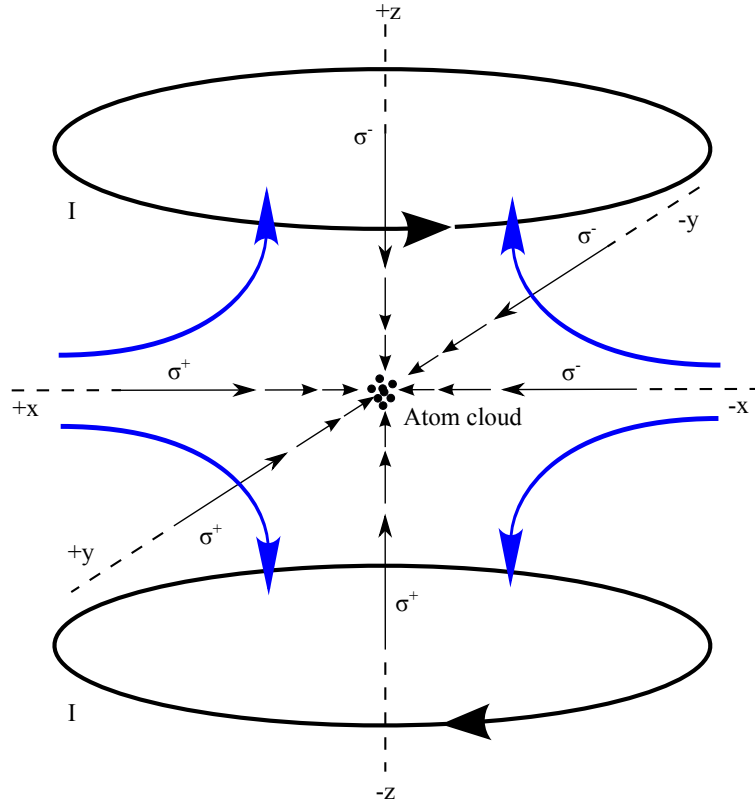


Figure 5.3 Principal arrangement of the MOT

This discrepancy between theory and experiment was explained by new cooling mechanisms [63, 64]. The heating due to spontaneous emission is inevitable, so the low temperatures had to be the result of some unexpectedly effective cooling mechanisms outside the Doppler model.

One key for the mechanism of sub-Doppler cooling to be possible is that the picture of the atom being a two level system is not realistic. In particular the presence of Zeeman levels in the hyperfine ground state has to be considered. The time it takes for optical pumping to transfer atoms among the magnetic sublevels is often longer than the lifetime of the excited state. Another key is that the counter-propagating laser beams cannot be treated independently, as their interference produces polarization gradients in the light field, which causes the optical pumping rate to be spatially dependent. The atom will experience a shift in the energy of its magnetic sublevels, which is dependent on the polarization of the laser field and the orientation of the atomic dipole. A

more detailed description can be found in [63]. Thus Sub-Doppler temperatures could be achieved using polarization gradients in the standing waves created by a pair of counter-propagating beams.

Two types of polarization gradient may occur, each linked with a different cooling mechanism:

For a pair of orthogonal linearly polarized beams(*lin* \perp *lin* polarization gradient cooling), the so called Sisyphus cooling occurs because of the spatial modulation in the light shift of the magnetic Zeeman ground sub-levels. The polarization of the standing wave varies between circular and linearly polarized over a distance equal to half a wavelength. This modulation produces an oscillating light shift of the ground state Zeeman sub-levels across the standing wave. Since this light shift varies in space due to the variation in the polarization the atom will experience different light shift potentials. If an atom in a particular magnetic sublevel is placed at a top of the potential, and absorbs a photon, it can decay to its original level or a different sublevel by spontaneous decay. It is likely that the atom will fall from the top of the potential into a valley, thus the atom will spend on average more time in climbing the potential hills. The atom will therefore convert its kinetic energy into potential energy by fluorescence. This cooling mechanism will continue until the atoms are located in the potential wells. The final achievable temperature is therefore related to the depth of the potential well $k_B T = \frac{\hbar\Omega_R^2}{4\Delta}$, where Ω_R is the Rabi-frequency. This indicates that the temperature can be reduced by increased detuning or reduced intensity. However there is a fundamental limit, the recoil limit. This is reached when the de-Broglie wavelength of the atom is about equal to the wavelength of the light, so the energy gained from a photon recoil becomes equal to or greater than the depth of the spatial potential wells. So the atomic wavepacket can no longer be localized in the potential walls, even if they are deeper than the photon recoil energy. This is the recoil limit, characterised by a temperature T_{rec} , which is the temperature at which an atom's r.m.s. velocity is equal to the recoil velocity $v_{rec} = \hbar k/m$ in each direction. Because the recoil limit is set by the energy of a single spontaneously emitted photon, it is possible to get away from it by using a final state of the atoms from which spontaneous emission is prohibited.

$$\frac{1}{2}k_B T_{rec} = \frac{p^2}{2m} = \frac{\hbar^2 k^2}{2m} \quad (5.8)$$

For a pair of circularly polarized beams($\sigma^+ \perp \sigma^-$ polarization gradient cooling) , a motion-dependent population difference occurs. The nature of the polarization gradient is different in this case. Here the polarization is linear throughout the standing wave and rotates in orientation such that it forms a helix. This drives π transitions ($\Delta m_F = 0$) between the different magnetic sublevels. Stationary atoms will have population distributed evenly over all the ground state Zeeman sublevels, because they will be optically pumped by $\delta m_F = 0$, with less fraction of the population pumped by $\delta m_F = 1$. Only when atoms are in motion is this symmetry broken. Moving atoms, however, will experience a rotation of the quantization axis as they move along the beam. This is because the direction of linear polarization rotates along the axis of beam propagation, passing through 2π for every wavelength λ it travels. Because the optical pumping process takes a finite time, as the atom moves the population by $\delta m_F = 0$ lags the polarization direction change. It can be shown that atoms traveling towards the beam driving $\sigma+$ transitions are more likely to be $\delta m_F = +1$, with the reverse being true for atoms traveling towards the σ beam [63]. So the atoms scatter more photons from the beam that they are moving towards. The result is a viscous force which opposes the direction of motion, slowing and cooling the atoms.

The MOT configuration satisfies this $\sigma^+ \perp \sigma^-$ polarization gradient cooling case. But for sub-Doppler cooling to occur directly in the MOT, a special requirement needs to be satisfied. That is the Landé g-factors of the excited and the ground cooling levels are nearly equal. The Doppler cooling force is equal to zero for the so-called locking velocity $V_D = -g_e \frac{\mu_B B}{\hbar k}$. And the locking velocity of the sub-Doppler mechanism is $V_s = -g_g \frac{\mu_B B}{\hbar k}$. The sub-Doppler cooling process is efficient only for velocities near V_s . If the velocities V_D and V_s differ much, only a small number of atoms undergoes the sub-Doppler cooling, almost without influencing the total temperature of atoms. If the Landé g-factors of the excited and the ground cooling levels are nearly equal, then the locking velocity of the Doppler cooling force equals the locking velocity of the Sub-Doppler cooling force, which enables efficient sub-Doppler cooling [65, 15].

5.3 MOT Initial Result

Our first MOT was achieved on Nov. 2, 2012. Fig. 5.4 shows a picture of the fluorescence without B field on and the MOT with the B field on. The parameters used for this MOT are shown in table 5.1

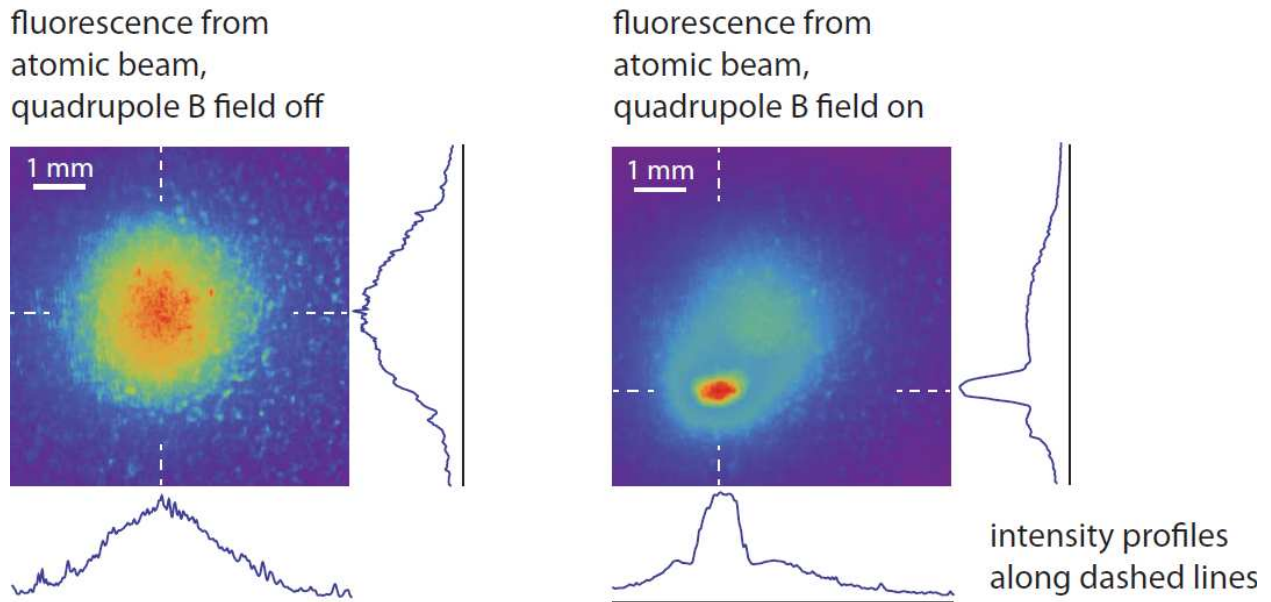


Figure 5.4 initial MOT picture

Table 5.1 Initial MOT parameters

MOT beams	57 mW each	Slowing beam	9 mW
MOT vacuum	1.5×10^{-8} Torr	Source vacuum	2.3×10^{-7}
Source Temperature	1150°C	B field current	20 A
CCD exposure time	0.08 s	EM gain	disabled

This was achieved with the second to last version of the laser system (including a verdi laser of 18 W at 532 nm, an M2 SolsTis Ti:Sapph laser of about 5.8 W at 821 nm, and our own home-made SHG cavity with LBO crystal), and the new vacuum system, in which atoms are loaded into the MOT from a high temperature effusion cell(Createc SFC-40-10-284-HL-WK-SHE-SC) with a

Tantalum crucible which contains ~ 15 grams of Holmium pieces. Details about the effusion cell and vacuum system are discussed in Chapter 2.

5.4 First trap operation

When the vacuum chamber and all the optics are in place, and the Ho is operating at high temperature around $1150\text{ }^{\circ}\text{C}$ and shooting into the trapping chamber, the steps for trying for the MOT is as following: Initially, monitor the operating temperature of the effusion cell, and then the pressure inside the trapping chamber. When the pressure is about $\sim 10^{-8}$ Torr or better, it is possible to see dim fluorescence where the trapping beams pass through the chamber with the trapping laser tuned to near-resonance. It is always easier to identify this fluorescence by slowly scanning the laser frequency and looking for a change on the camera image. After an adequate fluorescence has been seen, the magnetic field gradient is turned on and the lasers are reset to the appropriate frequencies and polarizations. If the apparatus being used has produced no MOT before, it will be a good practice to try both current directions through the MOT coils to determine the correct sign of the magnetic field for trapping. The trapped atoms should appear as a small bright cloud, much brighter than the background fluorescence. To verify that it is the MOT, one can see if it changes with the laser polarizations by turning the quarter-waveplates around the chamber or waving a piece of magnetic material and see if the MOT moves with it due to the changing position of zero magnetic field.

5.5 Imaging System

Measurements are carried out on the MOT by imaging with a CCD camera. An EMCCD camera(Andor LUCA-R) was used. This provides low noise and includes electron multiplication (EM) gain for use with low light applications as is the case for a weak MOT. The imaging system includes two lenses together with a blue filter (Semrock FF01-405/10-25) and an iris (for reducing background scattering) are attached to a lens tube mounted onto the camera housing. Light collected from the MOT is focused onto the CCD chip. The resolution of this imaging system

is $10\mu m/px$. And the performance is verified with an USAF chart. Fig. 5.5 shows the imaging system layout. And fig. 5.6 shows a picture of the imaging system and a USAF test image.

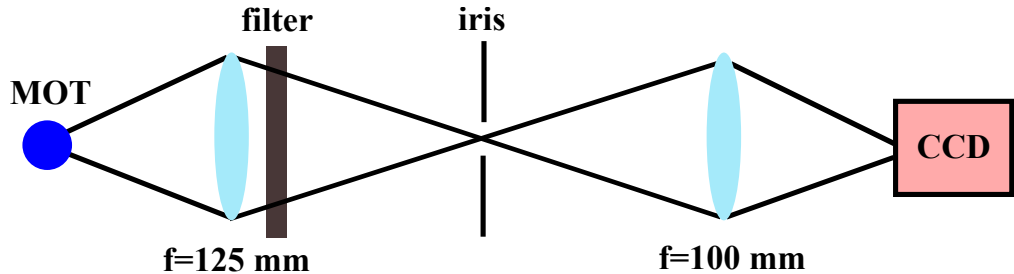


Figure 5.5 imaging system layout

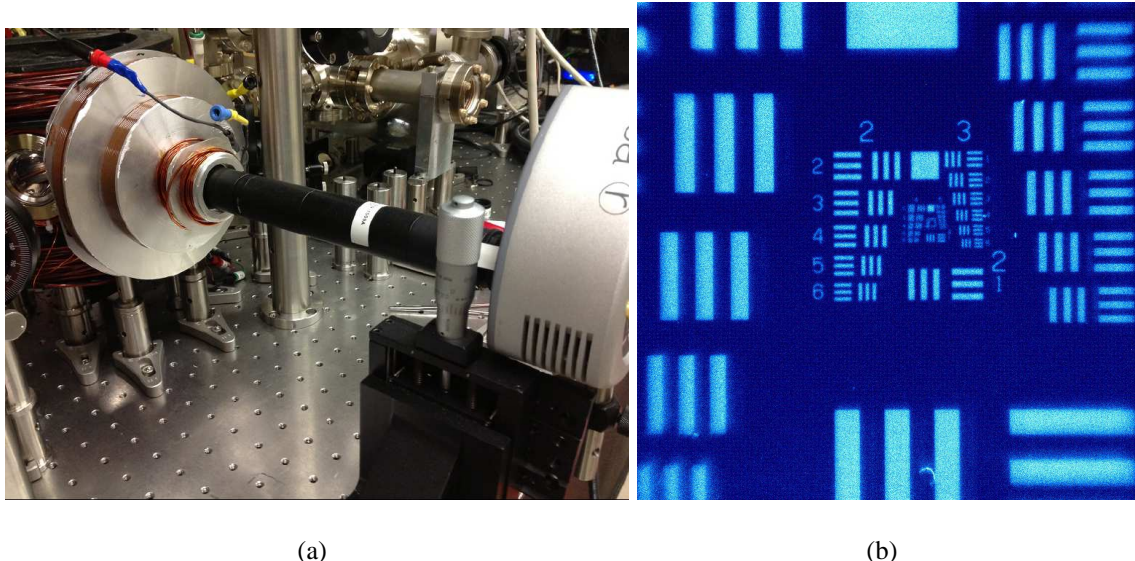


Figure 5.6 (a) a picture of the imaging system (b) a USAF test image with this imaging system

5.6 MOT characteristics

Many measurements could be made with the MOT, we should start by making some straightforward measurements: the total number of trapped atoms N , the atom density n_0 , and the temperature T . These measurements are all made by observing the fluorescence from the trapped atoms. Some absorption imaging measurements will be discussed later.

5.7 MOT population and density

The number of trapped atoms is basically determined by measuring the total amount of light scattered by the trapped atoms, and then dividing it with the amount of light scattered per atom, which is extracted from the excited state lifetime.

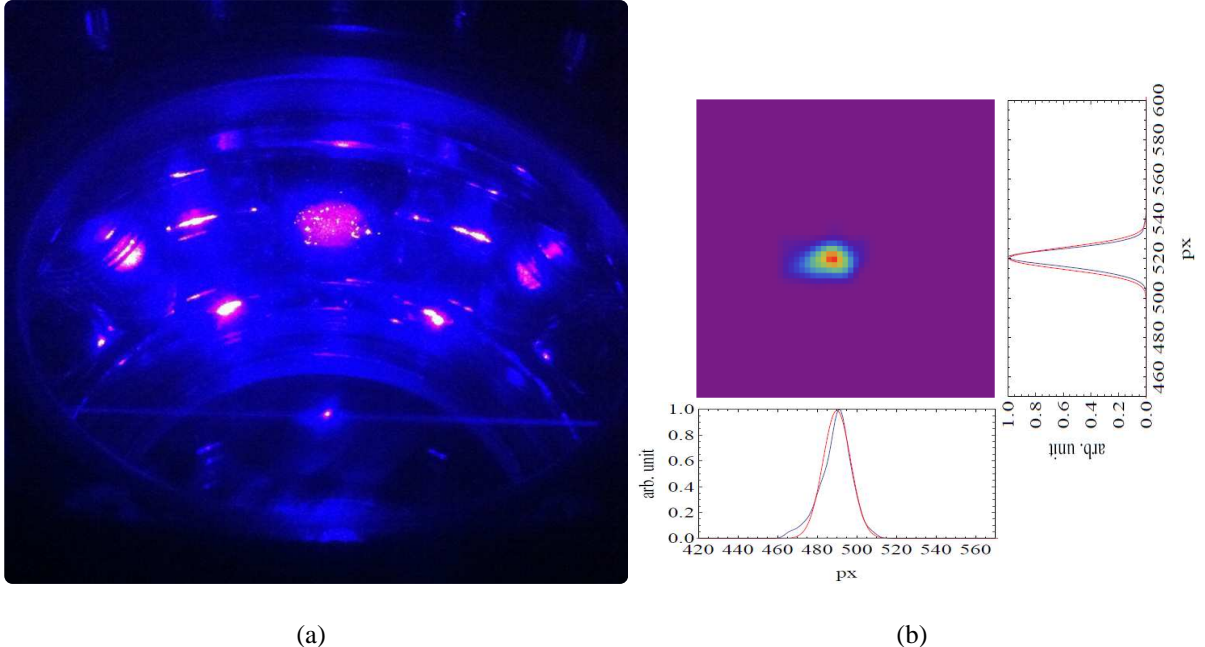


Figure 5.7 (a) A picture of the MOT inside the vacuum chamber (b) Gaussian fit to the MOT fluorescence image

An example of a fluorescence image of the MOT, taken using the image system described before is shown in fig. 5.7. The center of the MOT, the point of highest density, is found by locating the pixel with the highest photon count. Slices of the image are then cut through this point in horizontal and vertical direction. Both slices are fit with a Gaussian profile. The number of atoms present in the image can be evaluated from the total level of fluorescence detected at the CCD.

From equation (1.3) and using the relationship $I/I_s = 2\Omega^2/\Gamma^2$, we rewrite equation (1.3) as

$$\Gamma_s = \frac{\Gamma}{2} \frac{I/I_s}{1 + I/I_s + 4(\frac{\Delta}{\gamma})^2} \quad (5.9)$$

where I is the sum of the intensities of the six trapping beams, Δ is the detuning from resonance, and I_s is the $2.7 \times 61 mW/cm^3$ saturation intensity. Δ is set by sending an RF frequency of $1 \sim 2\gamma$ to an AOM in the branch of the hollow cathode holmium lamp. The zeroth order goes to the MOT, and the plus first order goes to the hollow cathode lamp. Therefore the cooling beams are red detuned to resonance. The high-finesse reference cavity PTZ is locked to the error signal from the holmium lamp. A typical number for R in our experiments is 4×10^6 photons/ (s × atoms). Normally we use the linewidth $\gamma = \Gamma/(2\pi)$ of 32 MHz with frequency unit for convenience with the corresponding detuning also in MHz.

To determine the temperature and number of atoms in the MOT, a calibrated CCD camera (Andor Luca-R) is used to perform fluorescence imaging. This is set up with $\times 1.25$ magnification to give $10 \mu\text{m}/\text{pixel}$. The atom number is calculated from summing over the pixel counts using

$$N_{atom} = \frac{1}{(\Omega/4\pi)\kappa\Gamma_s\tau_{ex}} \sum_{px} C_{px} \quad (5.10)$$

where κ is the camera quantum efficiency, which is 0.227 count/photon (Calibration of Andor Luca-R camera, @ 410 nm, EM Gain = 1) [66]. τ_{ex} is the camera exposure time. Γ_s is the photon scattering rate per atom, $\Omega/4\pi$ is the solid angle collection efficiency. The collection solid angle of the imaging lens is $\Omega = \pi r^2/d^2$, where $r = 12.7$ mm is the lens radius, and $d = 125$ mm is the distance from the MOT to the lens. $\sum_{px} C_{px}$ is the total pixel counts in the MOT, which is obtained by doing a Gaussian curve fit to the fluorescence image with the measured maximum pixel counts in the MOT center as the fit amplitude.

The atom density (at the center of the MOT) is approximated by assuming the MOT has a Gaussian profile with equal waist in x, y and z directions, which is given by

$$\rho(0) = \frac{N_{atom}}{(2\pi)^{3/2}w^3} \quad (5.11)$$

where w is the averaged waist of the MOT extracted from Gaussian fits to the fluorescence images.

We achieved a MOT population of $\sim 10^6$ with atom density of $\sim 10^{10}/cm^3$ A typical set of parameters used is shown in table 5.2.

Table 5.2 MOT Parameter Set

B field	20 A of current, 20 G/cm
Temperature of source	1150 °C
Pressure in MOT chamber	3×10^{-9} Torr
Pressure in Ho source chamber	2×10^{-8} Torr
Cooling beams power	225 mW in total, 75 mW in each
Cooling beams waist	~ 6 mm
Cooling beams detuning	- 50 MHz
Slowing beam power	70 mW
Slowing beam detuning	~ - 320 MHz
Camera EM gain	1
Camera exposure time	400 μ s

5.8 Optimising the MOT population

Various parameters can be used to improve the number of atoms in the trap.

The total force in a MOT is a combination of the light scattering force and magnetic field gradient force [48]

$$F_{MOT} = -\alpha v - \frac{\alpha}{k} \beta z \quad (5.12)$$

where $\beta = \frac{g\mu_B}{\hbar} \frac{dB}{dz}$ with $g = g_{F'}m_{F'} - g_F m_F$. α is the damping coefficient proportional to the scattering force.

Increasing intensity I enlarges the scattering force, however it will also saturate this force to $F_{scatt} = \hbar k \Gamma / 2$. Equation 5.12 also show that the force in the MOT also depends on the magnetic field gradient. The maximum achievable atom number was got with a MOT gradient of 20 G/cm and a detuning of - 47 MHz by adjusting the position of the magnetic field coils, the strength of the field gradient, the frequencies of both trapping and slowing lasers, the beam alignments, and the polarizations of the beams.

5.9 Trap temperature

When the atoms are initially trapped in the MOT, they exhibit a Gaussian position distribution. Start with considering 1D distribution,

$$P(x_i) = \sqrt{\frac{2}{\pi w_x(0)^2}} \exp\left(-\frac{2x_i^2}{w_x(0)^2}\right) \quad (5.13)$$

The 1D Maxwell Boltzmann velocity distribution is given by

$$f(v_x) = \left(\frac{m}{2\pi k_B T_x}\right)^{1/2} \exp\left(-\frac{mv_x^2}{2k_B T_x}\right) \quad (5.14)$$

where T_x is the temperature in 1D and m is the mass of holmium atoms. As the cloud expands over a period of time t , the position $x(t)$ of one atom is given by

$$x(t) = x_i + v_x t \quad (5.15)$$

Combined with the Maxwell Boltzmann distribution, we get

$$f(v_x) = \left(\frac{m}{2\pi k_B T_x}\right)^{1/2} \exp\left(-\frac{m(x - x_i)^2}{2k_B T_x t^2}\right) \quad (5.16)$$

The position distribution as a function of time is then given by

$$P(x, t) = \int_{-\infty}^{\infty} P(x_i) f(v_x) dx_i = \int_{-\infty}^{\infty} P(x_i) f(x - x_i) dx_i = P(x_i) \otimes f(v_x) \quad (5.17)$$

The final position distribution is a convolution of the initial position distribution and the velocity distribution. Because both distributions are Gaussian, the final distribution will also be Gaussian with a waist given by the quadrature sum of both waists. From equation (5.13) and (5.16), the waist of the cloud as it expands is

$$w_x(t) = \sqrt{w_x(0)^2 + \frac{4k_B T_x}{m} t^2} \quad (5.18)$$

The MOT temperature of the atoms was therefore measured using this time of flight method (TOF) [67] [68], where the cloud of atoms is allowed to expand freely for a small period of time, within which a series of images of the atom cloud originally in the MOT are taken with a CCD

camera. By making a plot of the Gaussian waist of the cloud at different expansion times, and fitting it with the equation 5.18 above, the values of the initial waist of the cloud $w_x(0)$, and the temperature T_x can be both determined. During the expansion time, the lasers and the magnetic field are turned off. Measurements with magnetic coils on gave no atom cloud expansion due to magnetic trapping.

For this measurement we set the MOT free expansion time to be starting at ~ 2.5 ms and ends at ~ 6 ms, to avoid the eddy current effect after the MOT coils current turns off. A measurement of the eddy current effect was taken with a test coil with about 20 turns of thin wires, put right above the MOT chamber. The test coil was connected to an oscilloscope for observing the eddy current effect after the MOT coils are turned off. The main peak of the eddy current produced a voltage of 9.7 V and lasted until 236 μ s after the coil was shut off. Then started at 1.3 ms a series of oscillations decayed from 440 mV and ended at 2.3 ms after the power to the coils was shut off. The longest time the TOF measurement can be chosen is in principle limited by the time taken for the MOT to expand out of the field of view of the CCD camera. And in our case since the field of view is large enough, it is limited by the time that it gets too weak to be considered as an atom cloud signal compared to the noise background.

The MOT parameters were optimized to give the greatest number of atoms for a given source temperature(typically around $1150^{\circ}C$). An example of our temperature measurement is shown in fig. 5.8, with temperature result of $356.2(\pm 6.8)\mu K$ in the vertical direction and $220.3(\pm 10.1)\mu K$ in horizontal direction. This data was taken at $s = 1.1, \Delta = -42MHz, \nabla B_z = 20G/cm$.

5.9.1 Sub-Doppler Cooling

The coldest temperature is obtained at large detuning, giving temperature below the Doppler limit of $T_D = 780\mu K$ of holmium, however at the cost of MOT population.

Efficient sub-Doppler cooling was observed in our MOT, comparing to the Doppler Temperature. Mainly due to the degeneracy of the ground state g-factor ($g_{F11}=0.82$) and the excited state g-factor ($g_{F12}=0.83$). (Table 5.3 shows the lander g factors of the ground and excited hyperfine

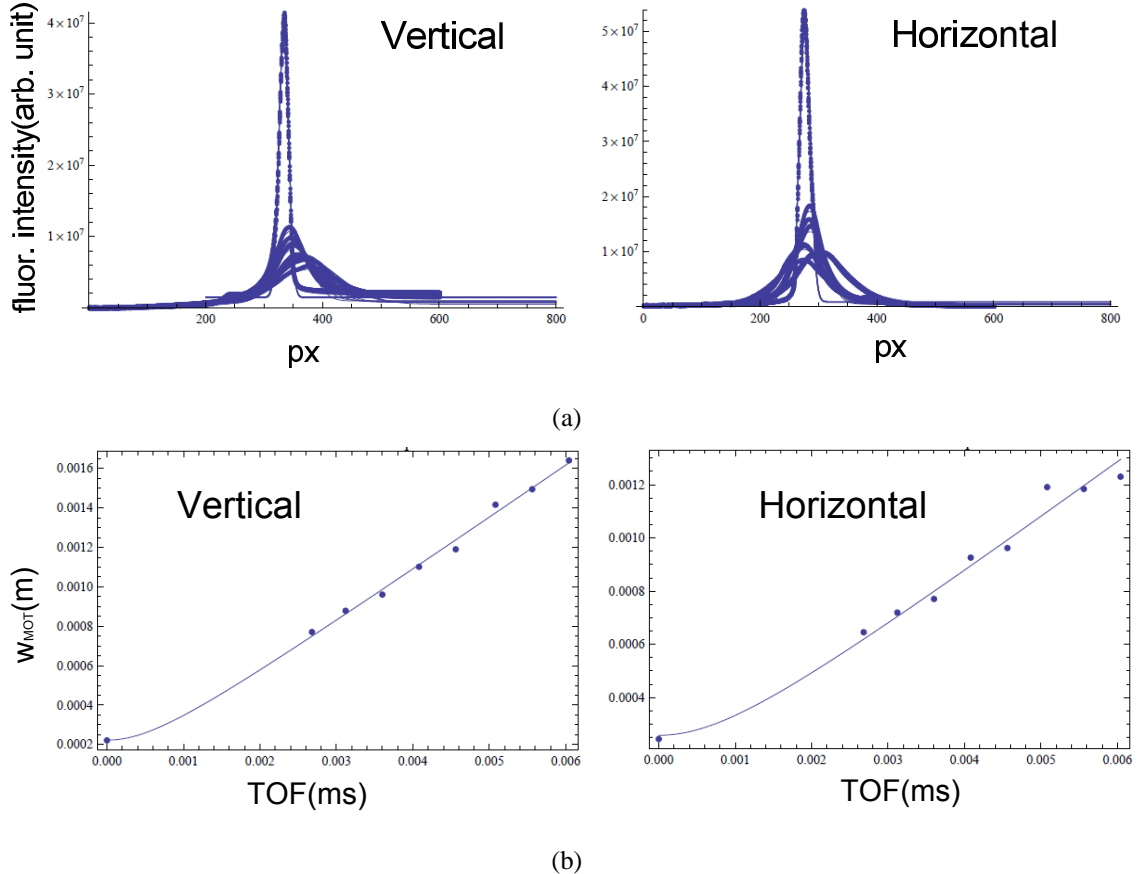


Figure 5.8 an example result of temperature measurements (a) Gaussian fit to MOT width at different TOF (b) fit width of MOT and temperature curve fit to data

states of the cooling transition at 410.5 nm) So the locking velocity for the Doppler and the sub-Doppler forces are nearly equal. A more detailed discussion is in [65]. The minimum temperature we achieved was about $75 \mu\text{K}$ in the vertical direction of the MOT, with $\Delta = -2\gamma$.

Table 5.3 Landé g-factors of the ground and excited hyperfine states of the cooling transition at 410.5 nm

ground F	4	5	6	7	8	9	10	11
g-factor	2.040	1.560	1.286	1.114	1.000	0.920	0.862	0.818
excited F	5	6	7	8	9	10	11	12
g-factor	1.863	1.499	1.271	1.119	1.013	0.936	0.878	0.833

An approximate expression for the dependence of the MOT temperature with respect to detuning is given by [69, 70]:

$$T = T_0 + a \frac{\hbar\Gamma}{2k_B |\delta|} \frac{\Gamma}{I_s} I \quad (5.19)$$

A result of the MOT temperature as a function of cooling beam detuning is shown in fig 5.9, with theoretical curve fit using Eq.5.19.

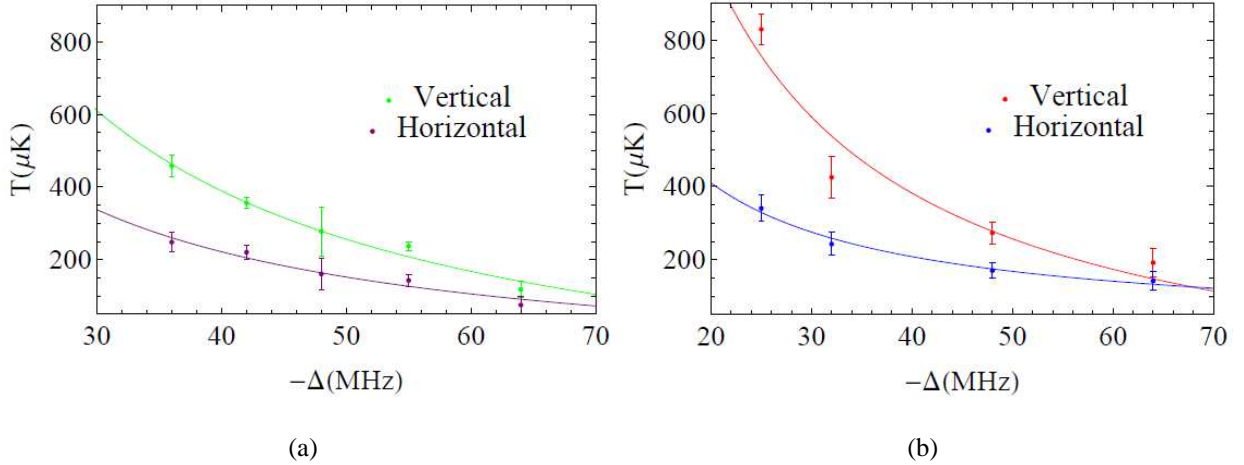


Figure 5.9 MOT temperature vs cooling light detuning (a) taken at $s = 1.1$ (b) taken at $s = 1.5$

5.10 Characterization of Repumper

The effect of a repumper (aiming at the transition of $|F_g = 10\rangle$ to $|F_e = 11\rangle$) , blue-detuned to cooling beams, on the MOT population was also evaluated. Fig. 5.10 shows the level diagram and the cooling and repumping transitions. The repumping transition is +600 MHz higher than the cooling transition. With slowing beam on, the repumper does not obviously change the MOT population, which is typically 10^6 . As the repumper beam being switched between on and off over time, up to 5% of the MOT population change was observed, which is the same as the background fluctuation during the operation without the repumper beam. With slowing beam off, the MOT population is largely reduced, which is only several thousands, adding the repumper does improve the MOT population, up to about a factor of two with the optimum detuning. Fig. 5.11 shows the effect of the repumper on the MOT population with the slowing beam off. The data cuts off at

$\Delta = 620 MHz$ because of the tuning limit of our AOM. Note that the detuning is with respect to cooling transition of $|F_g = 11\rangle$ to $|F_e = 12\rangle$, which is on resonance for the repumping transition at around 600 MHz detuning. This result indicates that with the slowing beam on, the MOT population is well pumped to the $|F_g = 11\rangle$ ground state.

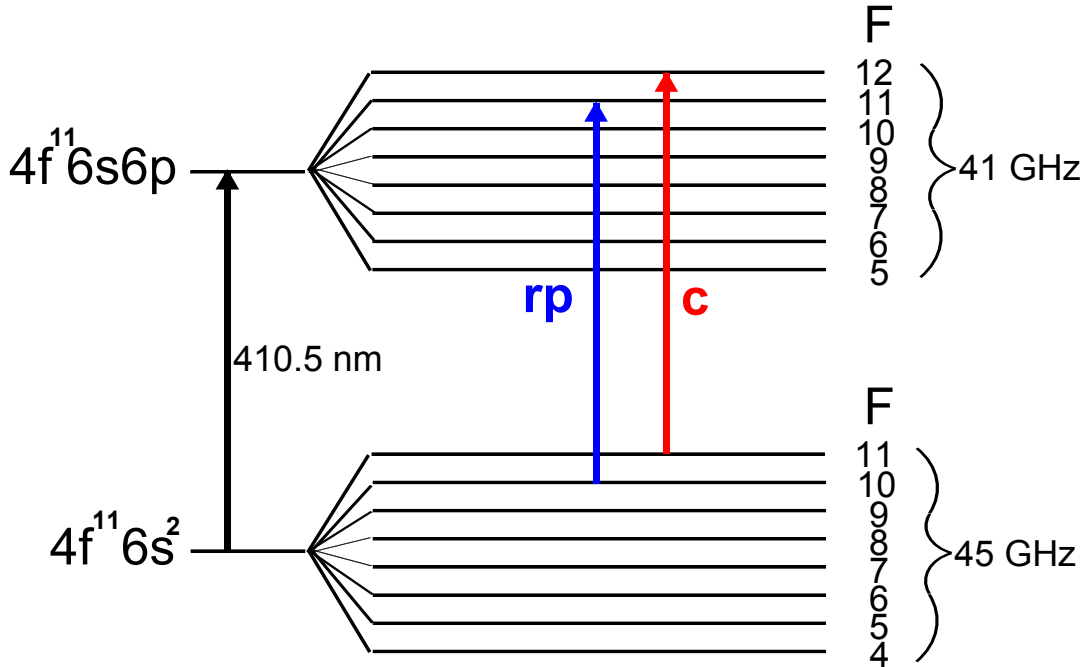


Figure 5.10 level diagram and transitions of the cooling and repumping transitions

5.11 Absorption Imaging Analysis

Besides fluorescence imaging analysis, absorption imaging was also used. A probe beam opposing the camera is illuminated from the side on the MOT. This probe beam is prepared with a pick-off from the cooling beam passing through AOMs and fibers. We prepared two different probe beam frequencies aiming at the transitions of $|F = 11\rangle$ to $|F' = 12\rangle$, and the $|F = 10\rangle$ to $|F = 11\rangle$. We observed absorption in the $|F = 11\rangle$ to $|F' = 12\rangle$ transition, but no absorption in the $|F = 10\rangle$ to $|F = 11\rangle$ transition. Fig 5.13 shows the pictures of the $|F = 11\rangle$ to $|F' = 12\rangle$ transition, with the background image (no atoms, no probe beam), The probe beam image (no atoms,

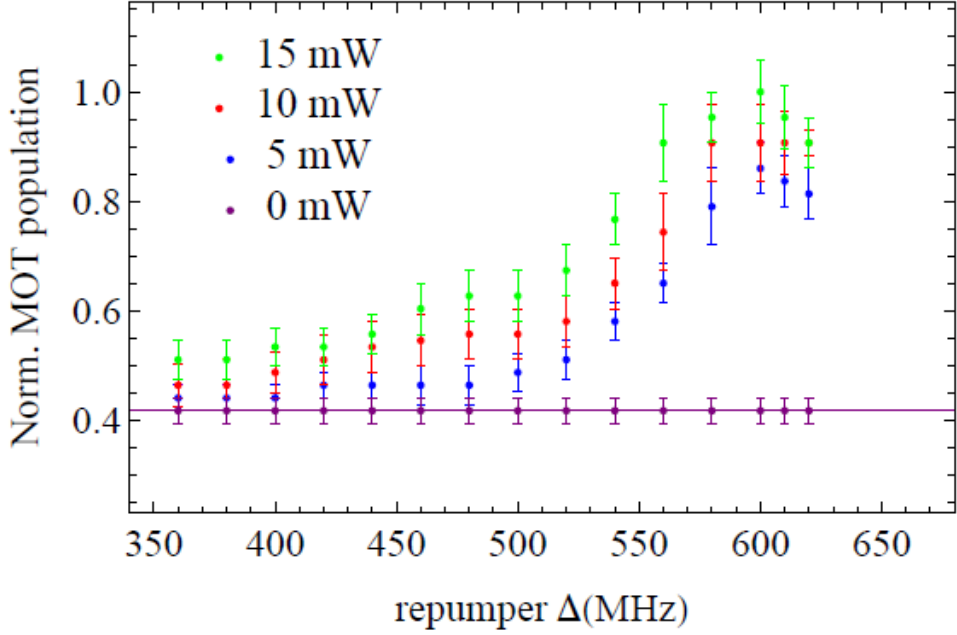


Figure 5.11 MOT population vs. repumper detuning, with slowing beam off, taken at different repumper beam powers from 0 to 15 mW.

probe beam on), and the signal image (atoms and probe beam on). Fig. 5.12 shows the level diagram and the cooling and two probe beam transitions. The pulse length of the absorption beam was $8 \mu\text{s}$, and the camera exposure time used was $400 \mu\text{s}$ with an EM gain of 25.

For the absorption images taken above, the optical depth of the absorption, which is defined as $OD = e^{(-OD)}$, with I being the transmitted intensity and I_0 being the incident intensity, is extracted by using

$$OD = -\ln\left(\frac{I_s - I_b}{I_p - I_b}\right), \quad (5.20)$$

and then the Gaussian fits to the extracted optical depth in horizontal and vertical directions are shown in fig 5.14. This fit results in an averaged central OD of 0.8, with a waist of $165 \mu\text{m}$. The central density n_0 is then calculated by using

$$OD = \int_{-\infty}^{\infty} \sigma n_0 e^{\left(\frac{2x^2}{w^2}\right)} dx \quad (5.21)$$

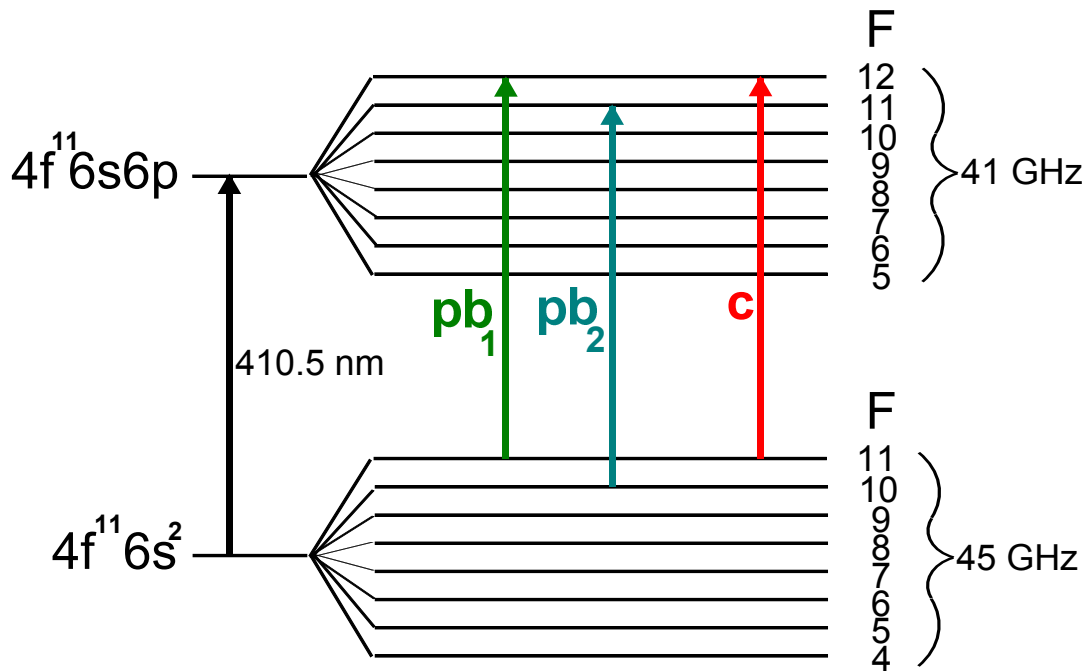


Figure 5.12 level diagram and transitions of the cooling and two probe beam transitions

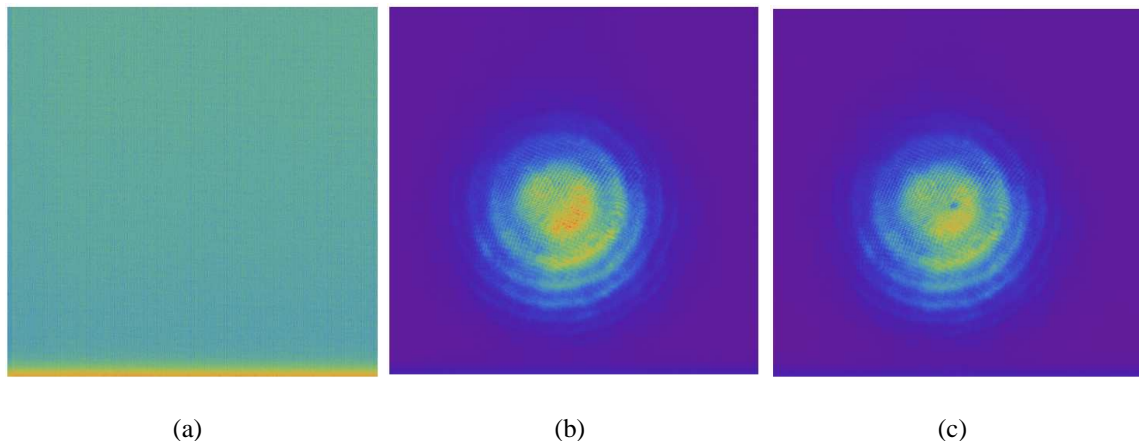


Figure 5.13 Absorption imaging pictures (a) background image (I_b) (b) probe beam image (I_P)
(c) signal image (I_s)

where $\sigma = \frac{3\lambda^2}{2\pi}$ is the scattering cross section, with $\lambda = 410.5nm$.

Then we ended up with $n_0 = 4.7 \times 10^{10}/cm^3$. To compare, Fluorescence imaging was also taken under the same experimental condition, and gives an atom density of $1.9 \times 10^{10}/cm^3$.

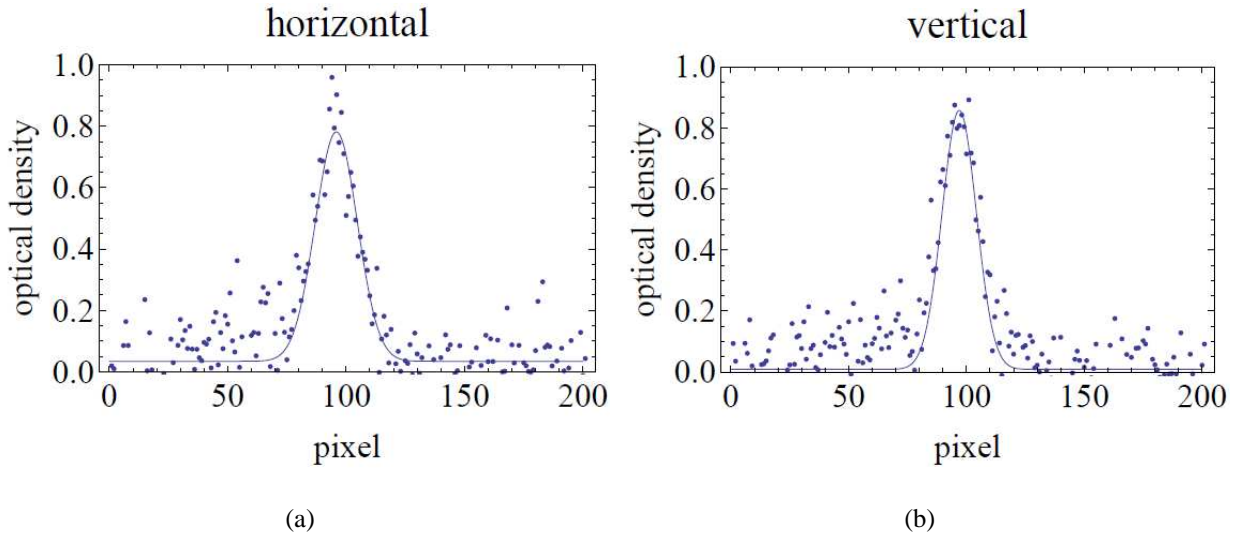


Figure 5.14 Gaussian Fits to the absorption images (a) in vertical direction (b) in horizontal direction

5.12 Summary

This chapter covers theoretic overview of laser cooling and magneto-optical trapping, and the experimental results of the holmium MOT. The MOT population, density, temperature, and efficient sub-Doppler cooling are discussed. The effect of the repumping beam on the MOT population is investigated. And the fluorescence imaging and absorption imaging result of the MOT density are compared. A paper reporting these results is in preparation.

Chapter 6

Optical Pumping

In the MOT and optical molasses, atoms are uniformly distributed over a range of m_F states due to the interaction with the light field. For our future quantum computing work, the atoms need to be prepared into the target reservoir state, either $|F = 11, m_F = 11\rangle$ stretched state or $|F = 11, m_F = 0\rangle$ dark state.

Two of the optical pumping schemes that can be used are illustrated in the following sections. The first one is bright-state pumping using σ^+ cooling transition to pump population across to the $|F = 11, m_F = 11\rangle$ stretched state. The second one is dark-state pumping using π -polarized light, to pump the population to the $|F = 11, m_F = 0\rangle$ dark state.

6.1 Theoretical Model

Assume that field E_{ik} couples initial state $|i\rangle$ and final state $|k\rangle$ with frequency ω_{ik} . i.e. $E_{ik} = E_{ki} = \langle i | \hat{E} | k \rangle$. The density matrix is defined as $\rho = \sum_{nm} |n\rangle \langle m|$. If we only account for the coherent evolution ($i\hbar = [\hat{H}, \hat{\rho}]$) driven by the external fields, then the Hamiltonian is

$$H = \sum_{i=1}^N U_i |i\rangle \langle i| - \sum_{i=2}^N \sum_{k=1}^{i-1} (E_{ik} d_{ik} |i\rangle \langle k| + E_{ik}^* d_{ik}^* |k\rangle \langle i|) \quad (6.1)$$

where U_i is the energy of each atomic state, and the electric dipole is $d_{ik} = \langle i | \hat{d} | k \rangle$. Then we reach

$$i\hbar \frac{d\rho}{dt} = \sum_{i,m}^N U_i (\rho_{im} |i\rangle \langle m| - \rho_{mi} |m\rangle \langle i|) + \sum_{k,i,m} (E_{ik} d_{ik} \rho_{mi} |m\rangle \langle k| - E_{ik} d_{ik}^* \rho_{im} |k\rangle \langle m|) + \sum_{k,i,m} (E_{ik} d_{ik}^* \rho_{mk} |m\rangle \langle i| - E_{ik} d_{ik} \rho_{km} |i\rangle \langle m|) \quad (6.2)$$

Taking matrix elements by operating with $\langle m | \dots | m \rangle$ onto the density matrix, to get the populations terms

$$i\hbar \frac{d\rho_{mm}}{dt} = \sum_{k=1}^N E_{im} (d_{im} \rho_{mi} - d_{im}^* \rho_{im}) \quad (6.3)$$

Taking matrix elements by operating with $\langle n | \dots | m \rangle$ to get the coherence terms

$$\begin{aligned} i\hbar \frac{d\rho_{nm}}{dt} &= (U_n - U_m) \rho_{nm} + \sum_{i=2}^N (E_{im} d_{im} \rho_{ni} - E_{in} d_{in}^* \rho_{im}) \\ &\quad + \sum_{k=1}^{m-1} E_{mk} d_{mk}^* \rho_{nk} - \sum_{k=1}^{n-1} E_{nk} d_{nk} \rho_{km} \end{aligned} \quad (6.4)$$

With $E_{im} = \frac{\varepsilon_{im}}{2} e^{-i\omega_{im}t} + \frac{\varepsilon_{im}^*}{2} e^{i\omega_{im}t}$, $\rho_{im} = \tilde{\rho}_{im} e^{-i\omega_{im}t}$, $\omega_{mi} = -\omega_{im}$ and dropping the fast rotating terms(of $\sim 2\omega$), we reach the form

$$\frac{d\rho_{mm}}{dt} = -\frac{i}{2} \sum_{i=1}^N (\Omega_{im} \tilde{\rho}_{mi} - \Omega_{im}^* \tilde{\rho}_{im}) \quad (6.5)$$

$$\frac{d\tilde{\rho}_{nm}}{dt} = i\Delta_{nm} \tilde{\rho}_{nm} - \frac{i}{2} \left[\sum_{i=1}^N (\Omega_{mi}^* \tilde{\rho}_{ni} - \Omega_{ni} \tilde{\rho}_{im}) \right] \quad (6.6)$$

where $\Delta_{nm} = \omega_{nm} - \frac{1}{\hbar}(U_n - U_m)$, $\Omega = \frac{\varepsilon d}{\hbar}$, $\tilde{\rho}_{mi} = \tilde{\rho}_{im}^*$.

Now let's include spontaneous decay terms to get the final form

$$\frac{d\rho_{mm}}{dt} = - \sum_{k=1}^{m-1} \gamma_{mk} \rho_{mm} + \sum_{k=m+1}^N \gamma_{km} \rho_{kk} + \frac{i}{2} \sum_{i=1}^N (\Omega_{im}^* \tilde{\rho}_{im} - \Omega_{im} \tilde{\rho}_{mi}) \quad (6.7)$$

$$\frac{d\tilde{\rho}_{nm}}{dt} = -\frac{1}{2} \left(\sum_{l=1}^{n-1} \gamma_{nl} + \sum_{l=1}^{m-1} \gamma_{ml} \right) \tilde{\rho}_{nm} + i\Delta_{nm} \tilde{\rho}_{nm} - \frac{i}{2} \left[\sum_{i=1}^N (\Omega_{mi}^* \tilde{\rho}_{ni} - \Omega_{ni} \tilde{\rho}_{im}) \right] \quad (6.8)$$

Note that equations (6.7) and (6.8) that determine how the whole density matrix evolves with time, do not only depend on the coherences driven by external fields that directly couple pairs of states, but also depend on coherences that are not driven by any external fields.

6.2 Optical Pumping in Holmium

6.2.1 $\sigma+$ polarized laser beam case

To consider the optical pumping of the Holmium ground states, we start with the ground state levels $|F_g = 10\rangle, |F_g = 11\rangle$, coupling to excited levels $|F_e = 11\rangle, |F_e = 12\rangle$, with $\sigma+$ polarization. And ground state levels from $|F_g = 4\rangle$ to $|F_g = 10\rangle$ are coupled with π -polarized microwave. To decrease the number of variables, which is also the number of equations that we need to solve, we count only the number of populations and the number of coherences that have to be included in our equation set. There are 176 states (128 ground states and 48 excited states) included for populations. For coherences, the pumping beam coupling ground states in $|F_g = 11\rangle$ and excited states in $|F_e = 12\rangle$, and the repumper coupling ground states in $|F_g = 10\rangle$ to excited states in $|F_e = 11\rangle$ gives 44 coherences. The six microwave fields coupling $|F_g = 4\rangle$ and $|F_g = 5\rangle, |F_g = 5\rangle$ and $|F_g = 6\rangle \dots |F_g = 9\rangle$ and $|F_g = 10\rangle$ gives 84 coherences. The non-driven coherences between ground states $|F_g = 4\rangle \sim |F_g = 9\rangle$ and excited state $|F_e = 11\rangle$ gives 259 coherences. So the total number of variables in this model is 563. Thus we can solve the 563 equations numerically to get the final population of any state of interest after evolving with time. A diagram showing the energy levels and the coupling fields of this case is shown in fig. 6.1.

To convert these equations into numerical form, we need a few more definitions. Assume that the excited states with angular momentum $J = J_e$ decay only to ground state manifold $J = J_g$. The upper and lower manifolds are split into hyperfine levels with angular momentum F due to interaction with the nuclear spin I . The nuclear spin as well as the intrinsic electron spin S are constants of the motion. In this situation the decay γ_{kj} from $|k\rangle = |n_k, L_k, S, J_k, I, F_k, M_k\rangle$ to $|j\rangle = |n_j, L_j, S, J_j, I, F_j, M_j\rangle$ is given by

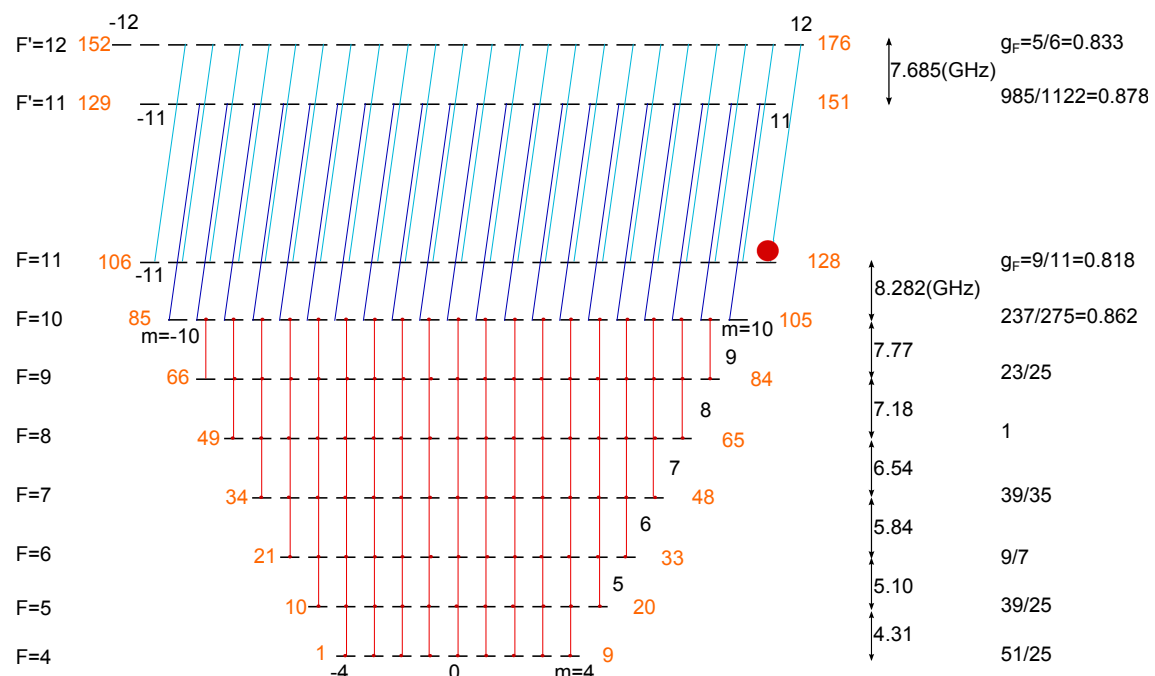


Figure 6.1 $\sigma+$ case Holmium optical pumping. Orange lines represent the π -polarized microwave field, deep blue lines represent the $\sigma+$ repumping field, and light blue lines represent the $\sigma+$ pumping field.

$$\gamma_{kj} = \gamma \times \gamma_{kj}^2 = \gamma_{E1} \times \frac{2F_k + 1}{2F_+ + 3} \left(\frac{S_{F_k J_k 1}^{J_j F_j I}}{S_{F_+ + 1, J_e, 1}^{J_g F_+ I}} \right)^2 \left(\frac{C_{F_k, M_k, 1, M_j - M_k}^{F_j M_j}}{C_{F_+ + 1, F_+, 1, -1}^{F_+ F_+}} \right)^2 \quad (6.9)$$

where the total dipole allowed decay rate out of $|k\rangle$ is $\gamma_{E1} = \sum_j \gamma_{kj} = 204 \times 10^6 S^{-1}$.

For microwave coupled coherences, the magnetic dipole moments coupling $|FM\rangle \rightarrow |F + 1, M\rangle$ are

$$\mu_{FM} = (\mu_B g_J) (-1)^{F+I+J+1} \sqrt{(2F+1)J(J+1)(2J+1)} \left\{ \begin{array}{ccc} J & I & F \\ F+1 & 1 & J \end{array} \right\} C_{FM10}^{F+1M} \quad (6.10)$$

The target pumping state of this case is the ground state $|F = 11, M_F = 11\rangle$ state. The simulation result of this case with initial population evenly distributed in all ground levels is shown in fig. 6.2. The total time in the plot is $1000/\gamma = 49\mu s$. The final result is 95.2% population in the target stretched state.

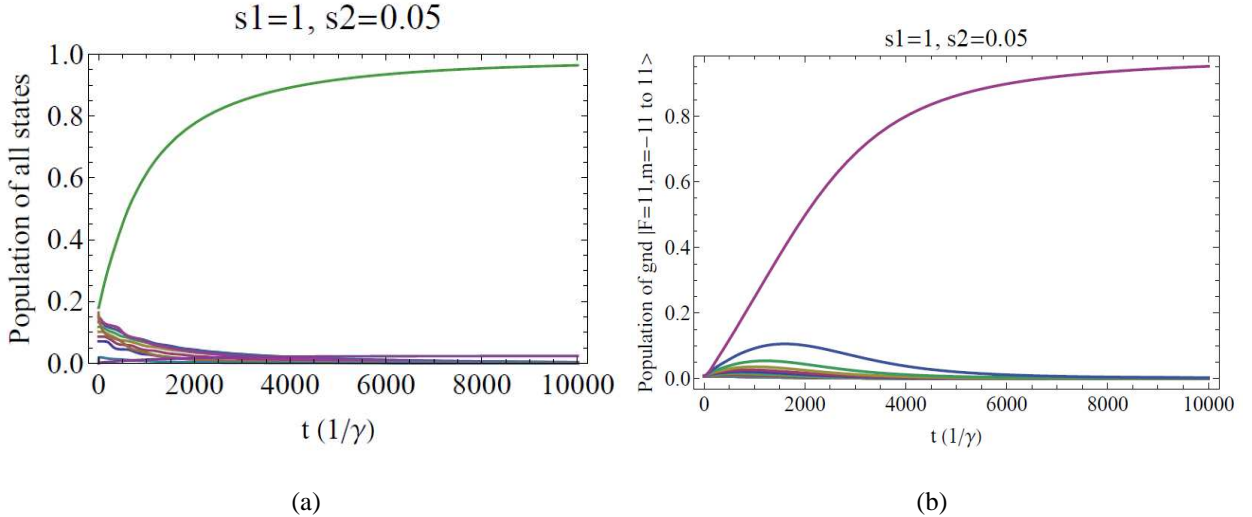


Figure 6.2 (a) Population of all F states (b) Population of target state.

6.2.2 π -polarized laser beam case

Now let's consider the case using π polarized light to prepare the population onto the target $|F_e = 11, M_F = 0\rangle$ dark state. The pumping beam couples the ground states of $|F_g = 11\rangle$ to the

excited states of $|F_e = 11\rangle$, and the repumper couples the ground states of $|F_g = 10\rangle$ to the excited states of $|F_e = 11\rangle$. The microwave couplings are the same as the $\sigma+$ optical pumping case discussed previously. The number of variables, thus the number of equations is 538, which includes 151 of population and 387 coherences. A diagram showing the energy levels and the coupling fields of this case is shown in fig. 6.3. And the simulation result of this case with initial population evenly distributed in all ground levels is shown in fig. 6.4. The final result is that 98.7% population in the target dark state after $980 \mu s$ ($2 \times 10^5 \gamma$).

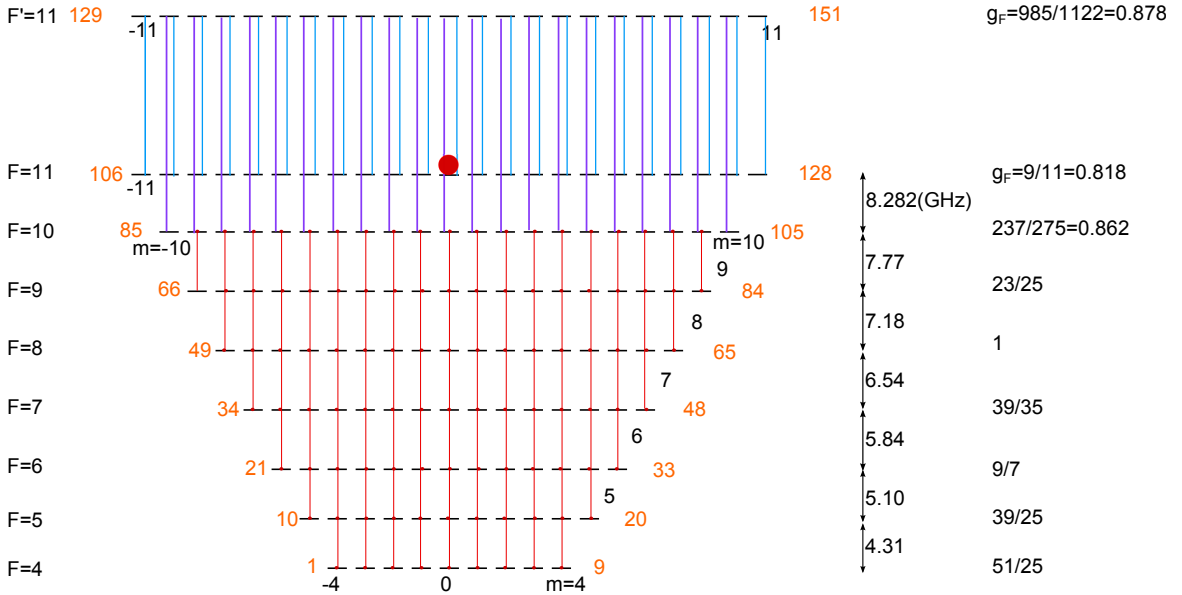


Figure 6.3 π case Holmium optical pumping. Orange lines represent the π -polarized microwave field, deep blue lines represent the π repumping field, and light blue lines represent the π pumping field.

6.3 Summary

In Summary, two types of optical pumping schemes (stretched state pumping and dark state pumping) are discussed for state preparation of the quantum computing. According to our experimental observation of the effect of the repumping beam coupling ground $F = 10$ and excited $F' = 11$ hyperfine states, the atoms trapped in the MOT are already well pumped into the ground $F = 11$ state. Therefore the optical pumping model can be much more simplified.

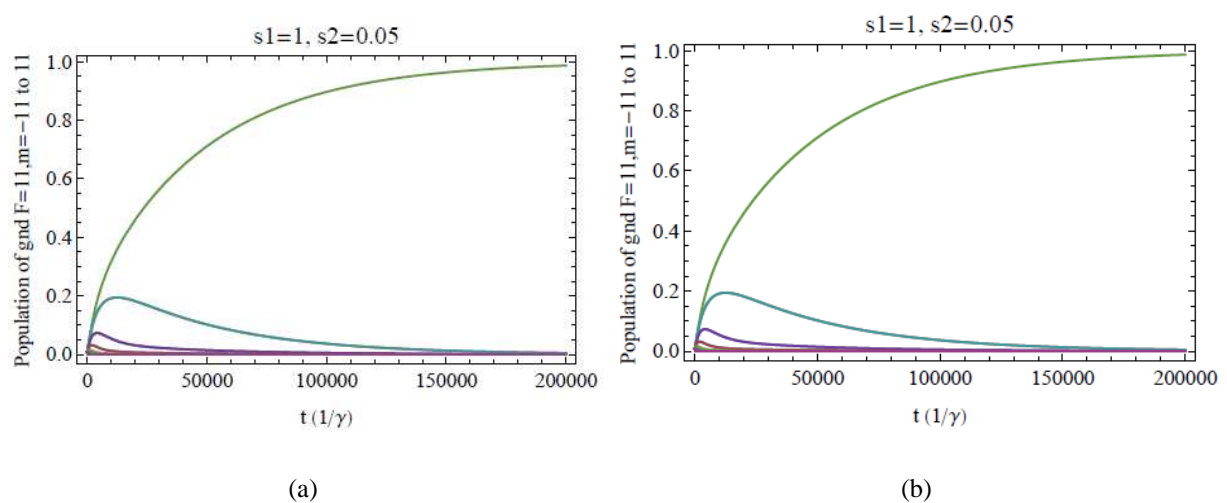


Figure 6.4 (a) Population of all F states (b) Population of target state.

Chapter 7

Summary and Outlook

7.1 Summary

An experiment on laser cooling and trapping holmium atoms was designed and constructed during the course of my PhD study. During the course of this work we have explored several versions of laser systems, and two main versions of vacuum systems. We constructed diode lasers at 410.5 nm then gave up, due to the limits of power, and difficulty to stabilize the frequency. In order to achieve high power at 410.5 nm, we chose to frequency double infrared light at 821 nm using nonlinear crystals. We succeeded in achieving the holmium MOT with our second last version of laser system and our last version of vacuum system in Nov. 2012. A more powerful fully commercial laser system was used to replace the previous one to achieve higher power, thus larger population in the MOT.

Experimental data are presented on the MOT characteristics such as population of $\sim 10^6$, atom density of $10^{10}/cm^3$ and temperature down to $\sim 100\mu K$. Ho MOT has also shown efficient sub-Doppler cooling as Er and Dy have recently demonstrated, due to the near degeneracy of ground-and-excited-state Lande g factors.

In addition, the hyperfine spectroscopy results were taken for the strong cooling transition at 410.5 nm with 32 MHz linewidth, and a comparably strong transition at 416 nm with 106 MHz linewidth were presented. And measurements of the hyperfine coefficients of the excited state of the cooling transition are discussed.

A theoretical model of the hybrid optical pumping was built for state preparation into a hyperfine Zeeman sublevel, as a starting point of building the quantum register. Two approaches

are discussed: the $\sigma+$ bright-state pumping approach, and the π dark-state pumping approach. Pumping efficiency for the two approaches are theoretically investigated.

7.2 Outlook

Following the realization of the holmium MOT, future experiments will be Rydberg spectroscopy on the hollow cathode lamp to test out the feasibility of the 413 nm Rydberg transition for quantum collective encoding [12, 8, 71]. And in parallel we will try building a red dipole trap at 821 nm, and the narrow-line cooling at 598.5 nm onto the MOT. The 413 nm light will be frequency doubled from a 826 nm external cavity diode laser using an LBO crystal SHG cavity. And the 598.5 nm light will be frequency doubled from a 1197 nm external diode laser using a PPKTP crystal SHG cavity.

LIST OF REFERENCES

- [1] Solstis narrow linewidth, tunable cw ti:sapphire laser user manual v 10.0. 2012.
- [2] Richard P. Feynman. Simulating physics with computers. *International Journal of Theoretical Physics*, 21, Issue: 6-7:467–488, 1982.
- [3] D. Deutsch. Quantum theory, the church-turing principle and the universal quantum computer. *Proc. R. Soc. Lond. A*, 97:400, 1985.
- [4] D. Deutsch and R. Jozsa. Rapid solution of problems by quantum computation. *Proc. R. Soc. Lond. A*, 439:553, 1992.
- [5] P. W. Shor. Algorithms for quantum computation: discrete logarithms and factoring. *Foundations of Computer Science, 1994 Proceedings.*, 35th Annual Symposium:124 – 134, 1994.
- [6] D. Deutsch and R. Jozsa. Rapid solution of problems by quantum computation. *Proc. R. Soc. Lond. A*, 439:553, 1992.
- [7] D. P. DiVincenzo. Dogma and heresy in quantum computing. *Quantum Inform. Comput.*, 1:1, 2001.
- [8] M. Saffman, T. G. Walker, and K. Mølmer. Quantum information with rydberg atoms. *Rev. Mod. Phys.*, 82:2313, 2010.
- [9] D. Jaksch, J. I. Cirac, P. Zoller, S. L. Rolston, R. Côté, and M. D. Lukin. Fast quantum gates for neutral atoms. *Phys. Rev. Lett.*, 85:22082211, 2001.
- [10] M. D. Lukin, M. Fleischhauer, R. Cote, L. M. Duan, D. Jaksch, J. I. Cirac, and P. Zoller. Dipole blockade and quantum information processing in mesoscopic atomic ensembles. *Phys. Rev. Lett.*, 87:037901, 2001.
- [11] E. Brion, K. Mølmer, and M. Saffman. Quantum computing with collective ensembles of multilevel systems. *Phys. Rev. Lett.*, 99:260501, 2007.
- [12] M. Saffman and K. Mølmer. Scaling the neutral-atom rydberg gate quantum computer by collective encoding in holmium atoms. *Physical Review A*, 78:012336, 2008.

- [13] J. J. McClelland and J. L. Hanssen. Laser cooling without repumping: A magneto-optical trap for erbium atoms. *Phys. Rev. Lett.*, 96:143005, 2006.
- [14] Mingwu Lu, Seo Ho Youn, and Benjamin L. Lev. Trapping ultracold dysprosium: A highly magnetic gas for dipolar physics. *Phys. Rev. Lett.*, 104:063001, 2010.
- [15] D. Sukachev, A. Sokolov, K. Chebakov, A. Akimov, S. Kanorsky, N. Kolachevsky, and V. Sorokin. Magneto-optical trap for thulium atoms. *Phys. Rev. A.*, 82:011405(R), 2010.
- [16] A. J. Berglund, J. L. Hanssen, and J. J. McClelland. Narrow-line magneto-optical cooling and trapping of strongly magnetic atoms. *Phys. Rev. Lett.*, 100:113002, 2008.
- [17] M. Lu, S. H. Youn, and B. L. Lev. Spectroscopy of a narrow-line laser-cooling transition in atomic dysprosium. *Phys. Rev. A.*, 83:012510, 2011.
- [18] K. Aikawa, A. Frisch, M. Mark, S. Baier, A. Rietzler, R. Grimm, and F. Ferlaino. Bose-einstein condensation of erbium. *Phys. Rev. Lett.*, 108:210401, 2012.
- [19] M. Lu, N. Q. Burdick, S. H. Youn, and B. L. Lev. Strongly dipolar bose-einstein condensate of dysprosium. *Phys. Rev. Lett.*, 107:190401, 2011.
- [20] M. Lu, N. Q. Burdick, and B. L. Lev. Quantum degenerate dipolar fermi gas. *Phys. Rev. Lett.*, 108:215301, 2012.
- [21] <http://en.wikipedia.org/wiki/holmium>.
- [22] G. F. Wakefield, A. H. Daane, and F. H. Spedding. Vapor pressure of holmium. *J. Chem. Phys.*, 47, No. 12:4994–4999, 1967.
- [23] Saffman wiki page/Ho (not open to public) MATERIAL SAFETY DATA SHEET.
- [24] Single Filament Effusion Cell SFC-40-10-HL-WK-SH-SC User Manual from CREATEC. 2012.
- [25] <http://www.chem.arizona.edu/salzmanr/480a/480ants/knumolco/knumolco.html>.
- [26] T. Bergeman, G. Erez, and H. J. Metcalf. Magnetostatic trapping fields for neutral atoms. *Phys. Rev. A*, 35:1535, 1987.
- [27] Valentin G. Dmitriev, Gagik G. Gurzadyan, and David N. Nikogosyan. Handbook of nonlinear optical crystals (springer series in optical sciences). 1999.
- [28] G.D.Boyd and D.A.Kleinman. Parametric interaction of focused gaussian light beams. *J.Appl.Phys.*, 39:3597, 1968.
- [29] T.W.Hansch and B.Couillaud. Laser frequency stabilization by polarization spectroscopy of a reflecting reference cavity. *Opt.Commun.*, 35(3):441–444, 1980.

- [30] J.-J. Zondy. Twin-crystal walk-off-compensated type-ii second-harmonic generation: single-pass and cavity-enhanced experiments in ktiopo4. *Opt. Commun.*, 81:427, 1991.
- [31] A. Douillet, J.-J. Zondy, A. Yelisseyev, S. Lobanov, and L. Isaenko. Stability and frequency tuning of thermally loaded continuous-wave *aggas2* optical parametric oscillators. *J. Opt. Soc. Am. B*, 16:1481, 1999.
- [32] R. Le Targat, J.-J. Zondy, and P. Lemonde. 75% -effciency blue generation from an intracavity ppktp frequency doubler. *Optics Communications*, 247:471–481, 2005.
- [33] S.Bourzeix, M.D.Plimmer, F. Nez, L.Julien, and F.Biraben. Efficient frequency doubling of a continuous wave titanium:sapphire laser in an external enhancement cavity. *Optics Communications*, 99:89–94, 1993.
- [34] <http://www.u-oplaz.com/crystals/crystals03.htm>.
- [35] D. N. Nikogosyan. Lithium triborate. *Appl. Phys. A*, 58:181–190, 1994.
- [36] Y. Cha, K. Ko, G. Lim, J. Han, H. Park, T. Kim, and D. Jeong. External-cavity frequency doubling of a 5-w 756-nm injection-locked ti:sapphire laser. *Optics Express*, 16(7):4866–4871, 2008.
- [37] E. Arimondo, M. Ingoscio, and P. Violino. Experimental determinations of the hyperfine structure in the alkali atoms. *Reviews of Modern Physics*, 49, No.1:30–75, 1977.
- [38] C. I. Hancox. Magnetic trapping of transition-metal and rare-earth atoms using buffer-gas loading. *Ph.D Thesis*, 2005.
- [39] W. Dankwort, J. Ferch, and H. Gebauer. Hexadecapole interaction in the atomic ground state of ^{165}ho . *Zeitschrift fur Physik*, 267:229–237, 1974.
- [40] B. Burghardt, S. Buttgenbach, N. Glaeser, R. Harzer, G. Meisel, B. Roski, and F. Traber. Hyperfine structure measurements in metastable states of ^{165}ho . *Z. Phys. A*, 1982.
- [41] G Nachtshiem. *Thesis, unpublished*, 1980.
- [42] K. T. Cheng and W. J. Childs. Ab initio calculation of $4f^n6s^2$ hyperfine structure in neutral rare-earth atoms. *Physical Review A*, 31, No. 5:2775–2784, 1985.
- [43] Kurze Originalmitteilungen. Drehimpulsquantenzahl und hyperfeinstrukturaufspaltung des grundzustandes im ^{165}ho i-spektrum. *Die Naturwissenschaften*, 49:101–102, 1962.
- [44] A. Kramida, Y. Ralchenko, J. Reader, and NIST ASD Team. *NIST Atomic Spectra Database (ver. 5.0)*, 2012.
- [45] H. Noh, S. E. Park, L. Z. Li, J. Park, and C. Cho. Modulation transfer spectroscopy for ^{87}rb atoms: theory and experiment. *Optics Express*, 19, Issue 23:23444–23452, 2011.

- [46] L. Z. Li, S. E. Park, H. Noh, J. Park, and C. Cho. Modulation transfer spectroscopy for a two-level atomic system with a non-cycling transition. *Journal of the Physical Society of Japan*, 80, Issue 7:074301–074301–6, 2011.
- [47] Gillian Nave. Atomic transition rates for neutral holmium (hoi). *J. Opt. Soc. Am. B*, 20, No. 10:2193, 2003.
- [48] C. J. Foot. Atomic physics (oxford university press). 2005.
- [49] S. Stenholm. Semiclassical theory of laser cooling. *Rev. Mod. Phys.*, 58:699, 1986.
- [50] C. S. Adams and E. Riis. Laser cooling and trapping of neutral atoms. *Prog. Quant. Electron.*, 21:1, 1997.
- [51] H. J. Metcalf and P. van der Straten. Laser cooling and trapping. *Springer, San Diego*, 2002.
- [52] S. Chu, J. Bjorkholm, A. Ashkin, and A. Cable. Experimental observation of optically trapped atoms. *Physical Review Letters*, 57:314, 1986.
- [53] Z. Lin et al. Laser cooling and trapping of li. *Jpn. J. Appl. Phys.*, 30:L1324, 1991.
- [54] T. Walker, D. Homann, P. Feng, and R. S. Williamson. A vortex-force atom trap. *Physics Letters A*, 163:309–12, 1992.
- [55] D. Sesko, T. Walker, C. Monroe, A. Gallagher, and C. Wieman. Collisional losses from a light-force atom trap. *Phys. Rev. Lett.*, 63:961–4, 1989.
- [56] K. Sengstock, U. Sterr, G. Hennig, D. Bettermann, J. H. Muller, and W. Ertmer. Optical ramsey interferences on laser cooled and trapped atoms, detected by electron shelving. *Optics Communications*, 103:73–8, 1993.
- [57] T. Kurosu and F. Shimizu. Laser cooling and trapping of calcium and strontium. *Japanese Journal of Applied Physics*, 29:L2127–9, 1990.
- [58] F. Bardou, O. Emile, J.-M. Courty, C. I. Westbrook, and A. Aspect. Magneto-optical trapping of metastable helium: collisions in the presence of resonant light. *Europhysics Letters*, 20:681–6, 1992.
- [59] F. Shimizu, K. Shimizu, and H. Takuma. Laser cooling and trapping of ne metastable atoms. *Phys. Rev. A*, 39:2758–60, 1989.
- [60] H. Katori and F. Shimizu. Laser cooling and trapping of argon and krypton using diode lasers. *Japanese Journal of Applied Physics*, 29:L2124–6, 1990.
- [61] M. Walhout, H. J. L. Megens, A. Witte, and S. L. Rolston. Magneto-optical trapping of metastable xenon: isotope-shift measurements. *Phys. Rev. A*, 48:R879–82, 1993.

- [62] S. Chu, J. Bjorkholm, A. Ashkin, and A. Cable. Magneto-optical trapping of yb atoms and a limit on the branching ratio of the 1p_1 state. *Phys. Rev. A*, 59, No.2:R934–R937, 1999.
- [63] J. Dalibard and C. Cohen-Tannoudji. Laser cooling below the doppler limit by polarization gradients: simple theoretical models. *J. Opt. Soc. Am. B*, 6:2023, 1989.
- [64] P. J. Ungar, D. S. Weiss, E. Riis, and S. Chu. Optical molasses and multilevel atoms: theory. *J. Opt. Soc. Am. B*, 6:2058, 1989.
- [65] M. Walhout, J. Dalibard, S. L. Rolston, and W D. Phillips. $\sigma_+ - \sigma_-$ optical molasses in a longitudinal magnetic field. *J. Opt. Soc. Am. B*, 9, No. 11:1997, 1992.
- [66] Siyuan Zhang. Trapping and rydberg excitation of a single atom qubit in a blue detuned bottle beam. *Ph.D. thesis*, 2012.
- [67] P. D. Lett, W. D. Phillips, S. L. Rolston, C. E. Tanner, R. N. Watts, and C. I. Westbrook. Optical molasses. *J. Opt. Soc. Am. B*, 6:2984, 1989.
- [68] P. D. Lett, Richard N. Watts, Christoph I. Westbrook, and William D. Phillips. Observation of atoms laser cooled below the doppler limit. *Phys. Rev. Lett.*, 61, No. 2:169, 1988.
- [69] Xinye Xu, Thomas H. Loftus, Josh W. Dunn, Chris H. Greene, John L. Hall, Alan Gallagher, and Jun Ye. Single-stage sub-doppler cooling of alkaline earth atoms. *Phys. Rev. Lett.*, 91:193002, 2003.
- [70] Andrew J. Berglund, Siu Au Lee, and Jabez J. McClelland. Sub-doppler laser cooling and magnetic trapping of erbium. *Phys. Rev. A*, 76:053418, 2007.
- [71] E. F. Worden, R. W. Solarz, J. A. Paisner, and J. G. Conway. First ionization potentials of lanthanides by laser spectroscopy. *J. Opt. Soc. Am.*, 68:52–61, 1978.
- [72] R. W. P. Drever, J. L. Hall, F. V. Kowalski, J. Hough, G. M. Ford, A. J. Munley, and H. Ward. Laser phase and frequency stabilization using an optical resonator. *Appl. Phys. B*, 31:97–105, 1983.
- [73] R. W. Fox, C. W. Oates, and L. W. Hollberg. Stabilizing diode lasers to high-finesse cavities. *Experimental methods in the physical science*, 40:1–46.
- [74] G. C. Bjorklund and M. D. Levenson. Frequency modulation (fm) spectroscopy. *Appl. Physics. B*, 32:145–152, 1983.
- [75] E. D. Black. An introduction to pound-drever-hall laser frequency stabilization. *Am. J. Phys.*, 69(1):79, 2001.
- [76] T. W. Hansch and B. Couillaud. Laser frequency stabilization by polarization spectroscopy of a reflecting reference cavity. *Optics Communications*, 35(3):441–444, 1980.

- [77] R. K. Raj, D. Bloch, J.J. Snyder, G. Carny, and M. Ducloy. High-frequency optically heterodyned saturation spectroscopy via resonant degenerate four-wave mixing. *Phys. Rev. Lett.*, 44, No. 19:1251, 1980.
- [78] J. H. Shirley. Modulation transfer processes in optical heterodyne saturation spectroscopy. *Opt. Lett.*, 7:537, 1982.
- [79] D J McCarron, S A King, and S L Cornish. Modulation transfer spectroscopy in atomic rubidium. *Meas. Sci. Technol.*, 19:105601, 2008.

Appendix A: Laser Stabilization

A critical element of any atomic physics experiment is the production of narrow linewidth laser light at the required frequencies. This appendix covers the key laser stabilization techniques used throughout this work.

Typically, an optical frequency reference is established by stabilizing a laser either to an optical transition or a high finesse cavity. In order to stabilize the laser a reference signal is fed-back to the laser to counteract any drift in frequency. Typically the feedback mechanism will require the reference signal, known as the "error signal", to be anti-symmetric with a zero crossing centered on the atomic transition. A key feature to laser stabilization is therefore the way a suitable error signal may be generated. Many techniques exist for producing error signals, each have specific advantages and disadvantages.

Frequency control and stabilization of the lasers in this experiment is a necessary requirement. The natural linewidth of the cooling transition of Ho is 32 MHz. Which is relatively forgivable for our laser linewidth. Yet for higher population in the MOT, we still want the laser to be relatively narrow.

Here we describe the stabilization and locking techniques used with our laser system. In the first section we describe in details the Pound-Drever-Hall (PDH) locking used to lock the 820 nm ECDL. In the second section we will briefly discuss the Hddotansch-Couillaud (HC) locking used to lock our home-made SHG cavities. And then in the third section the modulation transfer locking used to lock the commercial Ti:Sa laser reference cavity will be discussed.

A.1 PDH locking

Pound-Drever-Hall laser frequency stabilization is a useful powerful and broadly used technique for frequency stabilizing a laser [72, 73]. This locking scheme is used to lock our external diode laser, and it is similar to frequency modulation spectroscopy (FM-spectroscopy) except that an atomic vapor cell is replaced by a reference cavity. A detailed theoretical discussions are in [74] and [75].

This laser stabilization system is based on signals reflected from a stable Fabry-Perot reference cavity. High sensitivity for detection of resonance information is achieved by optical hetero-dyne detection with sidebands produced by RF phase modulation. The electro-optic modulator (EOM) produces phase-modulation sidebands which are located spectrally well outside the resonator carrier and the sidebands are basically totally reflected from the cavity input mirror because they are not on resonance in the cavity. The carrier frequency matches the cavity resonance frequency and is built up in power at the laser frequency. The field is phase-modulated at a frequency much higher than the resonance line width of the cavity, which is several MHz. The RF modulation is used to derive an electronic error signal that represents the deviation of the laser frequency from a given cavity reference fringe. Then the electronic feedback is used to control the laser frequency and minimize its deviations relative to the cavity fringe. A basic optics layout is shown in fig. A.1

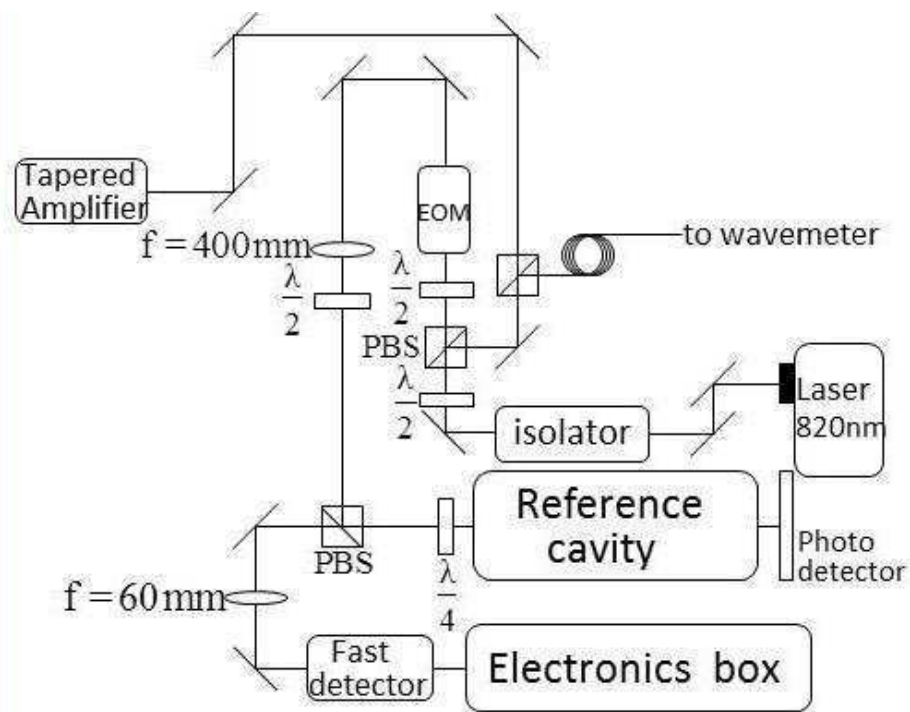


Figure A.1 Optics Layout of the PDH lock

A tank circuit is constructed to amplify the voltage applied to the EOM. It contains an inductor in series with an input resistor of 48 ohms to approximately match the impedance. The modulation

frequency is 41.4MHz which is determined by the tank circuit together with the EOM. The EOM can be seen as a pure capacitive load with a capacitance of 57.5 pF. The inductance in the tank circuit was chosen to make the resonance frequency at 40MHz which corresponds to about 2.3 turns of the coil being used(6.5 mm in diameter, 1.4mm spacing).

The cavity reflection is returned to the fast photodetector using a quater-waveplate along with a PBS. The detector signal is amplified to pass the modulation frequency. Then it is phase-sensitively demodulated using a mixer. The output error signal is filtered and amplified for the feedback loop and sent to the diode lasers piezo.

The fast photo-detector contains two components: a direct reflection term and a leakage term of the resonance signal in the cavity. The detected photocurrent represents the interference of these two components. One sideband is at higher frequency with a phase relative to the carrier that is in phase with the modulation, and the other sideband is at lower frequency that is out of phase by 180 degrees. If there is no phase shift of the laser carrier or modulation sidebands with respect to one another, the detector photocurrent will not have a signal at the modulation frequency because only the phase is modulated not the amplitude and power. The beating between the carrier and the upper frequency sideband produce a photocurrent that is exactly cancelled by the out of phase photocurrent from the lower frequency side. If phase shift occurs in any of them, the photocurrents will not cancel and the RF power at the modulation frequency will appear on the detector signal. Near a cavity resonance, the optical reflection of the carrier from the cavity is phase shifted with respect to the sidebands that are further away from the cavity resonance. Consequently, the detector photocurrent will be non-zero at the modulation frequency. The lasers frequency noise will then appear as noise sidebands centered around the modulation frequency. When this signal is mixed with the RF source signal with the appropriately chosen relative phase(which is achieved by matching the cable length of the path connecting the RF and the mixer), the result is a frequency discriminator with odd symmetry that is used to correct the frequency of the laser. In the absence of residual amplitude modulation or RF pickup, the center of the cavity resonance will correspond to zero at the output error signal. The error signal is then filtered and amplified to control the laser. Oscilloscope captured signals are shown in fig A.2

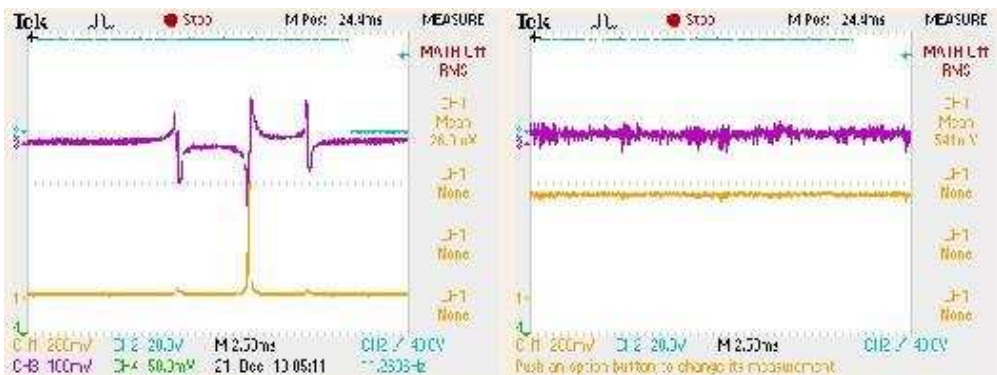


Figure A.2 error signal and cavity transmission signal before and after the laser is locked

The lower curve shows the transmitted intensity of the phase-modulated laser in the reference cavity. The output of the phase-sensitive detector(error signal), upper curve, shows a frequency discriminator dispersion resonance whenever any of the input frequencies match the cavity resonance frequency. These curves were taken with 41MHz modulation frequency.

The goal is to supply enough gain to drive the lasers frequency fluctuations to the noise floor over as much of the feedback bandwidth as possible. At low frequencies, the loop will have very high gain, so that small deviations of the error signal are greatly amplified and the device is forced to move in the proper direction, effectively suppressing the deviation. An RF spectrum analyzer can be used to view the noise sidebands, which are centered at the modulation frequency. The spectrum analyzer display should consist of a center peak at the modulation frequency with noise sidebands on either side. If the gain is increased, the sidebands will increase in amplitude as the feedback starts to oscillate. The trace on the RF spectrum analyser shows the error signal at the mixer input. The noise sidebands are peaking at about 3 MHz when the laser is locked and that indicates the approximate servo bandwidth is nearly this wide. The frequency noise spectrum of the laser changes as the laser sees optical feedback. Checking for locking action is needed by closing the feedback switch on the lock box and turning up the gain knob. An increase in transmission, widening of the resonance, or even a flat top of the fringe are all indications that the polarity of the system is correct and the feedback loop is attempting to keep the laser locked to the fringe. If the overall sign is wrong, the fringe will be suppressed and the system will try to lock to the sidebands

instead. This situation can be corrected by choosing the opposite slope for the discriminator by changing the demodulation phase by 180 degrees which is achieved by the slow inverse switch on the lock box.

Another RF analyser was used at the same position to monitor the noise spectrum of the laser at low frequencies below 100 KHz, shown in fig. A.3

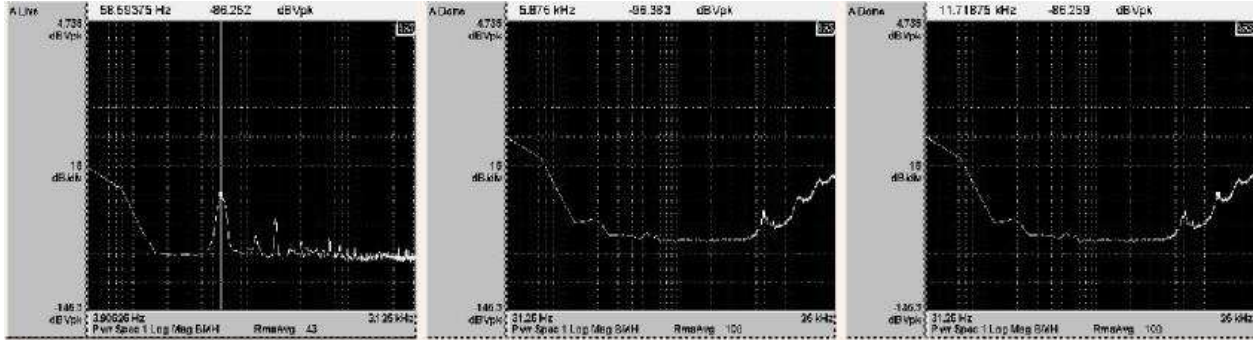


Figure A.3 Noise Spectrum at low frequencies when laser is locked

The output from the mixer is filtered and split into two channels. A slow channel(1KHz bandwidth) discussed above that feeds back to the piezo controlling the length of the lasers external cavity, and a fast channel(3MHz bandwidth) that feeds back to the lasers injection current. The fast modulation connects through the resistor/capacitor combination. It is a passive filter only, which acts as a bias-T to separate the frequency ranges of the slow and fast feedback loops. The current driver is connected to the diode through a 820 uH inductor, acting as a low pass filter to protect the current driver and reduce some high frequency noise of the laser. A basic circuit layout is shown in fig A.4. Dashed line includes all elements in the electronics box in Fig. A.1.

If the electronic feedback bandwidth is wider than the dominant noise spectrum of the laser, the laser fluctuations can be controlled such that the laser appears tightly locked to the peak of the cavity mode. There are two basic determining factors in the final performance of the lock: the initial noise spectrum of the laser and the electronic bandwidth achievable in the servo system. The error signal has odd symmetry about the line center that enables locking to the top of a cavity fringe.

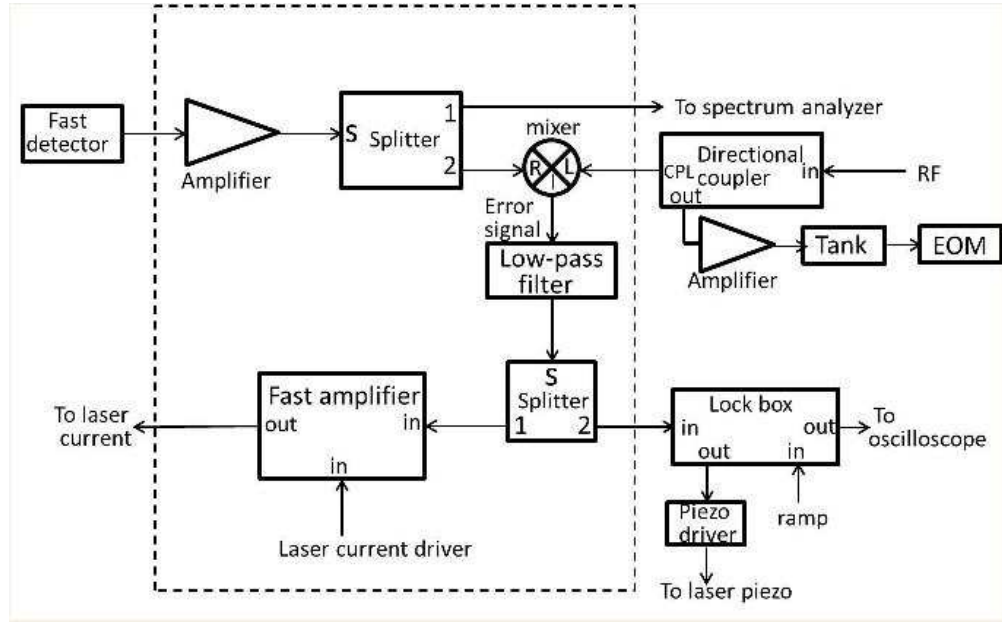


Figure A.4 Circuit Layout

Unwanted amplitude modulation that sometimes occurs is attributable to improper alignment of the beam polarization with respect to the modulator crystals polarization axis. To get rid of it, a half-waveplate is put in front of the EOM. By putting a photo-detector after the first PBS after the EOM and adjusting the wave plate in front of it, a maximum extinction ratio can be achieved and the signal that is monitored on the scope should be a clean thin line instead of a thick noisy signal that represents amplitude modulation to the laser.

A.2 Hänsch-Couillaud (HC) locking

For locking the frequency doubling cavities to the IR pump laser frequency, we used the Hänsch-Couillaud (HC) locking scheme [76]. Fig. fig:HC locking shows its layout of the optics and electronics. The biggest advantage of this locking scheme is that it requires no modulation onto the laser beams.

The laser beam that is reflected from the input coupler mirror of the doubling cavity is split into two beams, with left and right handed circular polarization using a quater-wave plate together with a polarizing beam cube. And the two beams are detected with a balanced photo detector to form

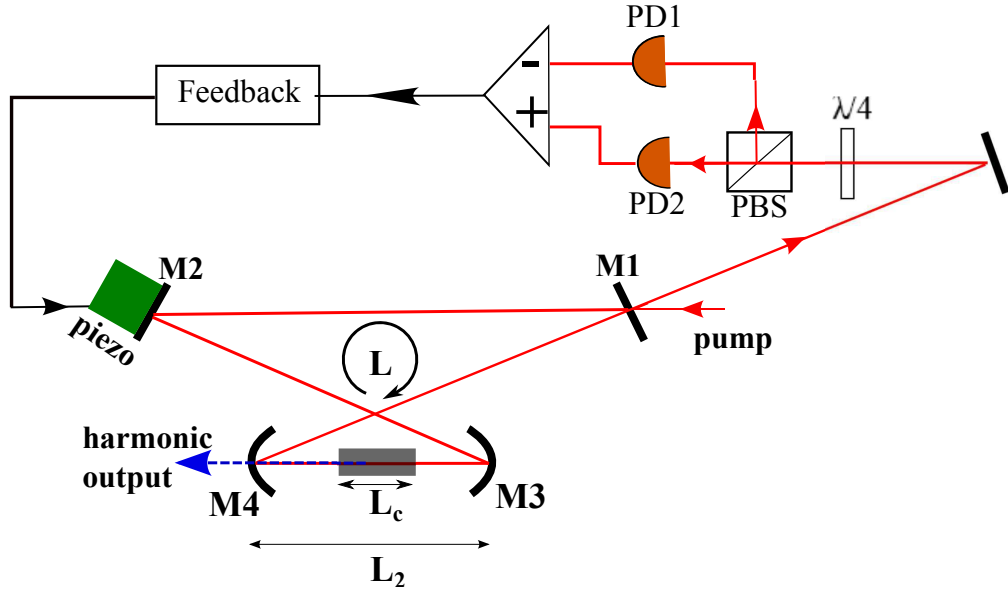


Figure A.5 Circuit Layout

an error signal, then feed back to the piezo inside the doubling cavity. The HC scheme requires a intra-cavity polarizer for polarization selection. Although the doubling cavity does not have any polarization-selective elements, the HC scheme can still be applied due to the birefringence of the nonlinear crystals. The TEM_{00} modes of the cavity for two orthogonal polarizations do not quite overlap, and this is good enough to form an error signal.

A.3 Modulation transfer locking

The Ti:Sa ring cavity consists of four mirrors, an optical diode, a birefringent filter (BRF), and an intracavity thin etalon, all mounted on one baseplate for improved temperature stability. The optical diode forces the ring cavity to operate uni-directionally, resulting in a traveling wave that ensures a minimum of spatial-hole burning. The BRF introduces a wavelength-dependent loss into the cavity, and a wavelength tuning is accomplished by rotating the BRF. This provides a relatively rapid but coarse wavelength adjustment. The etalon introduces a spectral loss into the cavity that is a much sharper function of frequency than the BRF. By electronically adjusting the etalon spacing, the output frequency can be finer tuned. Fig reffig:TiSaRing shows a schematic

layout of the Ti:Sa laser's ring cavity. The laser cavity has been sealed and is not designed for user-adjustable. The user can adjust the tuning

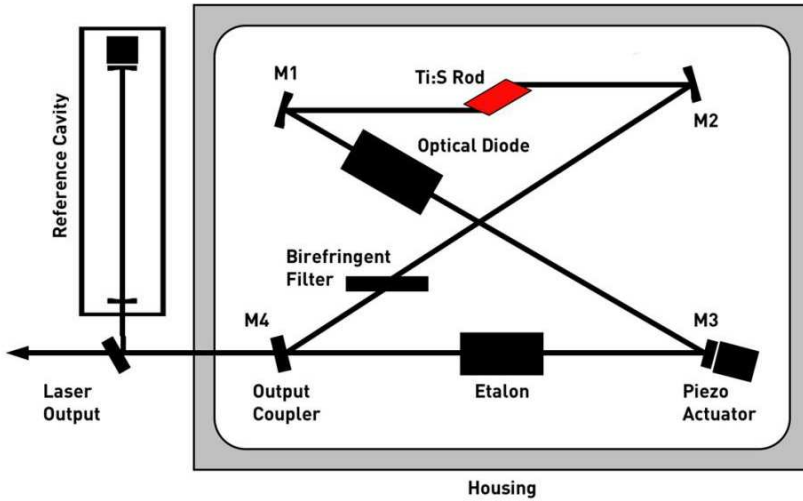


Figure A.6 schematic ring-cavity layout of M Squard Ti:Sa laser [1]

This laser frequency is stabilized by locking to a hollow-cathod Holmium lamp cell. The frequency is shifted with an AOM centered around 80 MHz. And the rf signal frequency was set to about 50 MHz, which is about 1.5γ red-detuned to the cooling transition. A small amount of laser light (about 15 mW) is picked off from the output of the SHG cavity pumped with Ti:Sapph laser output, sent through an acousto-optic modulator (AOM) into the lamp area.

Modulation transfer locking is used to lock the Ti:Sa laser's reference cavity piezo to the signal from the blue light resonance in the hollow cathode holmium lamp. This setup is also one of the setups used for the hyperfine spectroscopy discussed in Chapter 4. Its advantage over FM spectroscopy is that the error signal is on a zero background and it has a large amplitude. And the setup is relatively simple to produce an error signal for the laser to lock to.

A simplified schematic layout of the optics and electronics for laser locking and spectroscopy using this technique is shown in fig A.7. The pump beam is modulated using an EOM. The probe beam and the pump beam which have about equal strength, counter-propagate through the Ho

hollow cathode lamp. The probe beam absorption is detected on a photo detector. The photo-detector signal is mixed with the reference local oscillator signal used to drive the EOM. The mixer gives an IF output of a background-free error signal.

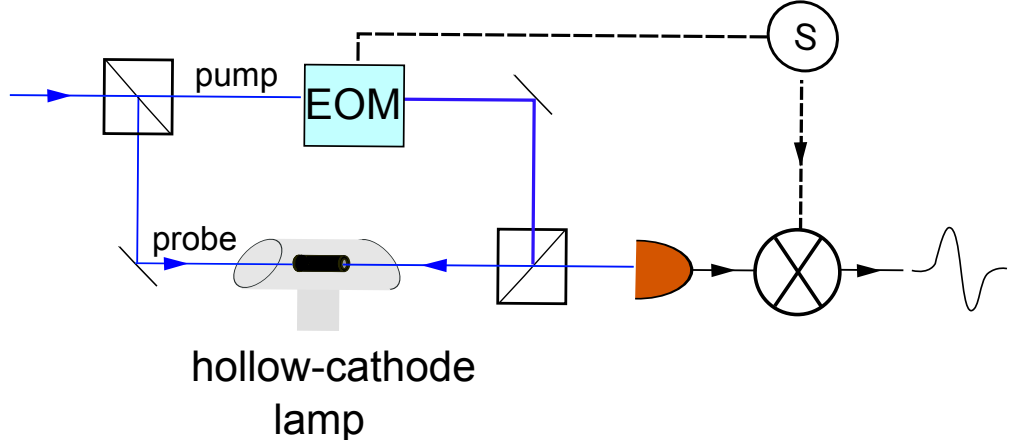


Figure A.7 Modulation transfer spectroscopy setup

This technique produces a strong modulation signal on this transition. The error signal has a flat background. The difference between this modulation transfer technique and the FM spectroscopy technique is that the phase modulation is on the pump beam instead of the probe beam. When the interactions of the pump and probe beams with the atomic medium are sufficiently nonlinear, the modulation is transferred from the pump beam to the probe beam by a four-wave mixing process, which is the most efficient for closed transitions as atoms cannot relax into other ground states. Then the sidebands transferred to the probe beam will beat with the carrier frequency at the photo detector, and absorption and dispersion signals will be produced with the phase sensitive demodulation. This four-wave mixing process which transfers the modulation only occurs when sub-Doppler resonance condition between the probe and pump beams occurs. So the error signal produced is independent of changes in absorption due to fluctuations in polarization, temperature and beam intensity. More detailed theoretical discussions are in [77, 78, 79].